SOLVING THE MHD EQUATIONS IN THE PRESENCE OF NON-AXISYMMETRIC CONDUCTORS USING THE FOURIER-FINITE ELEMENT METHOD

A Dissertation

by

DANIEL CASTANON QUIROZ

Submitted to the Office of Graduate and Professional Studies of
Texas A&M University
in partial fulfillment of the requirements for the degree of

DOCTOR OF PHILOSOPHY

Chair of Committee,	Jean-Luc Guermond
Committee Members,	Wolfgang Bangerth
	Andrea Bonito
	Sharath Girimaji
Head of Department,	Emil Straube

May 2016

Major Subject: Mathematics

ABSTRACT

The research presented in this dissertation focus on the numerical approximation of the magnetohydrodynamic (MHD) equations in the von Kármán Sodium (VKS) set-up. These studies are performed with the `SFEMaNS` MHD code developed by J.-L. Guermond and C. Nore since 2002 for axisymmetric geometries. `SFEMaNS` is based on a spectral decomposition in the azimuthal direction and a Lagrange finite element approximation in a meridian plane. To overcome the axisymmetric restrictions, we propose a novel numerical method to solve the Maxwell part of the MHD equations, and use a pseudo-penalty method to model the rotating impellers. We then present hydrodynamic and MHD simulations of the VKS set-up. Hydrodynamic results compare well with the experimental data in the same range of kinetic Reynolds numbers: at small impeller rotation frequency, the flow is steady; at larger frequency, the fluctuating flow is characterized by small scales and helical vortices localized between the blades. MHD computations are performed for two different flows. One with small kinetic Reynolds number, and the other with a larger one. In both cases, using a ferromagnetic material for the impellers decreases the dynamo threshold and enhances the predominantly axisymmetric magnetic field: the resulting dynamo is a mostly axisymmetric axial dipole with an azimuthal component concentrated in the impellers as observed in the VKS experiment.

ACKNOWLEDGEMENTS

There is an enormous list of individuals, that in one way or another have contributed in getting me to this point. But, I am afraid that if I start writing names I might forget somebody. If that is the case I ask beforehand for their forgiveness. First and foremost, I am very indebted to my parents, my sister and all my family in Mexico. Their support has been invaluable through all these years.

I want to thank my advisor, J.-L. Guermond, for all his patience, encouragement and interesting discussions that we have had through all these years. I also want to thank C. Nore for her encouragement and guidance. The interesting courses, conversations or comments that I have had from all the faculty members of the Numerical Analysis group at Texas A&M have been crucial to my education, especially the ones from R. Lazarov, B. Popov, W. Bangerth, V. Girault, A. Bonito and A. Demlow.

Last in this list of people, but by no means least, I want to thank all my good friends and fellow students. They all have encouraged me to keep going when I needed it and they have made me stop when necessary as well.

TABLE OF CONTENTS

Page

LIST OF FIGURES

FIGURE Page

LIST OF TABLES

TABLE Page

1. INTRODUCTION

1.1 Motivation

Magnetohydrodynamics (MHD) is the physical-mathematical framework that consists of describing the behavior of magnetic fields in electrically conducting fluids, e.g. in plasmas and liquid metals. MHD applications are present in the fields of astrophysics, electrical engineering, petroleum engineering, and plasma physics. The focus on this thesis relies on the so-called dynamo effect, that is the process through which a conducting fluid can maintain a magnetic field. This phenomenon is of special interest in astrophysics, because it affects the formation and behavior of galaxies, stars or planets. Therefore there exist extensive numerical and analytical attempts to understand it.

Unfortunately, the exact mechanism by which a fluid dynamo can be put in action in astrophysical bodies remains an open challenge. It is not until recently that fluid dynamos have been produced in laboratory experiments, thus offering an opportunity to test numerical tools which can then be applied to natural dynamos. The most recent experiment, called the von Kármán Sodium 2 (VKS), was performed in Cadarache, France in 2006, see [42]. Here a dynamo was successfully produced by setting liquid sodium in motion in a closed cylindrical vessel; the liquid metal is kept in motion by two counter-rotating impellers at the top and bottom of the vessel. Each impeller, made of soft iron, is a disk fitted with curved blades. In contrast to previous experimental dynamos, the phenomena involved in VKS experiment is not completely understood until now [27, 26, 38]. This thesis focuses on simulating numerically the VKS experiment in order to assist its comprehension.

There are currently several numerical codes capable to solve MHD problems in

particular geometries, see [31, 59, 61, 65]. My thesis adviser, J.L. Guermond, has been working together with C. Nore in the analysis and MHD simulation since 2002. They have been developing the open source code called `SFEMaNS`[1] for Spectral/Finite elements for Maxwell and Navier-Stokes equations [29, 30, 31]. This code has been validated for non-trivial MHD applications [26, 38], and it is based on a hybrid method with a Fourier decomposition in the azimuthal direction, and Lagrange finite elements in the meridional plane. However, using Lagrange finite elements for electromagnetic problems is quite challenging, because it has been shown by Costabel [13] that standard methods based on those elements can cause convergence problems. Nevertheless, `SFEMaNS` uses a novel Lagrange element formulation which has been proved to be convergent for electromagnetic problems, for mathematical details see Bonito and Guermond [8], and Bonito *et al.* [9].

The code `SFEMaNS` uses Fourier spectral elements in the azimuthal direction in the spirit of [59, 61]. This choice allows to use parallelization techniques for the fast Fourier transform (FFT) producing a massively parallel algorithm for MHD problems. Details of the algorithm and its implementation can be found in the papers of Guermond *et al.* [30, 31]. However, the main restriction of this method is that all parts of the domain must be axisymmetric. Nevertheless, in Guermond *et al.* [31] and Giesecke *et al.* [26], the authors replaced the impellers with flat disks in order to study the influence of the magnetic permeability of the impellers in the VKS experiment.

Extending spectral methods to parts of the domain that are not axisymmetric is a non-trivial problem, but doing so will keep the efficiency and usability of pseudo-spectral codes such as `SFEMaNS`. Moreover, solving numerically a MHD problem involves solving the conducting fluid flow, and the magnetic field generated by

[1]This code can be requested to `guermond@math.tamu.edu`

this flow. In this thesis we use a pseudo-penalty method to model non-axisymmetric moving obstacles, and we propose a novel numerical method to solve the magnetic field generated by a moving non-axisymmetric conductor using Fourier-finite element methods. Both methods allow us to perform full MHD simulations of the VKS experiment. Specifically, MHD computations are performed for two fluid flows, one with small kinetic Reynolds number, and the other with a larger one. In both cases, using a ferromagnetic material for the impellers, enhances the predominantly axisymmetric magnetic field: the resulting dynamo is a mostly axisymmetric axial dipole as observed in the VKS successful experiment.

1.2 Thesis Outline

Section 2 - In this section we introduce the Maxwell, Navier-Stokes, and MHD equations. We also introduce their non-dimensionalization that leads to the use of the kinetic Reynolds number R_{e} and the magnetic Reynolds number R_{m}. We also mention recent laboratory experiments that have successfully generated fluid dynamos, the VKS experiment being the most recent one, and which is the focus of this thesis.

Section 3 - Here we introduce the geometry and PDE setting for the MHD equations. We then introduce a variational weak form, and a Fourier-finite numerical scheme as starting points to produce a new numerical method capable to simulate the VKS experiment. At the end of the section we introduce a simple model for Maxwell equations that illustrates the main difficulty of using spectral Fourier-finite elements.

Section 4 - In this section we propose an efficient numerical time stepping scheme for the simple model proposed at the end of section 3. By efficient time stepping scheme we mean a scheme that generates time independent matrices, and avoids im-

plicit convolutions when hybrid Fourier-finite elements are employed. We extend our ideas for general scalar Partial Parabolic Equations (PDEs) with variable coefficient in space and time.

Section 5 - In this section we extend our ideas of section 4 to the Maxwell equations in the low-frequency regime. We then perform some convergence tests, and report and validate kinematic dynamo computations using the half VKS setting.

Section 6 - Discretization of the Navier-Stokes equations is discussed first, and then we perform hydrodynamic and MHD simulations for the VKS setting at moderated low Reynolds numbers. It is found that for high values of magnetic permeability μ, an axisymmetric magnetic field is predominant. This coincides with the real VKS experiment.

Section 7 - The overall conclusion of this dissertation.

2. THE MHD EQUATIONS AND THE DYNAMO EFFECT

Throughout this thesis the MHD equations are numerically studied. These provide the simplest description of the dynamical coupling between matter (solid and fluid) and the electromagnetic field. In this section we first introduce the MHD equations; we refer to [1, 15, 41] for a detailed discussion. The MHD equations are a coupled system of nonlinear partial differential equations (PDEs), which are composed by the Maxwell and the Navier-Stokes equations. The Maxwell equations govern the electromagnetic field, and the Navier-Stokes equations the fluid motion. The two sets of equations are coupled by the Lorentz force and Ohm's law. After introducing the MHD equations, we then proceed to describe the dynamo effect which is of special interest in the field of astrophysics. We also mention recent laboratory experiments that have successfully generated fluid dynamos, but their complete understanding remains an open question. The VKS2 experiment is the most recent one and is the focus of this thesis. We refer to [17, 57] for a detailed discussion about dynamo theory.

2.1 Maxwell Equations

The classical macroscopic electromagnetic field is described by the Maxwell equations which are as follows:

$$\partial_t \mathbf{B} = -\nabla \times \mathbf{E}, \tag{2.1}$$

$$-\partial_t \mathbf{D} + \nabla \times \mathbf{H} = \mathbf{j}, \tag{2.2}$$

$$\nabla \cdot \mathbf{D} = \rho_c, \tag{2.3}$$

$$\nabla \cdot \mathbf{B} = 0, \tag{2.4}$$

where the fundamental field vectors $\mathbf{E}$ and $\mathbf{H}$ are called the electric and magnetic fields respectively. The vector functions $\mathbf{D}$ and $\mathbf{B}$, which will later be computed by constitutive relations, are called the electric displacement and magnetic induction, respectively. The three-dimensional vector field $\mathbf{j}$ denotes the current density, and the scalar function ρ_c denotes the charge density. Equation (2.1) is called Faraday-Maxwell equation, equation (2.2) is called Ampère-Maxwell equation, the divergence condition (2.3) is called Coulomb-Maxwell equation, and the last equation (2.4) is called Gauss-Maxwell equation. For MHD applications it is common to neglect the term $\partial_t \mathbf{D}$ in equation (2.5) and set $\rho_c = 0$ in (2.4), see [1, 15]. Thus we get

$$\nabla \times \mathbf{H} = \mathbf{j}, \tag{2.5}$$

$$\nabla \cdot \mathbf{D} = 0. \tag{2.6}$$

The Maxwell equations need to be complemented by Ohm's law which in the MHD setting establishes

$$\mathbf{j} = \sigma(\mathbf{E} + \mathbf{u} \times \mathbf{B}) + \mathbf{j}_s \quad \text{in} \quad \Omega_{cf}, \tag{2.7}$$

where σ denotes the electric conductivity of the medium, $\mathbf{u}$ the velocity of the conducting fluid, and $\mathbf{j}_s$ describes the applied current for external sources. Observe that we have explicitly stated that equation (2.7) is only valid in the domain Ω_{cf}, which we will be used to denote the fluid conducting region from now on. In conducting solid, which we denote as Ω_{cs}, Ohm's law simplifies to

$$\mathbf{j} = \sigma \mathbf{E} + \mathbf{j}_s \quad \text{in} \quad \Omega_{cs}. \tag{2.8}$$

In contrast if we are located in the vacuum region (i.e., there is not conducting-

region) we have $\sigma = 0$, and Ohm's law simplifies to

$$\mathbf{j} = 0 \quad \text{in} \quad \Omega_v. \tag{2.9}$$

Specifying the physical nature of the medium where the electromagnetic fields propagate will give us constitutive relations to link $\mathbf{E}, \mathbf{D}, \mathbf{H}$ and $\mathbf{B}$. For instance, when the ambient medium is vacuum such relations are

$$\begin{cases} \mathbf{D} = \epsilon_0 \mathbf{E} & \text{in} \quad \Omega_v, \\ \mathbf{B} = \mu_0 \mathbf{H} & \text{in} \quad \Omega_v, \end{cases}$$

where ϵ_0 and μ_0 denote the electric permittivity and the magnetic permeability of the vacuum, respectively. On the other hand, inside an electrically solid or fluid conducting medium, which we now define as Ω_c such that $\Omega_c = \Omega_{cs} \cup \Omega_v$, we have

$$\begin{cases} \mathbf{D} = \epsilon \mathbf{E} & \text{in} \quad \Omega_c, \\ \mathbf{B} = \mu \mathbf{H} & \text{in} \quad \Omega_c, \end{cases} \tag{2.10}$$

where ϵ and μ, respectively, denote the electric permittivity and the magnetic permeability of the material. In this thesis we will assume that ϵ and μ are positive, bounded and scalar functions of position. It is common practice to measure ϵ and μ using as a reference their values in vacuum defining

$$\begin{cases} \epsilon = \epsilon_r \epsilon_0 \\ \mu = \mu_r \mu_0, \end{cases} \tag{2.11}$$

where ϵ_r and μ_r denote the relative electric permittivity and the relative magnetic permeability to vacuum, respectively. However, for MHD applications related with

this thesis, the Maxwell equations are modeled in the low-frequency regime, so ϵ is not relevant in the conducting region Ω_c, and the condition $\nabla\cdot\mathbf{E} = 0$ only applies for the vacuum region Ω_v where ϵ_0 is constant, see [1, 15]. In summary, using all previous equations the Maxwell system (2.1)-(2.4) becomes

$$\begin{cases} \partial_t(\mu\mathbf{H}) = -\nabla\times\mathbf{E} & \text{in} \quad \Omega, \\ \nabla\times\mathbf{H} = \sigma(\mathbf{E} + \tilde{\mathbf{u}}\times\mathbf{B}) + \mathbf{j}_s, & \text{in} \quad \Omega_c \\ \nabla\times\mathbf{H} = 0 & \text{in} \quad \Omega_v \\ \nabla\cdot\mathbf{E} = 0 & \text{in} \quad \Omega_v, \\ \nabla\cdot(\mu\mathbf{H}) = 0 & \text{in} \quad \Omega, \end{cases} \tag{2.12}$$

where $\Omega = \Omega_c \cup \Omega_v$, and $\tilde{\mathbf{u}}$ is an extension of $\mathbf{u}$ on Ω_c, i.e., $\tilde{\mathbf{u}}$ is equal to $\mathbf{u}$ on Ω_{cf} and is prescribed in Ω_{cs}. It is common to set $\tilde{\mathbf{u}}$ to zero in Ω_{cs}, but it can be also set as a solid rotation velocity.

We are still left to specify the initial and boundary conditions for Maxwell Equations, a standard choice is

$$\begin{cases} \mathbf{E}\times\mathbf{n} = \mathbf{a} & \text{on} \quad \Gamma_n, \\ \mathbf{H}\times\mathbf{n} = \mathbf{H}_d\times\mathbf{n} & \text{on} \quad \Gamma_d, \\ \mathbf{H}|_{t=0} = \mathbf{H}_0 & \text{in} \quad \Omega, \end{cases} \tag{2.13}$$

where $\Gamma_n \cup \Gamma_d = \partial\Omega$. In section 3 we will discuss in more detail the above initial and boundary conditions.

2.2 Navier-Stokes Equations

For MHD applications where a fluid is involved, an incompressible Newtonian fluid will be considered. The time evolution of this fluid is modeled by the incompressible Navier-Stokes equations which are as follows:

$$\begin{cases} \partial_t \mathbf{u} + (\mathbf{u}\cdot\nabla)\mathbf{u} - \nu\Delta\mathbf{u} + \frac{1}{\rho}\nabla p = \frac{1}{\rho}(\nabla\times\mathbf{H})\times(\mu\mathbf{H}) \quad \text{in} \quad \Omega_{cf}, \\ \nabla\cdot\mathbf{u} = 0 \quad \text{in} \quad \Omega_{cf}, \\ \mathbf{u}|_{t=0} = \mathbf{u}_0 \quad \text{in} \quad \Omega_{cf}, \quad \mathbf{u}|_{\Gamma_f} = \mathbf{d}, \end{cases} \tag{2.14}$$

where $\mathbf{u}$ is the fluid velocity, p the fluid pressure, ρ the fluid density, and ν the kinematic viscosity. The term $\nabla\times\mathbf{H}\times(\mu\mathbf{H})$ is called the Lorenz force, and makes possible the interaction between the conducting fluid and the electromagnetic field. The initial velocity is prescribed by $\mathbf{u}_0$, and on the boundary $\Gamma_f = \partial\Omega_{cf}$ the fluid velocity is prescribed by $\mathbf{d}$.

2.3 Non-dimensionalized equations

For numerical analysis and implementation the Navier-Stokes equations and the Maxwell equations have to be expressed in non-dimensionalized form. We denote by $\mathcal{L}$ and $\mathcal{U}$ the reference length and velocity scales, respectively. In all this thesis the density is assumed to be a constant ρ and the reference scale for the pressure is $\mathcal{P} = \rho\mathcal{U}^2$. The reference time scale is $\mathcal{T} = \mathcal{L}/\mathcal{U}$. We take μ_0 as reference magnetic permeability, ϵ_0 as reference electric permittivity, and σ_0 as reference electric conductivity. The reference scale for the magnetic field is $\mathcal{H} = \mathcal{U}\sqrt{\rho/\mu_0}$, and for the electric field we choose $\mathcal{E} = \mu_0\mathcal{H}\mathcal{U}$. The current source $\mathbf{j}_s$ and the data $\mathbf{u}_0, \mathbf{d}, \mathbf{H}_0$ are non-dimensionalized by $\mathcal{H}\mathcal{L}^{-1}$,$\mathcal{U}$,$\mathcal{U}$, and $\mathcal{H}$, respectively. This process leaves two non-dimensional parameters which are referred to as the dynamic Reynolds number,

$R_{\rm e}$, and the magnetic Reynolds number, $R_{\rm m}$, and which are defined as follows:

$$R_{\rm e} = \frac{\mathcal{U}\mathcal{L}}{\nu}, \qquad R_{\rm m} = \mathcal{U}\mathcal{L}\sigma_0\mu_0. \tag{2.15}$$

Henceforth we abuse the notation by using the same symbols for the non-dimensional and the corresponding dimensional quantities. The non-dimensional set of equations are:

$$\begin{cases} \partial_t \mathbf{u} + (\mathbf{u}\cdot\nabla)\mathbf{u} - \frac{1}{R_{\rm e}}\Delta\mathbf{u} + \nabla p = (\nabla\times\mathbf{H})\times(\mu\mathbf{H}), \\ \nabla\cdot\mathbf{u} = 0, \\ \mathbf{u}|_{t=0} = \mathbf{u}_0 \quad \text{in} \quad \Omega_{cf}, \quad \mathbf{u}|_{\Gamma_f} = \mathbf{d}. \end{cases} \tag{2.16}$$

$$\begin{cases} \partial_t(\mu\mathbf{H}) = -\nabla\times\mathbf{E} & \text{in} \quad \Omega, \\ \nabla\times\mathbf{H} = R_{\rm m}\sigma(\mathbf{E} + \tilde{\mathbf{u}}\times\mathbf{B}) + \mathbf{j}_s, & \text{in} \quad \Omega_c \\ \nabla\times\mathbf{H} = 0 & \text{in} \quad \Omega_v \\ \nabla\cdot\mathbf{E} = 0 & \text{in} \quad \Omega_v, \\ \nabla\cdot(\mu\mathbf{H}) = 0 & \text{in} \quad \Omega, \\ \mathbf{H}|_{t=0} = \mathbf{H}_0 & \text{in} \quad \Omega, \\ \mathbf{E}\times\mathbf{n} = \mathbf{a} & \text{on} \quad \Gamma_n, \\ \mathbf{H}\times\mathbf{n} = \mathbf{H}_d\times\mathbf{n} & \text{on} \quad \Gamma_d. \end{cases} \tag{2.17}$$

2.4 The Dynamo Effect

The fluid dynamo effect is the process through which a conducting fluid can maintain a magnetic field. This phenomenon is of special interest in astrophysics, because it affects the formation and behavior of galaxies, stars or planets. Moreover, the dynamo effect is considered responsible for the ubiquity of the magnetic field in the Universe. Therefore there exist extensive numerical and analytical attempts to understand this effect. Unfortunately, the exact mechanism by which a fluid dynamo can be put in action in astrophysical bodies remains an open challenge.

It is not until recently that fluid dynamos have been produced in laboratory experiments; the three known ones are in Karlsruhe, Riga and Cadarache. The first two were produced in homogeneous conditions, i.e., μ is constant; moreover, these dynamos are well understood by theoretical models, which establishes the presence of non-axisymmetric magnetic field when the fluid velocity is axisymmetric. In contrast, the experiment in Cadarache was performed using heterogeneous and high permeability conductors. This setting produced a dynamo which magnetic field is mainly axisymmetric. Such dynamo has not yet been fully understood. We now proceed to describe in more detail all these experimental dynamos.

2.4.1 The Karlsruhe Dynamo

The Karlsruhe Dynamo experiment in 2000 in Germany (see [62]) demonstrated the model proposed by Roberts in 1970 (*cf.* [54, 55]). In this model a periodic fluid flow is prescribed as

$$\mathbf{u} = \sin(y)\mathbf{e}_x + \sin(x)\mathbf{e}_y + (\cos(x) - \cos(y))\mathbf{e}_z.$$

Roberts showed that this fluid is capable of dynamo action. The Karlsruhe Dy-

namo experiment consisted in an array of columnar tubes with pumps filled with liquid sodium, and confined in a cylindrical container. Such pumps created helical vortices's which generated two quasi-dipolar magnetic fields of opposite direction.

2.4.2 The Riga Dynamo

This experiment was done at Riga, Latvia in 2000 (see [22, 23]) which proved the Ponomarenko model [48]. This states that a cylinder with constant angular and axial velocities can maintain a magnetic field in an homogeneous medium. The experimental set up consists of three concentric cylinders all filled with liquid sodium. An helical flow is produced by a propeller situated at the top in the innermost cylinder, and then the flow is redirected by a coaxial back-region in the middle cylinder. The flow in the outermost cylinder is at rest at the beginning of the experiment, but Lorentz forces are expected to produce flow movement too. In this set up, the generated magnetic field was an helical non-axisymmetric field rotating in the same sense as the helical velocity field.

2.4.3 The Von Kármán Sodium Experiment 2

The von Kármán Sodium 2 (VKS2) experiment in Cadarache (France) has successfully achieved a self generated magnetic field in a conducting liquid in 2006, see [42]. The experiment mainly consists of a cylindrical container filled of liquid sodium heated at 140 degrees Celsius, which is stirred by two counter-rotating impellers located at the top and bottom of the container. Each impeller is composed of a supporting disk and eight curved blades. These act on the liquid sodium as efficient centrifugal pumps, and also act as magnetic conductors in the experiment. Figure 2.1 shows the experimental setting. This counter-rotating configuration can drive a turbulent flow up to Reynolds numbers as high as $10^7 \sim 10^8$. Initially the blades used in the VKS2 experiment were made of stainless steel, but dynamo action

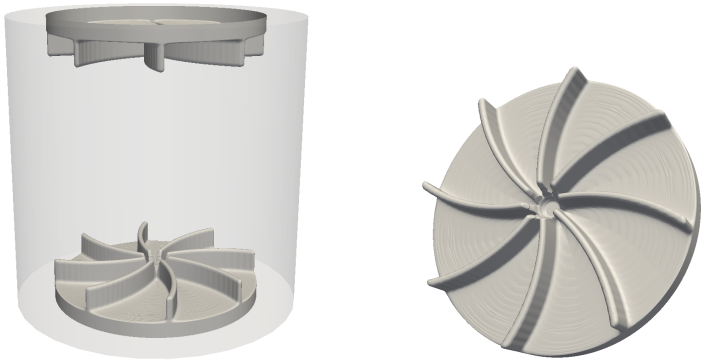

(a) Geometry. (b) Impeller.

Figure 2.1: VKS experimental setting.

was only achieved when the impellers were replaced by ferromagnetic ones; specifically, blades made of soft iron material. Moreover, once dynamo action occured the measured time-averaged magnetic field was steady and axisymmetric. Thus, it can be concluded that the presence of dynamo action with ferromagnetic impellers and the axisymmetry of the magnetic field were interlinked, but until now there was no satisfying explanation about the generation of the mainly axisymmetric magnetic field observed in this experiment [27, 26, 38]. This thesis is devoted to understand the mechanism in action in the VKS2 experiment using numerical simulation.

3. PRELIMINARIES OF MHD FINITE ELEMENT APPROXIMATION

In this section we introduce the geometry and PDE setting for the MHD Equations (2.16) and (2.17). We then introduce a variational weak form, and a numerical scheme as starting points to produce a new numerical method capable to simulate the VKS experiment. Such starting scheme has been implemented in the code `SFEMaNS` (for Spectral/Finite Elements for Maxwell and Navier-Stokes equations) developed mainly by J.L. Guermond and C. Nore, see [29, 30, 26, 31, 38]. However, the original scheme and therefore `SFEMaNS`, can handle only axisymmetric piecewise constant magnetic permeability μ. Overcoming the axisymmetric restricion is not trivial as explained in subsection 3.7.

3.1 The Geometry Setting

The MHD equations are considered in a bounded axisymmetric domain $\Omega \subset \mathbb{R}^3$. The boundary of Ω is denoted by $\Gamma = \partial\Omega$ and is assumed to be at least Lipchitz continuous. Ω is assumed to be partitioned into a conducting region (subscript c) and an insulating region (subscript v) as follows:

$$\overline{\Omega} = \overline{\Omega_c} \cup \overline{\Omega_v}, \quad \Omega_c \cap \Omega_v = \emptyset.$$

Ω_c is referred to as the conducting domain and Ω_v is referred to as the non-conducting domain. The conducting domain is further assumed to be partitioned into a fluid region Ω_{cf}, and a solid region Ω_{cs} such that

$$\overline{\Omega_c} = \overline{\Omega_{cs}} \cup \overline{\Omega_{cf}}, \quad \Omega_{cs} \cap \Omega_{cf} = \emptyset.$$

The interface between the conducting region and the non-conducting region is denoted by,

$$\Sigma = \partial\Omega_c \cap \Omega_v.$$

For the time being, the magnetic permeability μ is assumed to be dependent only in r and z, i.e, $\mu = \mu(r, z)$, and piecewise smooth over Ω_c. This last assumption will be dropped in sections 5 and 6. Being more precise, we assume that the conducting region Ω_c, can be partitioned into sub-regions $\Omega_{c1}, \ldots, \Omega_{cN}$ so that the restriction of μ over each sub-region $\Omega_{ci}, i \in \overline{1, N}$, is smooth. In other words,

$$\overline{\Omega_c} = \overline{\Omega_{c1}} \cup \cdots \cup \overline{\Omega_v}, \quad \Omega_{ci} \cap \Omega_{cj} = \emptyset, \quad \forall i, j \in \overline{1, N}.$$

The interface between all the conducting sub-regions is also given and denoted by Σ_μ,

$$\Sigma_\mu = \cup_{i,j \in \overline{1,N}} \overline{\Omega_{ci}} \cap \overline{\Omega_{cj}}.$$

The interfaces Σ and Σ_μ are fixed and given; they correspond to changes of material properties and one side of these interfaces is always a non-deformable solid. To easily refer to boundary conditions, we introduce

$$\Gamma_c = \Gamma \cap \partial\Omega_c, \quad \text{and} \quad \Gamma_v = \Gamma \cap \partial\Omega_v,$$

so we have $\Gamma = \Gamma_v \cup \Gamma_c$. We assume that $\partial\Omega_v$ has $J + 1$ connected components, for instance, $\Gamma_v^0, \ldots, \Gamma_v^J$, where is assumed that Γ_v^0 is the conneceted component of $\partial\Omega_v$ that contains Γ_v. We also partitionate Γ_c to impose different boundary conditions, so we set $\Gamma_c = \Gamma_{c,d} \cup \Gamma_{c,n}$ where $\Gamma_{c,d} \cap \Gamma_{c,n} = \emptyset$.

It is useful to define the average for any scalar or vector function f that is two-

valued at $\mathbf{x} \in \overline{\Omega_{ci}} \cap \overline{\Omega_{cj}}$ as,

$$\{f\}(\mathbf{x}) = \frac{1}{2}(f_1(\mathbf{x}) + f_2(\mathbf{x})).$$

We denote by $\mathbf{n}^c$ and $\mathbf{n}^v$ the outward normal on $\partial\Omega_c$ and $\partial\Omega_v$, respectively. Similarly, to distinguish between the limits $\lim_{\Omega_{ci}\ni\mathbf{y}\to\mathbf{x}}$ and $\lim_{\Omega_{cj}\ni\mathbf{y}\to\mathbf{x}}$ whenever $\mathbf{x}$ is on the interface Σ_μ and $\mathbf{x} \in \overline{\Omega_{ci}} \cap \overline{\Omega_{cj}}$, we set

$$\mathbf{H}_1(\mathbf{x}) = \begin{cases} \lim_{\Omega_{ci}\ni\mathbf{y}\to\mathbf{x}} \mathbf{H}(\mathbf{y}) & \text{if} \quad i < j \\ \lim_{\Omega_{cj}\ni\mathbf{y}\to\mathbf{x}} \mathbf{H}(\mathbf{y}) & \text{otherwise,} \end{cases} \tag{3.1}$$

$$\mathbf{H}_2(\mathbf{x}) = \begin{cases} \lim_{\Omega_{cj}\ni\mathbf{y}\to\mathbf{x}} \mathbf{H}(\mathbf{y}) & \text{if} \quad i < j \\ \lim_{\Omega_{ci}\ni\mathbf{y}\to\mathbf{x}} \mathbf{H}(\mathbf{y}) & \text{otherwise.} \end{cases} \tag{3.2}$$

We define $\mu_1(\mathbf{x})$ and $\mu_2(\mathbf{x})$ similarly. We also denote by $\mathbf{n}^i(\mathbf{x})$ and $\mathbf{n}^j(\mathbf{x})$ the outward normal at $\mathbf{x}$ on $\partial\Omega_{ci}$ and $\partial\Omega_{cj}$, respectively. Assuming that $i < j$, we set $\mathbf{n}_1(\mathbf{x}) = \mathbf{n}^i(\mathbf{x})$ and $\mathbf{n}_2(\mathbf{x}) = \mathbf{n}^j(\mathbf{x})$.

3.2 PDE Setting of MHD Equations

We now write again the MHD equations (2.16) and (2.17) introduced in section 2 using the notation defined in the preceding subsection; namely, the Navier-Stokes equations are

$$\begin{cases} \partial_t \mathbf{u} + (\mathbf{u}\cdot\nabla)\mathbf{u} - \frac{1}{R_e}\Delta\mathbf{u} + \nabla p = (\nabla\times\mathbf{H})\times(\mu\mathbf{H}) \quad \text{in} \quad \Omega_{cf}, \\ \nabla\cdot\mathbf{u} = 0 \quad \text{in} \quad \Omega_{cf}, \\ \mathbf{u}|_{t=0} = \mathbf{u}_0 \quad \text{in} \quad \Omega_{cf}, \quad \mathbf{u}|_{\Gamma_f} = \mathbf{d}, \end{cases} \tag{3.3}$$

and the Maxwell equations are

$$
\begin{cases}
\partial_t(\mu\mathbf{H}) = -\nabla\times\mathbf{E} & \text{in} \quad \Omega, \\
\nabla\times\mathbf{H} = R_{\mathrm{m}}\sigma(\mathbf{E}+\tilde{\mathbf{u}}\times(\mu\mathbf{H})) + \mathbf{j}_s, & \text{in} \quad \Omega_{ci}, \quad i \in \overline{1,N}, \\
\nabla\times\mathbf{H} = 0 & \text{in} \quad \Omega_v \\
\nabla\cdot\mathbf{E} = 0 & \text{in} \quad \Omega_v, \\
\nabla\cdot(\mu\mathbf{H}) = 0 & \text{in} \quad \Omega, \\
\mu_1\mathbf{H}_1\cdot\mathbf{n}_1 + \mu_2\mathbf{H}_2\cdot\mathbf{n}_2 = 0 & \text{on} \quad \Sigma_\mu, \\
\mathbf{H}_1\times\mathbf{n}_1 + \mathbf{H}_2\times\mathbf{n}_2 = 0 & \text{on} \quad \Sigma_\mu, \\
\mathbf{E}_1\times\mathbf{n}_1 + \mathbf{E}_2\times\mathbf{n}_2 = 0 & \text{on} \quad \Sigma_\mu, \\
\mathbf{H}|_{t=0} = \mathbf{H}_0 & \text{in} \quad \Omega, \\
\int_{\Gamma_v^i}\mathbf{E}\cdot\mathbf{n} = 0, \quad 1 \le i \le J, & \\
\mathbf{E}\times\mathbf{n} = \mathbf{a} & \text{on} \quad \Gamma_v \cup \Gamma_{c,n}, \\
\mathbf{H}\times\mathbf{n} = \mathbf{H}_d\times\mathbf{n} & \text{on} \quad \Gamma_{c,d}.
\end{cases}
\tag{3.4}
$$

Observe that conditions $(\mathbf{H}_1^c\times\mathbf{n}_1^c + \mathbf{H}_2^c\times\mathbf{n}_2^c)|_{\Sigma_\mu} = 0$, and $(\mathbf{E}_1^c\times\mathbf{n}_1^c + \mathbf{E}_2^c\times\mathbf{n}_2^c)|_{\Sigma_\mu} = 0$, were added to ensure continuity along the tangential component for $\mathbf{H}$ and $\mathbf{E}$, respectively. Similarly, the condition $(\mu_1\mathbf{H}_1^c\cdot\mathbf{n}_1^c + \mu_2\mathbf{H}_2^c\cdot\mathbf{n}_2^c)|_{\Sigma_\mu} = 0$ ensures continuity along the normal component of $\mu\mathbf{H}$. Moreover, the conditions $\int_{\Gamma_v^i}\mathbf{E}\cdot\mathbf{n} = 0$ were added to equations (2.17), because those are a consequence of using heterogeneous conductors in the low-frequency regime, see [1] for details.

The initial data are assumed to satisty the compatibility conditions $\nabla\cdot(\mu\mathbf{H}_0) = 0, \nabla\cdot\mathbf{u}_0 = 0$, and $\mathbf{u}|_{\Gamma_f} = \mathbf{d}|_{t=0}$. Then observe that the condition $\nabla\cdot(\mu\mathbf{H}) = 0$ is a consequence of using $\nabla\cdot(\mu\mathbf{H}_0) = 0$, and the first equation of (3.4), so we drop it for

the time being, but it will appear again when a discretization scheme is introduced.

It is possible to eliminate the electric field $\mathbf{E}$ from (3.4). We start by assuming that Ω_v is simply connected, so condition $\nabla\times\mathbf{H}|_{\Omega_v} = 0$ implies there exists a scalar potential ϕ, defined up to an arbitrary constant, such that $\mathbf{H}|_{\Omega_v} = \nabla\phi$, see [43, Theorem 3.37] for a formal proof of this statement. Also if we assume $\mathbf{H}_0$ satisfies $\nabla\times\mathbf{H}_0|_{\Omega_v} = 0$, we can also define ϕ_0 such that $\mathbf{H}_0|_{\Omega_v} = \nabla\phi_0$. Moreover, since the distinction between Ω_c and Ω_v has been made, we define

$$\mathbf{H} = \begin{cases} \mathbf{H}^c & \text{in} \quad \Omega_c \\ \\ \nabla\phi & \text{in} \quad \Omega_v \end{cases}, \mathbf{E} = \begin{cases} \mathbf{E}^c & \text{in} \quad \Omega_c \\ \\ \mathbf{E}^v & \text{in} \quad \Omega_v \end{cases}, \text{and} \quad \mu = \begin{cases} \mu^c & \text{in} \quad \Omega_c \\ \\ \mu_v & \text{in} \quad \Omega_v \end{cases}. \tag{3.5}$$

By inserting the above definitions and the scalar potential ϕ into (3.4) we get,

$$\begin{cases} \partial_t(\mu^c\mathbf{H}^c) = -\nabla\times\mathbf{E}^c, & \text{in} \quad \Omega_{ci}, \quad i \in \overline{1,N}, \\ \nabla\times\mathbf{H}^c = R_{\mathrm{m}}\sigma(\mathbf{E}^c + \tilde{\mathbf{u}}\times(\mu^c\mathbf{H}^c)) + \mathbf{j}_s, & \text{in} \quad \Omega_{ci}, \quad i \in \overline{1,N}, \\ \mu^v\partial_t\phi = -\nabla\times\mathbf{E}^v, & \text{in} \quad \Omega_v, \\ \nabla\cdot\mathbf{E}^v = 0, & \text{in} \quad \Omega_v, \\ \mu_1\mathbf{H}_1^c\cdot\mathbf{n}_1^c + \mu_2\mathbf{H}_2^c\cdot\mathbf{n}_2^c = 0 & \text{on} \quad \Sigma_\mu, \\ \mathbf{H}_1^c\times\mathbf{n}_1^c + \mathbf{H}_2^c\times\mathbf{n}_2^c = 0 & \text{on} \quad \Sigma_\mu, \\ \mathbf{E}_1^c\times\mathbf{n}_1^c + \mathbf{E}_2^c\times\mathbf{n}_2^c = 0 & \text{on} \quad \Sigma_\mu, \\ \mathbf{E}^c\times\mathbf{n}|_{\Gamma_{c,n}} = \mathbf{a}|_{\Gamma_c} \quad \mathbf{E}^v\times\mathbf{n}|_{\Gamma_v} = \mathbf{a}|_{\Gamma_v}, \\ \mathbf{H}^c\times\mathbf{n}|_{\Gamma_{c,d}} = \mathbf{H}_d^c\times\mathbf{n}|_{\Gamma_{c,d}}, \\ \int_{\Gamma_v^i}\mathbf{E}\cdot\mathbf{n} = 0, \quad 1 \le i \le J, \\ \mathbf{H}^c|_{t=0} = \mathbf{H}_0^c \quad \phi|_{t=0} = \phi_0. \end{cases} \tag{3.6}$$

To eliminate the arbitrariness of ϕ, the zero mean condition $\int_{\Omega_v}\phi=0$ is enforced. We now solve $\mathbf{E}^c$ in the second equation of (3.6) and inject this result to the first equation. Taking the divergence in both sides of the third equation, we get rid of $\nabla\times\mathbf{E}^v$. Using $\mathbf{E}^v|_{\Gamma_v}=(\mathbf{E}^v\cdot\mathbf{n}^v)\mathbf{n}^v+\mathbf{n}^v\times\mathbf{a}$, we eliminate the tangential component $\mathbf{E}^v$ on Γ_v, and we finally obtain the following MHD equations system:

$$\begin{cases}\partial_t\mathbf{u}+(\mathbf{u}\cdot\nabla)\mathbf{u}-R_{\mathrm{e}}^{-1}\Delta\mathbf{u}+\nabla p=(\nabla\times\mathbf{H})\times(\mu\mathbf{H}) \quad \text{in} \quad \Omega_{cf},\\ \nabla\cdot\mathbf{u}=0 \quad \text{in} \quad \Omega_{cf},\\ \mathbf{u}|_{t=0}=\mathbf{u}_0 \quad \text{in} \quad \Omega_{cf}, \quad \mathbf{u}|_{\Gamma_f}=\mathbf{d},\end{cases} \tag{3.7}$$

$$\begin{cases}\partial_t(\mu^c\mathbf{H}^c)=-\nabla\times(R_{\mathrm{m}}^{-1}\sigma^{-1}(\nabla\times\mathbf{H}^c-\mathbf{j}^s)-\tilde{\mathbf{u}}\times(\mu^c\mathbf{H}^c)) & \text{in} \quad \Omega_{ci}, \quad i\in\overline{1,N},\\ \mu^v\partial_t\Delta\phi=0, & \text{in} \quad \Omega_v,\\ (R_{\mathrm{m}}^{-1}\sigma^{-1}(\nabla\times\mathbf{H}^c-\mathbf{j}^s)-\tilde{\mathbf{u}}\times(\mu^c\mathbf{H}^c))\times\mathbf{n}^c=\mathbf{a} & \text{on} \quad \Gamma_{c,n},\\ \mathbf{H}^c\times\mathbf{n}=\mathbf{H}_d^c\times\mathbf{n} & \text{on} \quad \Gamma_{c,d},\\ \mu^v\partial_{\mathbf{n}^v}\partial_t\phi=-\mathbf{n}^v\cdot\nabla\times(\mathbf{n}^v\times\mathbf{a}), & \text{on} \quad \Gamma_v,\\ \mathbf{H}_1^c\times\mathbf{n}_1^c+\mathbf{H}_2^c\times\mathbf{n}_2^c=0 & \text{on} \quad \Sigma_\mu,\\ \mu_1\mathbf{H}_1^c\cdot\mathbf{n}_1^c+\mu_2\mathbf{H}_2^c\cdot\mathbf{n}_2^c=0 & \text{on} \quad \Sigma_\mu,\\ \mathbf{H}^c\times\mathbf{n}^c+\nabla\phi\times\mathbf{n}^v=0 & \text{on} \quad \Sigma,\\ \mu^c\mathbf{H}^c\cdot\mathbf{n}^c+\mu^v\nabla\phi\cdot\mathbf{n}^v=0 & \text{on} \quad \Sigma,\\ \mathbf{H}|_{t=0}=\mathbf{H}_0, \quad \phi|_{t=0}=\phi_0 & \text{in} \quad \Omega.\end{cases} \tag{3.8}$$

3.3 Function Spaces

In this subsection a variational weak form is presented as one of the building blocks to accomplish a complete VKS-MHD simulation. We begin defining some standard functions spaces, see [19, 28, 43] for a complete treatise in this subject. For all this subsection we assume $\Omega \subset \mathbb{R}^3$ is a Lipchitz open bounded set, not necessarily axisymmetric. Let us denote as $L^p(\Omega)$ the space of Lebesgue integrable scalar functions with exponent $1 \leq p \leq \infty$ defined on Ω and normed, for $1 \leq p < \infty$, by

$$\|v\|_{L^p(\Omega)} = \left(\int_\Omega |v|^p \right)^{\frac{1}{p}},$$

and, for $p = \infty$,

$$\|v\|_{L^\infty(\Omega)} = \text{esssup}_{x \in \Omega} |v|,$$

for which these spaces are Banach spaces. The most important case here is $p = 2$, which is the set of all square-integrable functions and is a Hilbert space where we denote as $(\cdot, \cdot)$ its scalar product.

Let s and p be two integers with $s \geq 0$ and $1 \leq p \leq \infty$. We denote by $W_p^s(\Omega)$ the Sobolev space of functions $L^p(\Omega)$ with partial derivatives (in the distribution sense) of order up to s in $L^p(\Omega)$, that is

$$W_p^s(\Omega) = \{v \in L^p(\Omega) : \partial^m v \in L^p(\Omega), \forall \quad |m| \leq s\},$$

equipped with the norm (for which it is a Banach space)

$$\|v\|_{W_p^s(\Omega)} = \sum_{|m|=s} \|\partial^m v\|_{L^p(\Omega)}.$$

A particularly important case occurs when $p = 2$, and it is denoted as $H^s(\Omega)$

which is a Hilbert space. By $H_0^1(\Omega)$ or $H_0(\Omega)$ we denote the closure of $\mathcal{C}_0^\infty(\Omega)$ in the H^1-norm, where $\mathcal{C}_0^\infty$ is the space of infinitely differentiable functions having compact support in Ω. We also denote H^{-1} as the dual space of $H_0(\Omega)$. It is well known that for functions in $H^1(\Omega)$, the trace is well defined at the boundary; namely, let $\gamma_0 : \mathcal{C}^0(\overline{\Omega}) \to \mathcal{C}^0(\partial\Omega)$ map functions in $\mathcal{C}^0(\overline{\Omega})$ to their trace $\partial\Omega$, then γ_0 can be continuously extended to $W_p^1(\Omega)$, see [19, Theorem B.52]. Moreover, if $v \in H_0(\Omega)$, then $\gamma_0(v) = 0$ almost everywhere at the boundary.

We now proceed to define spaces of vector functions, we denote as $\mathbf{L}^2(\Omega)$ the space of functions such that each component v_i is in $L^2(\Omega)$ equipped with the norm

$$\|\boldsymbol{v}\|_{L^p(\Omega)} = \sum_{i=1}^{3} \|v_i\|_{L^p(\Omega)}.$$

Similarly, we define $\mathbf{H}^s(\Omega)$ and $\mathbf{H}_0^s(\Omega)$. We denote as $\mathbf{H}_{\text{curl}}(\Omega)$ the space of vector functions $\mathbf{v}$ in $\mathbf{L}^2(\Omega)$ such that $\nabla\times\mathbf{v}$ is in $\mathbf{L}^2(\Omega)$. The space is $\mathbf{H}_{\text{curl}}(\Omega)$ equipped by the canonical norm (for which it is a Banach space)

$$\|\mathbf{v}\|_{\mathbf{H}_{\text{curl}}(\Omega)} = \left(\|\mathbf{v}\|^2_{\mathbf{L}^2(\Omega)} + \|\nabla\times\mathbf{v}\|^2_{\mathbf{L}^2(\Omega)}\right)^{\frac{1}{2}}.$$

For $\mathbf{v} \in \mathbf{H}_{\text{curl}}(\Omega)$ and $\mathbf{u} \in \mathbf{H}^1(\Omega)$, we have the following integration by parts formula

$$\int_\Omega (\nabla\times\mathbf{v})\cdot\mathbf{u} = \int_\Omega (\nabla\times\mathbf{u})\cdot\mathbf{v} - \int_{\partial\Omega} (\mathbf{v}\times\mathbf{n})\cdot\mathbf{u} \tag{3.9}$$

where $\mathbf{v}\times\mathbf{n}$ is the tangential trace operator, please refer to [43, Theorem 3.29] for details. Moreover, we denote as $\mathbf{H}_{\text{div}}(\Omega)$ the space of vector functions $\mathbf{v}$ in $\mathbf{L}^2(\Omega)$ such that $\nabla\cdot\mathbf{v}$ is in $\mathbf{L}^2(\Omega)$. The space is $\mathbf{H}_{\text{div}}(\Omega)$ equipped by the canonical norm (for

which it is a Banach space)

$$\|\mathbf{v}\|_{\mathbf{H}_{\mathrm{div}}(\Omega)} = \left(\|\mathbf{v}\|^2_{\mathbf{L}^2(\Omega)} + \|\nabla{\cdot}\mathbf{v}\|^2_{\mathbf{L}^2(\Omega)}\right)^{\frac{1}{2}}.$$

For $\mathbf{v} \in \mathbf{H}_{\mathrm{div}}(\Omega)$ and $\phi \in H^1(\Omega)$, we have the following integration by parts formula

$$\int_\Omega (\nabla{\cdot}\mathbf{v})\phi + \int_\Omega \mathbf{v}\cdot\nabla\phi = \int_{\partial\Omega} (\mathbf{v}\cdot\mathbf{n})\phi \tag{3.10}$$

where $\mathbf{v}\cdot\mathbf{n}$ is the normal trace, please refer to [43, Theorem 3.24] for details.

Finally, because this thesis deals with time dependent problems, we also introduce suitable notation for those. Whenever E is a normed space with norm $\|\cdot\|_E$, we say a function $\psi : [0,T] \to E$ belongs to $L^p((0,T);E)$ if the map $(0,T) \ni t \mapsto \|\psi(t)\|$ is L^p integrable, see [20] for more details. When introducing a time disctretization, we denote by $\Delta t > 0$ a time step and set $t^n := n\Delta t, n \geq 0$. Also for any time dependent function $\psi : [0,T] \to E$, we denote $\psi^n := \psi(t^n)$.

3.4 Variational Weak Form

We now return to obtain the continous weak form of the MHD system (3.7)-(3.8), and we start by defining the following Hilbert spaces

$$\mathbf{H}^1(\Omega_{cf}) = \left\{\mathbf{v} \in \mathbf{L}^2(\Omega_{cf}), \nabla\mathbf{v} \in \mathbf{L}^2(\Omega_{cf})\right\}, \quad L^2_{\int=0}(\Omega_{cf}) = \left\{q \in L^2(\Omega_{cf}), \int_{\Omega_{cf}} q = 0\right\},$$

$$\mathbf{H}^1_0(\Omega_{cf}) = \left\{\mathbf{v} \in \mathbf{H}^1(\Omega_{cf}), \mathbf{v}|_{\Gamma_f} = 0\right\},$$

equipped with the canonical norms. So the Navier-Stokes weak form consists of seeking the pair $(\mathbf{u}, p) \in L^2((0,+\infty);\mathbf{H}^1(\Omega_{cf})) \cap L^2((0,+\infty);L^2_{\int=0}(\Omega_{cf}))$ such that $\mathbf{u}|_{t=0} = \mathbf{u}_0, \mathbf{u}|_{\Gamma_f} = \mathbf{d}$, and for all $(\mathbf{v}, q) \in \mathbf{H}^1_0(\Omega_{cf}) \times L^2_{\int=0}(\Omega_{cf})$ and for almost every

$t \in (0, +\infty)$:

$$\begin{cases} \int_{\Omega_{cf}} (\partial_t \mathbf{u} + (\mathbf{u} \cdot \nabla)\mathbf{u} + \nabla p) \cdot \mathbf{v} \\ - \int_{\Omega_{cf}} {R_{\mathrm{e}}}^{-1} \nabla \mathbf{u} : \nabla \mathbf{v} - \int_{\Omega_{cf}} (\nabla \times \mathbf{H}) \times (\mu \mathbf{H}) \cdot \mathbf{v} + \int_{\Omega_{cf}} q \nabla \cdot \mathbf{u} = 0, \end{cases} \tag{3.11}$$

where $\nabla \mathbf{u} : \nabla \mathbf{v} = \sum_{ij} \partial_i u_j \partial_j u_i$. When the magnetic field $\mathbf{H}^c$ is given and sufficiently smooth existence of weak solutions of (3.11) is known, see [63].

Let us now proceed with the continuous weak form of Maxwell equations. For the time being and without loss of generality, let us assume we do not have Dirichlet boundary conditions for $\mathbf{H}^c$, i.e, $\Gamma_{c,d} = \emptyset$, and define the spaces

$$\begin{aligned} \mathbf{L} &= \left\{ (\mathbf{b}, \phi) \in \mathbf{L}^2(\Omega_c) \times H^1_{\int=0}(\Omega_v) \right\} \\ \mathbf{X} &= \left\{ (\mathbf{b}, \phi) \in \mathbf{H}_{\mathrm{curl}}(\Omega_c) \times H^1_{\int=0}(\Omega_v); (\mathbf{b} \times \mathbf{n}^c + \nabla \phi \times \mathbf{n}^v)|_{\Sigma} = 0 \right\}, \end{aligned}$$

so the problem is to seek the pair $(\mathbf{H}, \phi) \in L^2((0, +\infty); \mathbf{X}) \cap L^\infty((0, +\infty); \mathbf{L})$ such that $\mathbf{H}|_{t=0} = \mathbf{H}_0, \nabla \phi|_{t=0} = \nabla \phi_0$, and for all pairs $(\mathbf{b}, \psi) \in \mathbf{X}$ and for almost every $t \in (0, +\infty)$:

$$\begin{cases} \int_{\Omega_c} \left[\partial_t (\mu^c \mathbf{H}^c) \cdot \mathbf{b} + (R_{\mathrm{m}}^{-1} \sigma^{-1} (\nabla \times \mathbf{H}^c - \mathbf{j}^s) - \tilde{\mathbf{u}} \times (\mu^c \mathbf{H}^c)) \cdot \nabla \times \mathbf{b} \right] \\ + \int_{\Omega_v} \mu^v \partial_t (\nabla \phi) \cdot \nabla \psi \\ + \int_{\Sigma_\mu} \left\{ R_{\mathrm{m}}^{-1} \sigma^{-1} (\nabla \times \mathbf{H}^c - \mathbf{j}^s) - \tilde{\mathbf{u}} \times (\mu^c \mathbf{H}^c) \right\} \cdot (\mathbf{b}_1 \times \mathbf{n}_1^c + \mathbf{b}_2 \times \mathbf{n}_2^c) \\ + \int_{\Sigma} \left(R_{\mathrm{m}}^{-1} \sigma^{-1} (\nabla \times \mathbf{H}^c - \mathbf{j}^s) - \tilde{\mathbf{u}} \times (\mu^c \mathbf{H}^c) \right) \cdot (\mathbf{b} \times \mathbf{n}^c + \nabla \psi \times \mathbf{n}^v) \\ = \int_{\Gamma_c} (\mathbf{a} \times \mathbf{n}) \cdot (\mathbf{b} \times \mathbf{n}) + \int_{\Gamma_v} (\mathbf{a} \times \mathbf{n}) \cdot (\nabla \psi \times \mathbf{n}), \end{cases} \tag{3.12}$$

the integrals over Σ and Σ_μ are zero, but when non-conforming finite element approximations are used these integrals do not vanish. When $\tilde{\mathbf{u}}$ is a given and smooth

function, existence of weak solutions of (3.12) is known, see [19, p. 313]. Existence of weak solutions of the couple MHD system is known when $\Omega_v = \emptyset$, but to prove uniqueness, smoothness assumptions must be made, see [24]. When $\Omega_v \neq \emptyset$ existence of weak solutions is an open problem, nevertheless it is assumed in this thesis.

When the velocity $\tilde{\mathbf{u}}$ is given the MHD system (3.11)-(3.12) reduces to solve only Maxwell equations. This is the so-called kinematic dynamo problem, and for the rest of this section we focus only in this problem. In section 6 we discuss the discretization of the Navier-Stokes equations and the full MHD problem, respectively. We now proceed to discuss the discretization of the weak problem (3.12).

3.5 Finite Element Approximation

Let (r, θ, z) be the polar coordinates and t be the time variable. Assuming that Ω is an axisymmetric domain such that $\Omega \subset \mathbb{R}^3$, we choose to use spectral approximation in the azimuthal direction θ and finite elements in the meridional plane (r, z). This is called the Fourier finite element method, see [6, 33] for details. The generic form of approximate function is

$$f(r, \theta, z, t) = \sum_{k=-M}^{M} f_h^k(r, z, t) \mathrm{e}^{ik\theta}, \tag{3.13}$$
$$\mathrm{i}^2 = -1, \quad \overline{f_h^k}(r, z, t) = f_h^{-k}(r, z, t) \quad \forall k \in \overline{0, M},$$

where $M + 1$ is the maximum number of complex Fourier modes. The coefficients $f_h^k(r, z, t)$ take values in the appropriate finite element space.

As we have seen in the previous subsection the Navier-Stokes and Maxwell equations in the MHD setting are coupled, and this makes the choice of finite elements problematic. For instance, a natural choice for Navier-Stokes is to use the so-called Taylor-Hood finite elements, which consist of using Lagrange finite elements for $\mathbf{v}$

and p. However, using Lagrange elements and controlling the condition $\nabla\cdot(\mu\mathbf{H})$ in $L_2(\Omega)$ for Maxwell problems is dangerous due to the fact that such elements could not converge, see Costabel [13]. On the other hand, a natural choice of finite elements for Maxwell problems are the so called Nedelec-elements; these elements rely on edge interpolation which is cumbersome for Navier-Stokes problems.

There are several approaches that have successfully circumvent the problem of using Lagrange elements for Maxwell equations in the low frequency regime, see [3, 8, 9, 10, 14, 31]. The methods introduced in Bonito and Guermond [8] and more recently in Bonito *et al.* [9] solve the Maxwell eigenvalue problem using Lagrange elements, and controlling weakly the condition $\nabla\cdot(\mu\mathbf{H})$ in the dual space of $H_0^s(\Omega)$ where $\frac{1}{2} < s \leq 1$. Using these ideas a pseudo spectral Fourier-Finite element method has been proposed in Guermond *et al.* [31] to solve (3.12). This novel approach accounts for discontinuous μ as well and it is implemented in the open source code called `SFEMaNS` (for Spectral Finite Elements for Maxwell and Navier-Stokes equations). This code has been validated for non-trivial MHD applications [26, 38]. However, the main restriction of the approach in [31] is that μ has to be axisymmetric. Overcoming this restriction is a non-trivial problem, and one of the goals of this thesis. Sections 5 and 6 give full details of how to handle non-axisymmetric μ. Nevertheless, for the sake of introduction and completeness, we continue describing the original numerical scheme implemented in the code `SFEMaNS` which handles only piecewise-constant axisymmetric μ. In the last subsection, numerical convergence tests are presented which are used for comparisons in section 5, where a different variational form of (3.8) and a new numerical discretization are introduced.

3.5.1 Space Discretization for the Geometry

As mentioned before, we assume Ω is axisymmetric, so we denote by ${\Omega_v}^{\rm 2D}, {\Omega_c}^{\rm 2D}$ and $\Omega_{ci}^{\rm 2D} (i = 1, \ldots, N)$, the meridional sections of Ω_v, Ω_c and Ω_{ci}, respectively. We assume that Ω_v, Ω_c and Ω_{ci} have piecewise quadratic boundaries. These sections are meshed using quadratic triangular meshes.

We denote by $\{\mathcal{F}_h^v\}_{h>0}, \{\mathcal{F}_h^c\}_{h>0}$ and $\{\mathcal{F}_h^{ci}\}_{h>0}$ the corresponding regular families of non-overlappping quadratic triangular meshes. We assume that for every given mesh index h, $\mathcal{F}_h^{ci}$ is a subset of $\mathcal{F}_h^c$. We denote by $\Sigma_h^{\rm 2D}$ and $\Sigma_{\mu h}^{\rm 2D}$ the collection of triangles faces that compose the meridional section of Σ and Σ_μ, respectively. The collection of cylindrical surfaces generated by rotation around the symmetry axis by the faces in $\Sigma_h^{\rm 2D}$ and $\Sigma_{\mu h}^{\rm 2D}$ are denoted by Σ and Σ_μ, respectively. For every cylindrical surface F in $\Sigma \cup \Sigma_\mu$, we denote by h_F the diameter of the triangle face that generates F.

For every element K in the mesh $\mathcal{F}_h^v \cup \mathcal{F}_h^c$ we denote by $T_K : \hat{K} \to K$ the quadratic transformation that maps the reference triangle $\hat{K} := \{(r, z) \in \mathbb{R}^2, 0 \leq \hat{r}, 0 \leq \hat{z}, \hat{r} + \hat{z} \leq 1\}$ to K, and we denote by h_K, the diameter of K. Finally, we denote by $K^{\rm 3D}$ the volume generated by rotation around the symmetry axis by an element K.

3.5.2 Space Discretization of Maxwell Equations

Let $\ell_{\mathbf{H}}$ and ℓ_ϕ be two integers in $\{1, 2\}$ with $\ell_\phi \geq \ell_{\mathbf{H}}$. We define the meridional finite element spaces as follows,

$$\mathbf{X}_h^{\mathbf{H},2D} := \{\mathbf{b}_h \in \mathbf{L}^2(\Omega_c);\, \mathbf{b}_h|_{\Omega_{ci}} \in \boldsymbol{\mathcal{C}}^0(\overline{\Omega_{ci}}), \forall i = 1, \ldots, N, \mathbf{b}_h(T_K)|_K \in \mathbb{P}_{\ell_{\mathbf{H}}},\ \forall K \in \mathcal{F}_h^c\},$$

$$X_h^{\phi,2D} := \{\varphi_h \in \mathcal{C}^0(\overline{\Omega_v});\, \varphi_h(T_K)|_K \in \mathbb{P}_{\ell_\phi},\ \forall K \in \mathcal{F}_h^v\},$$

where $\mathbb{P}_k$ denotes the set of bivariate polynomials of total degree at most k, and $\mathbb{P}_k := \mathbb{P}_k \times \mathbb{P}_k \times \mathbb{P}_k$. Then, using the complex notation $\mathrm{i}^2 = -1$, the field $\mathbf{H}$ and the scalar potential ϕ are approximated in the following spaces:

$$\mathbf{X}_h^{\mathbf{H}} := \{\mathbf{b} = \sum_{m=-M}^{M} \mathbf{b}_h^m(r,z)e^{\mathrm{i}m\theta};\, \mathbf{b}_h^m \in \mathbf{X}_h^{\mathbf{H},2D},\ \overline{\mathbf{b}_h^m} = \mathbf{b}_h^{-m},\ k \in \overline{0,M}\},$$

$$X_h^{\phi} := \{\varphi = \sum_{m=-M}^{M} \varphi_h^m(r,z)e^{\mathrm{i}m\theta};\, \varphi_h^m \in X_h^{\phi,2D},\ \overline{\varphi_h^m} = \varphi_h^{-m},\ m \in \overline{0,M}\},$$

where $M+1$ is the maximum number of complex Fourier modes.

As in [31] we introduce the magnetic pressure p^c to control the divergence condition $\nabla\cdot(\mu^c\mathbf{H}) = 0$ weakly in the dual space of $H_0^s(\Omega)$ where $\frac{1}{2} < s \leq 1$. So we define the following finite element spaces,

$$X_h^{p,2D} := \left\{p_h \in L^2(\Omega_c) \,/\, p_h \in \mathcal{C}^0(\overline{\Omega_c}),\ p_h(T_K) \in \mathbb{P}_{\ell_p},\ \forall K \in \mathcal{F}_h^c,\ p_h = 0 \text{ on } \partial\Omega_c\right\},$$

$$X_h^{p} := \left\{p = \sum_{m=-M}^{M} p_h^m(r,z)\mathrm{e}^{\mathrm{i}m\theta} \,/\, \forall m = 1\ldots,M,\ p^m \in X_h^{p,2D} \text{ and } p_h^m = \overline{p_h^{-m}}\right\},$$

where ℓ_p is an integer in {1,2}.

3.5.3 Time Discretization

We now proceed to describe the time stepping scheme used originally in the code `SFEMaNS` and reported in [29, 30, 31] to discretize (3.12). First of all let us drop the assumption of not having Dirichlet boundary conditions, i.e, let us assume $\Gamma_{c,d} \neq \emptyset$. Now, the time derivatives of $\mathbf{H}^c$ and ϕ are approximated using Backward Difference of second order formula (BDF2), and after proper initialization at t^0 and t^1, we define

$$D\mathbf{H}^{c,n+1} = \frac{1}{2}(3\mathbf{H}^{c,n+1} - 4\mathbf{H}^{c,n} + \mathbf{H}^{c,n-1}), \tag{3.14}$$

and

$$\mathbf{H}^{*} = 2\mathbf{H}^{c,n} - \mathbf{H}^{c,n-1}. \tag{3.15}$$

Observe that for any sufficiently smooth function and using Taylor series we have $\mathbf{H}^{c,n+1} = \mathbf{H}^{*} + \mathcal{O}(\Delta t^2)$, this identity is used extensively in this thesis, and its stability properties are deeply studied in section 4. Then the solution of the Maxwell problem (3.12) is computed in one step by solving $\mathbf{H}^{c,n+1} \in \mathbf{X}_h^{\mathbf{H}}$, $\phi^{n+1} \in X_h^{\phi}$ and $p^{c,n+1} \in X_h^{p}$, so that the following holds for all $\mathbf{b} \in \mathbf{X}_h^{\mathbf{H}}$, $\varphi \in X_h^{\phi}$ and $q \in X_h^{p}$,

$$\begin{cases} \mathbf{H}^{c}|_{t=0} = \mathbf{H}_0^{c}, \\ \int_{\Omega_c} \mu^{c} \frac{D\mathbf{H}^{c,n+1}}{\Delta t} \cdot \mathbf{b} + \int_{\Omega_v} \mu^{v} \frac{\nabla D\phi^{n+1}}{\Delta t} \cdot \nabla\varphi + \mathcal{L}((\mathbf{H}^{c,n+1}, \phi^{n+1}), (\mathbf{b}, \varphi)) \\ + \mathcal{P}(\phi^{n+1}, \varphi) + \mathcal{D}((\mathbf{H}^{c,n+1}, p^{n+1}), (\mathbf{b}, q)) + \mathcal{E}(\mathbf{H}^{c,n+1}, \mathbf{b}) = \mathcal{R}_n(\mathbf{b}, \varphi), \end{cases} \tag{3.16}$$

where,

$$\begin{aligned} \mathcal{L}((\mathbf{H}, \phi), (\mathbf{b}, \varphi)) = & \int_{\Omega_c} \frac{1}{\sigma R_m} \nabla\times\mathbf{H} \cdot \nabla\times\mathbf{b} + \int_{\Sigma_\mu} \left\{ \frac{1}{\sigma R_m} \nabla\times\mathbf{H} \right\} \cdot (\mathbf{b}_1 \times \mathbf{n}_1^{c} + \mathbf{b}_2 \times \mathbf{n}_2^{c}) \\ & + g((\mathbf{H}, \phi), (\mathbf{b}, \varphi)) + \int_{\Sigma} \frac{1}{\sigma R_m} \nabla\times\mathbf{H} \cdot (\mathbf{b} \times \mathbf{n}^{c} + \nabla\varphi \times \mathbf{n}^{v}) \,. \end{aligned}$$

The bilinear form $g((\mathbf{H}, \phi), (\mathbf{b}, \varphi))$ penalizes the jumps conditions on Σ and Σ_μ

using the so-called Interior Penalty Method (IPM) see [2],

$$
\begin{aligned}
g((\mathbf{H},\phi),(\mathbf{b},\varphi)) = \beta_3 \sum_{F\in\Sigma_\mu} h_F^{-1} \int_F (\mathbf{H}_1\times\mathbf{n}_1^c + \mathbf{H}_2\times\mathbf{n}_2^c)\cdot(\mathbf{b}_1\times\mathbf{n}_1^c + \mathbf{b}_2\times\mathbf{n}_2^c) \\
+ \beta_1 \sum_{F\in\Sigma_\mu} h_F^{-1} \int_F (\mu_1^c\mathbf{H}_1\cdot\mathbf{n}_1^c + \mu_2^c\mathbf{H}_2\cdot\mathbf{n}_2^c)\cdot(\mu_1^c\mathbf{b}_1\cdot\mathbf{n}_1^c + \mu_2^c\mathbf{b}_2\cdot\mathbf{n}_2^c) \\
+ \beta_2 \sum_{F\in\Sigma} h_F^{-1} \int_F (\mathbf{H}\times\mathbf{n}_1^c + \nabla\phi\times\mathbf{n}_2^c)\cdot(\mathbf{b}\times\mathbf{n}^c + \nabla\varphi\times\mathbf{n}^v) \\
+ \beta_1 \sum_{F\in\Sigma} h_F^{-1} \int_F (\mu^c\mathbf{H}\cdot\mathbf{n}_1^c + \nabla\phi\cdot\mathbf{n}_2^c)\cdot(\mu^c y\mathbf{b}\cdot\mathbf{n}^c + \nabla\varphi\cdot\mathbf{n}^v)\,,
\end{aligned}
$$

where $\beta_1, \beta_2, \beta_3$ are penalization constant parameters and user dependent. We usually take $\beta_3 = \beta_2 = \beta_1$ and,

$$\beta_1 = \frac{1}{R_m \min_{\mathbf{x}\in\Omega_c}(\sigma(\mathbf{x}))}.$$

This scaling can be justified by arguments from the Interior Penalty Theory [2, 4, 30, 31]. Now, the bilinear form $\mathcal{P}(\phi,\varphi)$ is defined as

$$\mathcal{P}(\phi,\varphi) = \int_{\Omega_v} \mu^v \nabla\phi\cdot\nabla\varphi - \int_{\partial\Omega_v} \mu^v\varphi\mathbf{n}\cdot\nabla\phi,$$

this is a stabilization form due to the introduction of the magnetic pressure p^c, see [31]. The bilinear form $\mathcal{D}((\mathbf{H},p),(\mathbf{b},q))$ controls the divergence condition $\nabla\cdot(\mu^c\mathbf{H}) = 0$ weakly in Ω_c,

$$
\begin{aligned}
\mathcal{D}((\mathbf{H},p),(\mathbf{b},q)) =& \beta_1\cdot\left(\int_{\Omega_c}\mu^c\nabla p\cdot\mathbf{b} - \int_{\Omega_c}\mu^c\mathbf{H}\cdot\nabla q + \sum_{K\in\mathcal{F}_h^c}\int_{K^{3D}} h_K^{2(1-\alpha)}\nabla p\cdot\nabla q\right) \\
&+ \beta_1\cdot\sum_{K\in\mathcal{F}_h^c} h_K^{2\alpha}\int_{K^{3D}}\nabla\cdot(\mu^c\mathbf{H})\nabla\cdot(\mu^c\mathbf{b}) \qquad (3.17)
\end{aligned}
$$

where α is real number such that $\alpha\in[0.6, 0.8]$, see [8, 31]. All the computations

done in this thesis we have used $\alpha = 0.6$.

The bilinear form $\mathcal{E}(\mathbf{H}, \mathbf{b})$ imposes the Dirichlet boundary conditions on $\Gamma_{c,d}$ using interior penalty method as well,

$$\mathcal{E}(\mathbf{H}, \mathbf{b}) = \int_{\Gamma_{c,d}} \frac{1}{\sigma R_m} (\nabla \times \mathbf{H}) \cdot (\mathbf{b} \times \mathbf{n}^c) + \beta_4 \left(\sum_{F \in \Gamma_{c,d}} h_F^{-1} \int_F (\mathbf{H} \times \mathbf{n}^c) \cdot (\mathbf{b} \times \mathbf{n}^c) \right), \tag{3.18}$$

where β_4 is a user dependent parameter. Finally, the right hand side bilinear form $\mathcal{R}_n(\mathbf{b}, \varphi)$ is defined as

$$\begin{aligned} \mathcal{R}_n(\mathbf{b}, \varphi) = & \int_{\Sigma_\mu} \left\{ \frac{1}{\sigma R_m} \mathbf{j}^s + \tilde{\mathbf{u}} \times (\mu^c \mathbf{H}^*) \right\} \cdot (\mathbf{b}_1 \times \mathbf{n}_1^c + \mathbf{b}_2 \times \mathbf{n}_2^c) \\ & + \int_{\Omega_c} \left(\frac{1}{\sigma R_m} \mathbf{j}^s + \tilde{\mathbf{u}} \times (\mu^c \mathbf{H}^*) \right) \cdot \nabla \times \mathbf{b} \\ & + \int_{\Sigma} \left(\frac{1}{\sigma R_m} \mathbf{j}^s + \tilde{\mathbf{u}} \times (\mu^c \mathbf{H}^*) \right) \cdot (\mathbf{b} \times \mathbf{n}^c + \nabla \varphi \times \mathbf{n}^v) \\ & + \int_{\Gamma_{c,n}} (\mathbf{a} \times \mathbf{n}) \cdot (\mathbf{b} \times \mathbf{n}) + \int_{\Gamma_v} (\mathbf{a} \times \mathbf{n}) \cdot (\nabla \varphi \times \mathbf{n}), + \mathcal{H}_n(\mathbf{b}), \end{aligned}$$

where the linear form $\mathcal{H}_n(\mathbf{b})$ is defined as

$$\mathcal{H}_n(\mathbf{b}) = \int_{\Gamma_{c,d}} \left(\frac{1}{\sigma R_m} \mathbf{j}^s + \tilde{\mathbf{u}} \times (\mu^c \mathbf{H}^*) \right) \cdot (\mathbf{b} \times \mathbf{n}^c) + \beta_4 \left(\sum_{F \in \Gamma_{c,d}} h_F^{-1} \int_F (\mathbf{H}_d^c \times \mathbf{n}^c) \cdot (\mathbf{b} \times \mathbf{n}^c) \right),$$

which last term balances against the bilinear form $\mathcal{E}(\mathbf{H}, \mathbf{b})$.

3.6 Convergence Tests

As mentioned before, the original numerical scheme implemented in the code `SFEMaNS` handled only piecewise-constant axisymmetric μ. And as a part of the work of this thesis, `SFEMaNS` has been extended to handle piecewise-smooth axisymmetric μ. This worked as a starting point when μ is non-axisymmetric. We now test our implementation with two manufactured solutions.

3.6.1 Maxwell Equations with Vacuum

We construct an analytical solution for the system (3.8) defining first the magnetic field $\mathbf{H}$ and the magnetic permeablity μ by

$$\mathbf{H} = \begin{cases} \mathbf{H}^c & \text{in} \quad \Omega_c \\ \nabla\psi & \text{in} \quad \Omega_v \end{cases} \quad \text{and} \quad \mu = \begin{cases} \mu^c & \text{in} \quad \Omega_c \\ 1 & \text{in} \quad \Omega_v \end{cases} . \tag{3.19}$$

For this particular test we set $\mu^c = \mu^c(r, z)$, but μ^c is not allowed to have jumps in Ω_c, so $\Sigma_\mu = \emptyset$. Let us set Ω_c as a cylinder located at the origin with radius 1 and height 2; specifically, let $\Omega_c = \{(r, \theta, z) \in R^3 : (r, \theta, z) \in [0, 1] \times [0, 2\pi) \times [-1, 1]\}$, and let $\Omega_v = \{(r, \theta, z) \in R^3 : r^2 + z^2 = 10^2, \theta \in [0, 2\pi)\} \setminus \Omega_c$. Now, let us set

$$\mathbf{H} = \frac{1}{\mu^c}\nabla\psi, \tag{3.20}$$

in (3.19) where $\psi = \psi(r, z)$ such that it satisfies the Laplace equation in cylindrical coordinates; namely,

$$\partial_{rr}\psi + \frac{1}{r}\partial_r\psi + \partial_{zz}\psi = 0. \tag{3.21}$$

If we also set $\mathbf{j} = \nabla \times \mathbf{H}$, $\mathbf{u} = 0$, then $\mathbf{E} = \mathbf{0}$,and $\mathbf{H}$ satisfies (3.8). Now let us

define

$$\mu^c = \mu^c(r,z) = \frac{1}{f(r,z)+1},$$

where

$$f(r,z) = b \cdot r^3 \cdot (1-r)^3 \cdot (z^2-1)^3,$$

and b is a non-negative constant parameter which determines the variation of μ^c. Observe that $\mu^c = 1$ at $(r,z) = (1,\pm 1)$, then $\mu^c = 1$ at Ω_v. So we can set $\mu^c = \mu$, and by using (3.19) allows us to have vacuum, and μ has no jumps on Ω as required. Also notice that $f(r,z) \leq 0$ for $(r,\theta,z) \in \Omega_c$ and

$$\sup_{\Omega_c} f(r,z) = f_{\max} = 0, \quad \inf_{\Omega_c} f(r,z) = f_{\min} = -\frac{b}{2^6},$$

then

$$\mu^c_{\min} = \frac{1}{1+f_{\max}}, \quad \mu^c_{\max} = \frac{1}{1+f_{\min}}, \quad r_\mu = \frac{\mu_{\max}}{\mu_{\min}} = \frac{\frac{1}{1-\frac{b}{2^6}}}{1}, \quad \text{and} \quad b = 2^6\left(1-\frac{1}{r_\mu}\right).$$

To get an explicit solution in (3.20), equation (3.21) is solved using separation of variables, that is, letting $\psi(r,z) = R(r)Z(z)$ we solve the following system of ODEs,

$$\begin{aligned} Z'' - \lambda Z &= 0 \\ R'' + \frac{R'}{r} + \lambda R &= 0, \end{aligned}$$

where λ is any real number. Here we choose $\lambda = 1$, so

$$\psi(r, z) = J_0(r)\cosh(z). \tag{3.22}$$

Now, using $J_0'(r) = -J_1(r)$ and $\cosh'(z) = \sinh(z)$ we get,

$$\nabla\psi = \begin{bmatrix} -J_1(r)\cosh(z) \\ 0 \\ J_0(r)\sinh(z) \end{bmatrix},$$

then using (3.20) we compute,

$$\mathbf{H}^c = (f(r, z) + 1) \begin{bmatrix} -J_1(r)\cosh(z) \\ 0 \\ J_0(r)\sinh(z) \end{bmatrix}. \tag{3.23}$$

Denoting by $\mathbf{H}_h$ the approximate magnetic field, we report in tables 3.1a and 3.1b the relative errors using the code `SFEMaNS`. These tables also show the computed order of convergence (COC). For this test $\mathbb{P}_2, \mathbb{P}_2$ and $\mathbb{P}_1$ Lagrange elements are employed for $\mathbf{H}_h^c, \phi_h$ and p_h^c, respectively. Moreover, since solution (3.23) is in Fourier space with mode $m = 0$, scheme (3.16) is used only for this mode. The convergence rate observed in table 3.1a is optimal according with the theory, see Bonito *et al.* [9, Theorem 5.1], while superconvergence is observed in table 3.1b.

h	$\|\nabla\cdot(\mu\mathbf{H})_h\|_{L^2}$	COC	$\|\nabla\times(\mathbf{H}-\mathbf{H}_h)\|_{L^2}$	COC
0.4	4.3217E-01	—	1.5558E-01	—
0.2	1.5331E-01	1.50	3.9268E-02	1.99
0.1	8.6974E-02	0.82	1.2243E-02	1.68
0.05	1.6816E-02	2.37	1.6855E-03	2.86
0.025	5.5347E-03	1.60	5.2292E-04	1.69

(a)

h	$\|\mathbf{H}-\mathbf{H}_h\|_{L^2}$	COC	$\|\phi-\phi_h\|_{H^1}$	COC
0.4	5.3699E-01	—	2.7142E-02	—
0.2	1.4000E-01	1.94	8.5094E-03	1.67
0.1	1.8230E-02	2.94	1.0826E-03	2.97
0.05	1.0800E-03	4.08	5.0390E-05	4.43
0.025	8.8350E-05	3.61	3.4253E-06	3.88

(b)

Table 3.1: Numerical errors computed when vacuum is nonempty, and μ is axisymmetric using scheme (3.16).

3.6.2 Maxwell Equations with Jumps in μ

In this test we do not have vacuum, i.e, $\Omega_v = \emptyset$, but we allow μ^c to have jumps. We first begin setting $\mathbf{u} = 0$, $\mathbf{E} = 0$, and $\Omega_c = \Omega_{c,1} \cup \Omega_{c,2}$, where

$$\Omega_{c,1} = \{(r,\theta,z) \in R^3 : (r,\theta,z) \in [0,1] \times [0,2\pi) \times [1/4,1]\},$$

and

$$\Omega_{c,2} = \{(r,\theta,z) \in R^3 : (r,\theta,z) \in [1,2] \times [0,2\pi) \times [1/4,1]\}.$$

Let $\lambda_\mu = 10$ and set

$$\mathbf{H}^c = \begin{bmatrix} H_r \\ 0 \\ H_z \end{bmatrix}, \tag{3.24}$$

where

$$H_r = \begin{cases} H_{1,r} = rz & \text{in} \quad \Omega_{c,1}, \\ H_{2,r} = \frac{rz^3(3r+2)}{3z^2r+2z^2+2\lambda_\mu} & \text{in} \quad \Omega_{c,2}, \end{cases} \qquad \text{and} \qquad H_z = -\frac{1}{2}\frac{z^2(3r+2)}{1+r}.$$

We now define the magnetic permeability as

$$\mu^c = \mu^c(r,z) = \begin{cases} \mu_1 = 1 + r & \text{in} \quad \Omega_{c,1}, \\ \mu_2 = \mu_1 + \frac{2\lambda_\mu(1+r)}{z^2(3r+2)} & \text{in} \quad \Omega_{c,2}, \end{cases}$$

so we can see that μ^c has a jump, so $\Sigma_\mu \neq \emptyset$. Finally using $\mathbf{H}^c$ as in (3.24) for Dirichlet boundary conditions, the Maxwell equations (3.8) are satisfied. Denoting by $\mathbf{H}_h$ the approximate magnetic field using scheme (3.16), we report in table 3.2 the relative errors, and the computed order of convergence (COC) using `SFEMaNS`. For this test $\mathbb{P}_2$, and $\mathbb{P}_1$ Lagrange elements are used for $\mathbf{H}_h^c$ and p_h^c, respectively. Moreover, since the solution is in Fourier space with mode $m = 0$, scheme (3.16) is used only for this mode. All convergence rates observed in table 3.2 exceeds by almost one the theoretical rate, see Bonito *et al.* [9, Theorem 5.1].

h	$\|\nabla\cdot(\mu\mathbf{H})_h\|_{L^2}$	COC	$\|\nabla\times(\mathbf{H}-\mathbf{H}_h)\|_{L^2}$	COC	$\|\mathbf{H}-\mathbf{H}_h\|_{L^2}$	COC
0.2	2.6728E-01	—	7.6497E-01	—	5.1926E-01	—
0.1	3.6544E-02	2.87	6.9674E-02	3.46	4.2544E-02	3.61
0.05	9.9811E-03	1.87	8.3591E-03	3.06	1.5756E-03	4.76
0.025	1.7801E-03	2.49	1.4059E-03	2.57	5.7830E-05	4.77
0.0125	2.6337E-04	2.76	1.9085E-04	2.88	2.1993E-06	4.72

Table 3.2: Numerical errors computed when μ is axisymmetric, and has jumps using scheme (3.16).

3.7 A Simpler Model Proposed for Maxwell Equations

To illustrate and understand what is the main difficulty of using hybrid Fourier-Finite elements for Maxwell equations when μ is non-axisymmetric, we propose to study the following simpler model which is similar to the first equation of the Maxwell system (3.8),

$$\begin{cases} \partial_t(\mu u) - \nabla\cdot(\nabla u) = f(\mathbf{x},t) & \mathbf{x}\in\Omega, 0<t\leq T, \\ u(\mathbf{x},t) = 0 & \mathbf{x}\in\Omega, 0<t\leq T, \\ u(\mathbf{x},0) = u^0 & \text{in } \Omega, \end{cases} \tag{3.25}$$

where u is the unknown scalar field, and for the time being $\mu = \mu(r,\theta,z)$. We assume that Ω has smooth boundary, and the functions f, μ and u_0 are smooth. Let Δt be the time step and set $t^n := n\Delta t, n \geq 0$. Denoting u^n as an approximation of u at time t_n, we discretize (3.25) using the backward Euler (BDF1) time scheme,

$$\frac{\mu u^{n+1} - \mu u^n}{\Delta t} - \nabla\cdot\left(\nabla u^{n+1}\right) = f^{n+1}. \tag{3.26}$$

Now, introducing the Fourier representation (3.13)

$$u(r,\theta,z) \approx \sum_{|k|=0}^{M} \hat{u}_k(r,z)e^{ik\theta}, \quad \text{and} \quad (\mu u)(r,\theta,z) \approx \sum_{|k|=0}^{M} (\mu u)_k^{\wedge}(r,z)e^{ik\theta},$$

we get the weak form of (3.26) which is to find $(u^{n+1})_k^{\wedge}$ in some abstract space V such that

$$\begin{aligned} &\frac{1}{\Delta t}\int_{\hat{\Omega}} \left((\mu u^{n+1})_k^{\wedge} - (\mu u^n)_k^{\wedge} \right) \hat{\psi} r dr dz \\ &\quad + \int_{\hat{\Omega}} \nabla_{rz} \hat{u}_k^{n+1} \cdot \nabla_{rz} \hat{\psi} r dr dz \\ &\quad + \int_{\hat{\Omega}} \frac{k^2}{r} \hat{u}_k^{n+1} \hat{\psi} dr dz = \int_{\hat{\Omega}} \hat{f}_k^{n+1} \hat{\psi} r dr dz, \quad \forall \hat{\psi} \in V \quad \text{and} \quad k = 0, \pm 1, ..., \pm M, \end{aligned} \tag{3.27}$$

where $\hat{\Omega}$ is the meridional plane, and $\nabla_{rz} u = (\partial_r u)\mathbf{e}_r + (\partial_z u)\mathbf{e}_z$. The main difficulty of the weak form (3.27) is the implicit term $(\mu u^{n+1})_k^{\wedge}$ involving a convolution between $(u^{n+1})_k^{\wedge}$ and $\hat{\mu}_k$. This breaks the parallelization in the linear algebra; specifically, when finite elements are used to discretize $\hat{\Omega}$, the resultant matrix is full rather than decoupled mode by mode. Due to this difficulty, we propose a change of variables and study the following model

$$\begin{cases} \partial_t v - \nabla \cdot (\nabla (\eta v)) = f(\mathbf{x}, t) & \mathbf{x} \in \Omega, 0 < t \leq T, \\ v(\mathbf{x}, t) = 0 & \mathbf{x} \in \Omega, 0 < t \leq T, \\ v(\mathbf{x}, 0) = v^0 & \text{in } \Omega, \end{cases} \tag{3.28}$$

where $v = \mu u$ and $\eta = \mu^{-1}$. Time stepping schemes avoiding implicit convolutions for the parabolic problem (3.28) are proposed and studied in the following section. The case when η is time dependent is treated as well.

4. EFFICIENT SECOND ORDER BACKWARD DIFFERENCE SCHEME FOR PARABOLIC PROBLEMS WITH VARIABLE COEFFICIENTS

The purpose of this section is to find and analyze efficient time stepping schemes for the model

$$\begin{cases} \partial_t v - \nabla \cdot (\nabla (\eta v)) = f(\mathbf{x}, t) & \mathbf{x} \in \Omega, 0 < t \leq T, \\ v(\mathbf{x}, t) = 0 & \mathbf{x} \in \Omega, 0 < t \leq T, \\ v(\mathbf{x}, 0) = v^0 & \text{in } \Omega, \end{cases} \tag{4.1}$$

where η only depends on space. As discussed in subsection 3.7, the model (4.1) mimics the first equation of the Maxwell system (3.8), so it is natural to begin analyzing this PDE. By efficient time stepping schemes we mean schemes that use time independent matrices, and avoid implicit convolutions when hybrid Fourier-finite elements are employed. Two time stepping schemes are proposed with those properties for (4.1). One of first order, and one of second order in time. Their stability is proved in subsection 4.1.2 for sufficiently small time steps Δt. Then numerical experiments are performed using these efficient schemes when $\Omega \subset \mathbb{R}^d$ for $d = 2, 3$.

It is worth mentioning that when $\eta = \eta(\mathbf{x})$, model (4.1) mimics the kinematic dynamo problem of the VKS experiment, which is studied in section 5. Let us recall that the kinematic dynamo problem consists in solving only Maxwell equations (3.8) when the fluid velocity $\mathbf{u}$ is given. The case for time dependent η mimics the case when we have moving blades, which corresponds to a full MHD-VKS simulation problem where the magnetic field $\mathbf{H}$ and $\mathbf{u}$ are unknowns. Since this case is crucial,

in subsection 4.2 we focus our attention on the general scalar parabolic PDE with variable coefficients in time and space; namely,

$$\begin{cases} u_t + A(t)u = f(x,t) & \mathbf{x} \in \Omega, 0 < t \leq T, \\ u(\mathbf{x},t) = 0 & \mathbf{x} \in \partial\Omega, 0 < t \leq T, \\ u(\mathbf{x},0) = u^0 & \mathbf{x} \in \Omega, \end{cases} \tag{4.2}$$

where

$$A(t)u = -\sum_{ij} \frac{\partial}{\partial x_j}\left(\eta_{ij}(\mathbf{x},t)\frac{\partial u}{\partial x_j}\right) + \sum_i \eta_i(\mathbf{x},t)\frac{\partial u}{\partial x_i} + \eta(\mathbf{x},t)u.$$

We propose a novel efficient second order in time scheme to solve (4.2) and prove its stability in subsection 4.2.1. Numerical experiments using this new scheme are presented for $\Omega \subset \mathbb{R}^2$. The standard bibliography to study parabolic PDEs such as (4.2) is Evans [20], and Renardy and Rogers [52]. For details about numerical methods, see the monograph of Thomée [64].

4.1 Simpler Model for Maxwell Equations

In this subsection we focus to solve numerically the following PDE,

$$\begin{cases} \partial_t v - \nabla \cdot (\nabla (\eta v)) = f(\mathbf{x},t) & \mathbf{x} \in \Omega, 0 < t \leq T, \\ v(\mathbf{x},t) = 0 & \mathbf{x} \in \Omega, 0 < t \leq T, \\ v(\mathbf{x},0) = v^0 & \text{in } \Omega, \end{cases} \tag{4.3}$$

where we assume $\Omega \subset \mathbb{R}^d$ for $d = 2, 3$ with smooth boundary $\partial\Omega$, $f \in L^2(\Omega)$ and $v^0 \in H_0^1(\Omega)$. By assumption η depends only in Ω, and it has minimal regularity; namely, $\eta \in W_\infty^1(\Omega)$. Moreover, we assume there exists a positive constant η_0 such

that

$$0 < \eta_0 \leq \inf_{\mathbf{x}\in\Omega} \eta(\mathbf{x}). \tag{4.4}$$

Thus the variational weak form of (4.3) consists of finding $v \in C([0,T]; H_0^1(\Omega))$, with $\partial_t v \in L^2([0,T]; H^{-1}(\Omega))$ such that

$$\begin{cases} \int_\Omega (\partial_t v) w + \int_\Omega \nabla(\eta v) \cdot \nabla w = \int_\Omega f w \quad \forall w \in H_0^1(\Omega), 0 < t \leq T, \\ v(x,0) = v^0, \end{cases} \tag{4.5}$$

where $v^0 \in H_0^1(\Omega)$, and $f : [0,T] \to L^2(\Omega)$. To prove that the above weak problem (4.5) is well defined, let us define the bilinear form

$$A(t,v,w) = \int_\Omega \nabla(\eta v) \cdot \nabla w = \int_\Omega (\eta \nabla v \cdot \nabla w + v \nabla \eta \cdot \nabla w). \tag{4.6}$$

Thus using the fact that $\eta \in W_\infty^1(\Omega)$ we have that

$$|A(t,v,w)| \leq C \|v\|_{H_0^1(\Omega)} \|w\|_{H_0^1(\Omega)}, \tag{4.7}$$

so $A(t,v,w)$ is uniformly bounded. Moreover, using (4.4) we get

$$\begin{aligned} \eta_0 \int_\Omega |\nabla v|^2 &\leq \int_\Omega \eta |\nabla v|^2 \\ &\leq A(t,v,v) - \int_\Omega v \nabla \eta \cdot \nabla v \\ &\leq A(t,v,v) - L \int_\Omega |v||\nabla v|, \end{aligned} \tag{4.8}$$

where $L = \|\nabla \eta\|_{L^\infty(\Omega)}$. Now from Cauchy's inequality with $\epsilon > 0$,

$$ab \leq \epsilon a^2 + \frac{b^2}{4\epsilon} \quad (a, b \in \mathbb{R}), \tag{4.9}$$

we observe that

$$L\int_\Omega |v||\nabla v| \leq \epsilon \int_\Omega |\nabla v|^2 + \frac{L^2}{4\epsilon}\int_\Omega |v|^2,$$

thus inserting this estimate into (4.8) and choosing $\epsilon = \frac{\eta_0}{4}$ we obtain

$$\frac{3\eta_0}{4}\int_\Omega |\nabla v|^2 \leq A(t,v,v) + \frac{L^2}{\eta_0}\int_\Omega |v|^2. \tag{4.10}$$

Moreover, using Poincaré's inequality

$$\|v\| \leq C\|\nabla v\|_{L^2(\Omega)} \quad \text{for} \quad v \in H_0^1(\Omega), \tag{4.11}$$

it follows that

$$c\|v\|_{H_0^1(\Omega)} \leq A(t,v,v) + \lambda\|v\|_{L^2(\Omega)}, \tag{4.12}$$

for some appropiate constant $c > 0$ and $\lambda = \frac{L^2}{\eta_0} \geq 0$. Inequality (4.12) is called Gårding inequality. So using (4.7) and (4.12), it is a standard result that the weak problem (4.5) has a unique solution, see [19, Theorem 6.6] and [52, Theorem 8.19].

4.1.1 Time Discretization

Let us recall that we want to solve (4.5) using time stepping schemes which avoid implicit convolutions when we dicretize using hybrid Fourier-finite elements. This means that the term $\nabla(\eta v)\cdot\nabla w$ in (4.6) should be handled explicitely in time. We propose two time stepping schemes with that property, but first let us recall that for sufficiently smooth functions in time we have that

$$v^{n+1} = v^n + \mathcal{O}(\Delta t), \quad \text{and} \quad v^{n+1} = 2v^n - v^{n-1} + \mathcal{O}(\Delta t^2), \tag{4.13}$$

so introducing the notation

$$\delta v^{n+1} = v^{n+1} - v^n, \quad \text{and} \quad \delta^2 v^{n+1} = v^{n+1} - 2v^n + v^{n-1}, \tag{4.14}$$

we have

$$\delta v^{n+1} = \mathcal{O}(\Delta t), \quad \text{and} \quad \delta^2 v^{n+1} = \mathcal{O}(\Delta t^2). \tag{4.15}$$

We first propose a time stepping scheme for (4.5) which uses a Backward Difference Method (BDF) approximation of order one for the time derivative, and a first order extrapolation in time,

$$\frac{1}{\Delta t}\int_\Omega \delta v^{n+1} w + \int_\Omega \overline{\eta}\nabla\delta v^{n+1}\cdot\nabla w + \int_\Omega \nabla\left(\eta v^n\right)\cdot\nabla w = \int_\Omega f^{n+1} w, \tag{4.16}$$

where $\overline{\eta}$ is a parameter function independent of time. The term $\int_\Omega \overline{\eta}\nabla\delta v^{n+1}\cdot\nabla w$ adds artificial diffusion, and is of first order in time accurate due to (4.15). In the same spirit, we also propose a time stepping scheme which uses a BDF approximation of order two for the time derivative, and a second order extrapolation in time,

$$\begin{aligned}\frac{1}{2\Delta t}\int_\Omega (3v^{n+1} - 4v^n + v^{n-1})w + \int_\Omega \overline{\eta}\nabla\delta^2 v^{n+1}\cdot\nabla w \\ + \int_\Omega \nabla\left(\eta(2v^n - v^{n-1})\right)\cdot\nabla w = \int_\Omega f^{n+1} w.\end{aligned} \tag{4.17}$$

Similarly observe that the term $\int_\Omega \overline{\eta}\nabla\delta^2 v^{n+1}\cdot\nabla w$ adds artificial diffusion, and is of second order in time accurate due to (4.15). We refer to schemes (4.16) and (4.17) as BDF1* and BDF2*, respectively. As proved later the parameter function $\overline{\eta}$ needs to be in the space $L^\infty(\Omega)$ and satisfy

$$\eta(x) \le \overline{\eta}(x) \quad \forall x \in \Omega, \tag{4.18}$$

to guarantee stability of both schemes for sufficiently small time steps Δt. Moreover, $\overline{\eta}$ can be a constant function, so schemes (4.16) and (4.17) avoid implicit convolutions when hybrid Fourier-finite elements are used. In Shen and Yang [60], the authors use similar ideas of using time extrapolations, parameter constants and artificial diffusion to discretize the Allen-Cahn and Cahn-Hilliard equations. Doing so they gain stability, and avoid solving a nonlinear problem at each time step. Moreover, the authors give a rigorous proof of stability and convergence of their methods. Similarly, in Dong and Shen [16] a scheme is proposed to solve two-phase incompressible flows; however, only numerical experiments are presented. In Cappanera [11] a first order in time scheme is proposed to solve multiphase fluid flows, and a formal proof of its stability is given.

4.1.2 Proof of Stability

We now focus in proving the stability of schemes (4.16) and (4.17). We use energy methods for these tasks, and take inspiration from the works of Becker [5] and Emmrich [18]; where both prove stability of an implicit BDF2 scheme for parabolic PDEs with variable time steps. See also Samarskii [58] and Thomée [64] for an overview of energy methods.

First of all to avoid irrelevant technicalities we assume that $f = 0$, and we define the operator $\delta^{k+1} v^n$ for general k as

$$\delta^{k+1} v^n := \delta(\delta^k) v^n = \delta^k v^n - \delta^k v^{n-1}, \tag{4.19}$$

which properties are summarized in the following proposition.

Proposition 4.1.1. *Let $a(\cdot,\cdot)$ be a bilinear form, then*

a) $2a(\delta^{k+1}v^{n+1}, \delta^k v^{n+1}) = \delta a(\delta^k v^{n+1}, \delta^k v^{n+1}) + a(\delta^{k+1}v^{n+1}, \delta^{k+1}v^{n+1})$
$+ a(\delta^k v^{n+1}, \delta^k v^n) - a(\delta^k v^n, \delta^k v^{n+1}).$

b) $2a(\delta^k v^{n+1}, \delta^{k+1}v^{n+1}) = \delta a(\delta^k v^{n+1}, \delta^k v^{n+1}) + a(\delta^{k+1}v^{n+1}, \delta^{k+1}v^{n+1})$
$- a(\delta^k v^{n+1}, \delta^k v^n) + a(\delta^k v^n, \delta^k v^{n+1}).$

c) $2a(\delta^{k+1}v^{n+1}, \delta^k v^n) = \delta a(\delta^k v^{n+1}, \delta^k v^{n+1}) - a(\delta^{k+1}v^{n+1}, \delta^{k+1}v^{n+1})$
$+ a(\delta^k v^{n+1}, \delta^k v^n) - a(\delta^k v^n, \delta^k v^{n+1}).$

d) $2a(\delta^{k+2}v^{n+1}, \delta^k v^{n+1}) = \delta^2 a(\delta^k v^{n+1}, \delta^k v^{n+1}) + a(\delta^{k+2}v^{n+1}, \delta^{k+2}v^{n+1})$
$- 2a(\delta^{k+1}v^n, \delta^{k+1}v^n) + a(\delta^{k+1}v^{n+1}, \delta^{k+1}v^n)$
$- a(\delta^{k+1}v^n, \delta^{k+1}v^{n+1}) + a(\delta^k v^{n+1}, \delta^k v^n)$
$- a(\delta^k v^n, \delta^k v^{n+1}) - a(\delta^k v^n, \delta^k v^{n-1})$
$+ a(\delta^k v^{n-1}, \delta^k v^n).$

Proof. We proof all items for $k = 0$. Their result for general k follows by induction and using the recursive property (4.19)

a) $2a(\delta v^{n+1}, v^{n+1}) = 2a(v^{n+1}, v^{n+1}) - 2a(v^n, v^{n+1}),$

$$= a(v^{n+1}, v^{n+1}) - a(v^n, v^n) + a(v^n, v^n) + a(v^{n+1}, v^{n+1})$$
$$- 2a(v^n, v^{n+1})$$
$$= \delta a(v^{n+1}, v^{n+1}) + a(v^n, v^n) + a(v^{n+1}, v^{n+1})$$
$$- 2a(v^n, v^{n+1})$$
$$= \delta a(v^{n+1}, v^{n+1}) + a(v^n, v^n) - a(v^n, v^{n+1}) + a(v^{n+1}, v^{n+1})$$
$$- a(v^n, v^{n+1})$$
$$= \delta a(v^{n+1}, v^{n+1}) - a(v^n, \delta v^{n+1}) + a(\delta v^{n+1}, v^{n+1})$$
$$= \delta a(v^{n+1}, v^{n+1}) + a(\delta v^{n+1}, \delta v^{n+1}) - a(v^{n+1}, \delta v^{n+1})$$
$$+ a(\delta v^{n+1}, v^{n+1})$$
$$= \delta a(v^{n+1}, v^{n+1}) + a(\delta v^{n+1}, \delta v^{n+1}) + a(v^{n+1}, v^n)$$
$$- a(v^n, v^{n+1}).$$

b) $2a(v^{n+1}, \delta v^{n+1}) = 2a(v^{n+1}, v^{n+1}) - 2a(v^{n+1}, v^n),$

$$
\begin{aligned}
&= a(v^{n+1}, v^{n+1}) - a(v^n, v^n) + a(v^n, v^n) + a(v^{n+1}, v^{n+1}) \\
&\quad - 2a(v^{n+1}, v^n) \\
&= \delta a(v^{n+1}, v^{n+1}) + a(v^n, v^n) + a(v^{n+1}, v^{n+1}) \\
&\quad - 2a(v^{n+1}, v^n) \\
&= \delta a(v^{n+1}, v^{n+1}) + a(v^n, v^n) - a(v^{n+1}, v^n) - a(v^{n+1}, v^n) \\
&\quad + a(v^{n+1}, v^{n+1}) \\
&= \delta a(v^{n+1}, v^{n+1}) - a(\delta v^{n+1}, v^n) + a(v^{n+1}, \delta v^{n+1}) \\
&= \delta a(v^{n+1}, v^{n+1}) + a(\delta v^{n+1}, \delta v^{n+1}) - a(\delta v^{n+1}, v^{n+1}) \\
&\quad + a(v^{n+1}, \delta v^{n+1}) \\
&= \delta a(v^{n+1}, v^{n+1}) + a(\delta v^{n+1}, \delta v^{n+1}) + a(v^n, v^{n+1}) \\
&\quad - a(v^{n+1}, v^n).
\end{aligned}
$$

c) $2a(\delta v^{n+1}, v^n) = -2a(\delta v^{n+1}, \delta v^{n+1}) + 2a(\delta v^{n+1}, v^{n+1}),$

and the result follows using item $a)$ with $k = 0$.

d) $2a(\delta^2 v^{n+1}, v^{n+1}) = 2a(\delta^2 v^{n+1}, \delta v^{n+1}) + 2a(\delta^2 v^{n+1}, v^n)$

$$= I + II.$$

Using item $a)$ with $k = 1$ for I we get

$$I = \delta a(\delta v^{n+1}, \delta v^{n+1}) + a(\delta^2 v^{n+1}, \delta^2 v^{n+1}) + a(\delta v^{n+1}, \delta v^n) - a(\delta v^n, \delta v^{n+1}),$$

and by definition

$$II = 2a(\delta v^{n+1}, v^n) - 2a(\delta v^n, v^n),$$

but using items $c)$ and $a)$ with $k = 0$ we have

$$
\begin{aligned}
II &= \big(\delta a(v^{n+1}, v^{n+1}) - a(\delta v^{n+1}, \delta v^{n+1}) + a(v^{n+1}, v^n) - a(v^n, v^{n+1})\big) \\
&\quad - \big(\delta a(v^n, v^n) + a(\delta v^n, \delta v^n) + a(v^n, v^{n-1}) - a(v^{n-1}, v^n)\big) \\
&= \delta^2 a(v^{n+1}, v^{n+1}) - a(\delta v^{n+1}, \delta v^{n+1}) - a(\delta v^n, \delta v^n) + a(v^{n+1}, v^n) \\
&\quad - a(v^n, v^{n+1}) - a(v^n, v^{n-1}) + a(v^{n-1}, v^n),
\end{aligned}
$$

thus

$$
\begin{aligned}
I + II &= \delta^2 a(v^{n+1}, v^{n+1}) + a(\delta^2 v^{n+1}, \delta^2 v^{n+1}) - 2a(\delta v^n, \delta v^n) \\
&\quad + a(\delta v^{n+1}, \delta v^n) - a(\delta v^n, \delta v^{n+1}) + a(v^{n+1}, v^n) \\
&\quad - a(v^n, v^{n+1}) - a(v^n, v^{n-1}) + a(v^{n-1}, v^n).
\end{aligned}
$$

□

We now prove the stability of BDF1* time scheme (4.16). Then we do the same for the BDF2* scheme (4.17) in Theorem 4.1.2.

Theorem 4.1.1 (BDF1*)**.** *Let $\overline{\eta} \in L^\infty(\Omega)$ such that condition* (4.18) *is satisfied, and let*

$$
\Delta t < \alpha^2 \eta_0 \|\nabla \eta\|^{-2}_{L^\infty(\Omega)}, \tag{4.20}
$$

where

$$
\alpha = \inf_{\Omega} \frac{\eta}{\overline{\eta}},
$$

then the solution of the scheme (4.16) satisfies,

$$
\begin{aligned}
&\frac{1}{\Delta t} \int_\Omega \eta |v^{n+1}|^2 + \int_\Omega \left(\frac{\overline{\eta}}{\eta} - 1\right) |\nabla(\eta v^{n+1})|^2 \\
&\qquad \leq \frac{1}{\Delta t} \int_\Omega \eta |v^0|^2 + \int_\Omega \left(\frac{\overline{\eta}}{\eta} - 1\right) |\nabla(\eta v^0)|^2.
\end{aligned} \tag{4.21}
$$

Proof. Summing and substracting $\nabla(\eta v^{n+1})$ in equation (4.16) we get,

$$\frac{1}{\Delta t}\int_\Omega \delta v^{n+1} w + \int_\Omega \overline{\eta}\nabla\delta v^{n+1}\cdot\nabla w \\ - \int_\Omega \nabla\left(\eta\delta v^{n+1}\right)\cdot\nabla w + \int_\Omega \nabla\left(\eta v^{n+1}\right)\cdot\nabla w = 0.$$

Choosing $w = 2\eta v^{n+1}$, we have

$$\frac{2}{\Delta t}\int_\Omega \eta\delta v^{n+1} v^{n+1} + 2\int_\Omega \overline{\eta}\nabla\delta v^{n+1}\cdot\nabla\left(\eta v^{n+1}\right) \\ - 2\int_\Omega \nabla\left(\eta\delta v^{n+1}\right)\cdot\nabla\left(\eta v^{n+1}\right) + 2\int_\Omega |\nabla(\eta v^{n+1})|^2 = 0. \quad (4.22)$$

Observe that,

$$\begin{aligned}\nabla\delta v^{n+1} &= \nabla(\frac{\eta}{\eta}\delta v^{n+1}) \\ &= \frac{1}{\eta}\nabla\delta(\eta v^{n+1}) + \delta(\eta v^{n+1})\nabla\left(\frac{1}{\eta}\right) \\ &= \frac{1}{\eta}\nabla\delta(\eta v^{n+1}) - \delta(\eta v^{n+1})\left(\frac{\nabla\eta}{\eta^2}\right) \\ &= \frac{1}{\eta}\nabla\delta(\eta v^{n+1}) - \frac{1}{\eta}\delta v^{n+1}\nabla\eta. \end{aligned} \quad (4.23)$$

Using (4.23) in the second term of (4.22) we get,

$$\frac{2}{\Delta t}\int_\Omega \eta\delta v^{n+1} v^{n+1} + 2\int_\Omega \frac{\overline{\eta}}{\eta}\nabla\delta(\eta v^{n+1})\cdot\nabla\left(\eta v^{n+1}\right) \\ - 2\int_\Omega \frac{\overline{\eta}}{\eta}\delta v^{n+1}\nabla\eta\cdot\nabla\left(\eta v^{n+1}\right) \\ - 2\int_\Omega \nabla\left(\eta\delta v^{n+1}\right)\cdot\nabla\left(\eta v^{n+1}\right) + 2\int_\Omega |\nabla(\eta v^{n+1})|^2 = 0.$$

We now apply proposition 4.1.1.a to the first, second, and fourth terms of the left

hand side in this last equation,

$$\frac{1}{\Delta t}\int_\Omega \eta(\delta|v^{n+1}|^2+|\delta v^{n+1}|^2)+\int_\Omega \frac{\overline{\eta}}{\eta}(\delta|\nabla(\eta v^{n+1})|^2 \\ +|\nabla(\eta\delta v^{n+1})|^2)-2\int_\Omega \frac{\overline{\eta}}{\eta}\delta v^{n+1}\nabla\eta\cdot\nabla\left(\eta v^{n+1}\right)+\int_\Omega\left|\nabla\left(\eta v^{n+1}\right)\right|^2+\int_\Omega|\nabla\left(\eta v^n\right)|^2 \\ -\int_\Omega\left|\nabla\left(\eta\delta v^{n+1}\right)\right|^2=0.$$

Using $-2\int_\Omega \frac{\overline{\eta}}{\eta}\delta v^{n+1}\nabla\eta\cdot\nabla\left(\eta v^{n+1}\right)\geq -2\int_\Omega \frac{\overline{\eta}}{\eta}\left|\delta v^{n+1}\nabla\eta\cdot\nabla\left(\eta v^{n+1}\right)\right|$ and Cauchy's inequality (4.9) to the term $|\delta v^{n+1}\nabla\eta\cdot\nabla\left(\eta v^{n+1}\right)|$, we get the following

$$\frac{1}{\Delta t}\int_\Omega \eta(\delta|v^{n+1}|^2+|\delta v^{n+1}|^2)+\int_\Omega \frac{\overline{\eta}}{\eta}(\delta|\nabla(\eta v^{n+1})|^2+|\nabla(\eta\delta v^{n+1})|^2) \\ -\int_\Omega \frac{\overline{\eta}}{\eta}\left(\frac{1}{\epsilon}|\delta v^{n+1}\nabla\eta|^2+\epsilon|\nabla(\eta v^{n+1})|^2\right)+\int_\Omega\left|\nabla\left(\eta v^{n+1}\right)\right|^2 \\ +\int_\Omega|\nabla\left(\eta v^n\right)|^2-\int_\Omega\left|\nabla\left(\eta\delta v^{n+1}\right)\right|^2\leq 0.$$

Bounding the term $-\int_\Omega \frac{\overline{\eta}}{\eta}\frac{1}{\epsilon}|\delta v^{n+1}\nabla\eta|^2$ and regrouping we get,

$$\frac{1}{\Delta t}\int_\Omega \eta|v^{n+1}|^2+\int_\Omega\left(\frac{\eta}{\Delta t}-\frac{\overline{\eta}}{\eta\epsilon}||\nabla\eta||^2_{L^\infty(\Omega)}\right)|\delta v^{n+1}|^2 \\ +\int_\Omega \frac{\overline{\eta}}{\eta}(1-\epsilon)|\nabla(\eta v^{n+1})|^2+\int_\Omega\left(\frac{\overline{\eta}}{\eta}-1\right)|\nabla(\eta\delta v^{n+1})|^2 \\ \leq\frac{1}{\Delta t}\int_\Omega \eta|v^n|^2+\int_\Omega\left(\frac{\overline{\eta}}{\eta}-1\right)|\nabla(\eta v^n)|^2$$

Observe that $\left(\frac{\overline{\eta}}{\eta}-1\right)\geq 0$, because $\overline{\eta}\geq\eta$ by assumption. Then the third term is positive and can be dropped. Moreover, using $\epsilon=\frac{\eta}{\overline{\eta}}$ and condition (4.20), the second term becomes positive, so dropping it we finally obtain

$$\frac{1}{\Delta t}\int_\Omega \eta|v^{n+1}|^2+\int_\Omega\left(\frac{\overline{\eta}}{\eta}-1\right)|\nabla(\eta v^{n+1})|^2\leq\frac{1}{\Delta t}\int_\Omega \eta|v^n|^2+\int_\Omega\left(\frac{\overline{\eta}}{\eta}-1\right)|\nabla(\eta v^n)|^2.$$

Applying this last inequality recursively we get (4.21).

□

Theorem 4.1.2 (BDF2*)**.** *Let $\overline{\eta} \in L^\infty(\Omega)$ such that condition* (4.18) *is satisfied, and let*

$$\Delta t < \frac{\alpha^2 \eta_0}{2} \|\nabla \eta\|^{-2}_{L^\infty(\Omega)}, \tag{4.24}$$

where

$$\alpha = \inf_\Omega \frac{\eta}{\overline{\eta}},$$

then the solution of the scheme (4.17) satisfies,

$$\begin{aligned} \frac{1}{2\Delta t}\int_\Omega \eta|\delta v^{n+1}|^2 + \int_\Omega \left(\frac{\overline{\eta}}{\eta} - 1\right)|\nabla(\eta \delta v^{n+1})|^2 + \int_\Omega \left|\nabla\left(\eta v^{n+1}\right)\right|^2 \\ \leq \frac{1}{2\Delta t}\int_\Omega \eta|\delta v^{1}|^2 + \int_\Omega \left(\frac{\overline{\eta}}{\eta} - 1\right)|\nabla(\eta \delta v^{1})|^2 + \int_\Omega \left|\nabla\left(\eta v^{1}\right)\right|^2. \end{aligned} \tag{4.25}$$

Proof. Observe first that $(3v^{n+1} - 4v^n + v^{n-1})/2 = \delta v^{n+1} + \frac{1}{2}\delta^2 v^{n+1}$. Moreover, summing and substracting $\nabla(\eta v^{n+1})$ in equation (4.17) we get

$$\begin{aligned} \frac{1}{\Delta t}\int_\Omega \delta v^{n+1} w + \frac{1}{2\Delta t}\int_\Omega \delta^2 v^{n+1} w + \int_\Omega \overline{\eta}\nabla\delta^2 v^{n+1}\cdot\nabla w \\ - \int_\Omega \nabla\left(\eta\delta^2 v^{n+1}\right)\cdot\nabla w + \int_\Omega \nabla\left(\eta v^{n+1}\right)\cdot\nabla w = 0. \end{aligned}$$

Choosing $w = 2\eta\delta v^{n+1}$, we have

$$\begin{aligned} \frac{2}{\Delta t}\int_\Omega \eta|\delta v^{n+1}|^2 + \frac{2}{2\Delta t}\int_\Omega \eta\delta^2 v^{n+1}\delta v^{n+1} \\ + 2\int_\Omega \overline{\eta}\nabla\delta^2 v^{n+1}\cdot\nabla\left(\eta\delta v^{n+1}\right) - 2\int_\Omega \nabla\left(\eta\delta^2 v^{n+1}\right)\cdot\nabla\left(\eta\delta v^{n+1}\right) \\ + 2\int_\Omega \nabla\left(\eta v^{n+1}\right)\cdot\nabla\left(\eta\delta v^{n+1}\right) = 0. \end{aligned} \tag{4.26}$$

For the third term of (4.26) we apply equation (4.23), but replace δv^{n+1} with $\delta^2 v^{n+1}$ instead and get

$$\begin{aligned}
&\frac{2}{\Delta t}\int_\Omega \eta|\delta v^{n+1}|^2 + \frac{2}{2\Delta t}\int_\Omega \eta\delta^2 v^{n+1}\delta v^{n+1} \\
&\quad + 2\int_\Omega \frac{\overline{\eta}}{\eta}\nabla\delta^2(\eta v^{n+1})\cdot\nabla\left(\eta\delta v^{n+1}\right) - 2\int_\Omega \frac{\overline{\eta}}{\eta}\delta^2 v^{n+1}\nabla\eta\cdot\nabla\left(\eta\delta v^{n+1}\right) \\
&\quad - 2\int_\Omega \nabla\left(\eta\delta^2 v^{n+1}\right)\cdot\nabla\left(\eta\delta v^{n+1}\right) + 2\int_\Omega \nabla\left(\eta v^{n+1}\right)\cdot\nabla\left(\eta\delta v^{n+1}\right) = 0.
\end{aligned}$$

We now apply item a) of Proposition 4.1.1 to the second, third, fourth, fifth, and sixth terms of the left hand side

$$\begin{aligned}
&\frac{2}{\Delta t}\int_\Omega \eta|\delta v^{n+1}|^2 + \frac{1}{2\Delta t}\int_\Omega \eta(\delta|\delta v^{n+1}|^2 + |\delta^2 v^{n+1}|^2) \\
&\quad + \int_\Omega \frac{\overline{\eta}}{\eta}(\delta|\nabla(\eta\delta v^{n+1})|^2 + |\nabla(\eta\delta^2 v^{n+1})|^2) - 2\int_\Omega \frac{\overline{\eta}}{\eta}\delta^2 v^{n+1}\nabla\eta\cdot\nabla\left(\eta\delta v^{n+1}\right) \\
&\quad + \int_\Omega |\nabla(\eta\delta v^n)|^2 - \int_\Omega \left|\nabla\left(\eta\delta^2 v^{n+1}\right)\right|^2 + \int_\Omega \delta\left|\nabla\left(\eta v^{n+1}\right)\right|^2 = 0,
\end{aligned}$$

Using $-2\int_\Omega \frac{\overline{\eta}}{\eta}\delta^2 v^{n+1}\nabla\eta\cdot\nabla\left(\eta\delta v^{n+1}\right) \geq -2\int_\Omega \frac{\overline{\eta}}{\eta}\left|\delta^2 v^{n+1}\nabla\eta\cdot\nabla\left(\eta\delta v^{n+1}\right)\right|$ and Cauchy's inequality (4.9) with $\epsilon > 0$ to the term $|\delta^2 v^{n+1}\nabla\eta\cdot\nabla\left(\eta\delta v^{n+1}\right)|$, we get the following inequality

$$\begin{aligned}
&\frac{2}{\Delta t}\int_\Omega \eta|\delta v^{n+1}|^2 + \frac{1}{2\Delta t}\int_\Omega \eta(\delta|\delta v^{n+1}|^2 + |\delta^2 v^{n+1}|^2) \\
&\quad + \int_\Omega \frac{\overline{\eta}}{\eta}(\delta|\nabla(\eta\delta v^{n+1})|^2 + |\nabla(\eta\delta^2 v^{n+1})|^2) - \int_\Omega \frac{\overline{\eta}}{\eta}\left(\frac{1}{\epsilon}|\delta^2 v^{n+1}\nabla\eta|^2 + \epsilon|\nabla(\eta\delta v^{n+1})|^2\right) \\
&\quad + \int_\Omega |\nabla(\eta\delta v^n)|^2 - \int_\Omega \left|\nabla\left(\eta\delta^2 v^{n+1}\right)\right|^2 + \int_\Omega \delta\left|\nabla\left(\eta v^{n+1}\right)\right|^2 \leq 0.
\end{aligned}$$

Dropping $\frac{2}{\Delta t}\int_\Omega \eta|\delta v^{n+1}|^2$, bounding $-\int_\Omega \frac{\overline{\eta}}{\eta}\frac{1}{\epsilon}|\delta^2 v^{n+1}\nabla\eta|^2$, and regrouping we get

$$\begin{aligned}
&\frac{1}{2\Delta t}\int_\Omega \eta|\delta v^{n+1}|^2 + \int_\Omega\left(\frac{\eta}{2\Delta t} - \frac{\overline{\eta}}{\eta\epsilon}\left|\left|\nabla\eta\right|\right|^2_{L^\infty(\Omega)}\right)|\delta^2 v^{n+1}|^2 \\
&+ \int_\Omega \frac{\overline{\eta}}{\eta}(1-\epsilon)\left|\nabla(\eta\delta v^{n+1})\right|^2 + \int_\Omega\left(\frac{\overline{\eta}}{\eta}-1\right)\left|\nabla(\eta\delta^2 v^{n+1})\right|^2 + \int_\Omega\left|\nabla\left(\eta v^{n+1}\right)\right|^2 \\
&\leq \frac{1}{2\Delta t}\int_\Omega \eta|\delta v^{n}|^2 + \int_\Omega\left(\frac{\overline{\eta}}{\eta}-1\right)\left|\nabla(\eta\delta v^{n})\right|^2 + \int_\Omega\left|\nabla\left(\eta v^{n}\right)\right|^2.
\end{aligned}$$

Observe that $\left(\frac{\overline{\eta}}{\eta}-1\right)\geq 0$, because $\overline{\eta}\geq\eta$ by assumption, so we drop the fourth term. Moreover, using $\epsilon = \frac{\eta}{\overline{\eta}}$ and condition (4.24), the second term becomes positive, so dropping it we obtain finally

$$\begin{aligned}
&\frac{1}{2\Delta t}\int_\Omega \eta|\delta v^{n+1}|^2 + \int_\Omega\left(\frac{\overline{\eta}}{\eta}-1\right)\left|\nabla(\eta\delta v^{n+1})\right|^2 + \int_\Omega\left|\nabla\left(\eta v^{n+1}\right)\right|^2 \\
&\qquad\leq \frac{1}{2\Delta t}\int_\Omega \eta|\delta v^{n}|^2 + \int_\Omega\left(\frac{\overline{\eta}}{\eta}-1\right)\left|\nabla(\eta\delta v^{n})\right|^2 + \int_\Omega\left|\nabla\left(\eta v^{n}\right)\right|^2.
\end{aligned}$$

Then applying this last inequality recursively we get (4.25). □

Although conditions (4.20) and (4.24) in Theorems 4.1.1 and 4.1.2 are too restrictive, numerical evidence indicates that both schemes (4.16) and (4.17) are stable for time steps $\Delta t \sim O(h)$ using finite elements where h is the mesh size, and $\Delta t \sim O(h + M^{-1})$ using Fourier-finite elements where M is the number of complex Fourier modes. These claims are substantiated in the following numerical tests.

4.1.3 Numerical Experiments in $\mathbb{R}^2$

We present numerical computations for the simple model (3.25) using schemes (4.16) and (4.17) when $\Omega\subset\mathbb{R}^2$. Specifically, we set $\Omega = \{(x,y)\in\mathbb{R}^2 : r^2 = x^2+y^2 <$

1} and,

$$\eta(x,y) = \frac{1}{1-\beta\cdot s(r)\cos(\theta)},$$

where $s(r) = r^4(1-r)$ and β is a parameter to adjust the desired ratio $r_\eta = \frac{\eta_{max}}{\eta_{min}}$. To compute β, observe that the function $s(r)$ satisfies $s(r) \geq 0$ for $r \in \Omega$, and its maximum is at $r^* = \frac{4}{5}$ and is equal to $s_{\max} = s(r^*) \approx 0.082$. Then,

$$\eta_{\min} = \frac{1}{1+\beta\cdot s_{\max}}, \qquad \eta_{\max} = \frac{1}{1-\beta\cdot s_{\max}},$$
$$r_\eta = \frac{1+\beta\cdot s_{\max}}{1-\lambda\cdot s_{\max}}, \quad \text{and} \qquad \beta = \frac{1}{s_{\max}}\cdot\left(\frac{r_\eta - 1}{r_\eta + 1}\right).$$

Moreover, we set as an analytical solution of (4.3) the function

$$v(x,y,t) = \eta^{-1}\cos(x+y+t),$$

and compute f accordingly. We also choose,

$$\overline{\eta} = \sup_{(x,y)\in\Omega} \eta(x,y),$$

so the condition (4.18) is always satisfied. Table 4.1 shows time and space convergence of the schemes (4.16) and (4.17) which are referred as BDF1* and BDF2*, respectively. This table also shows the computed order of convergence (COC). To obtain those results, we discretized spatially using $\mathbb{P}_2$ Lagrange finite elements using an uniform mesh, and setting a difference ratio $r_\eta = 100$, so $\overline{\eta} = 100$. Successful convergence is always observed for both schemes.

(a) Time convergence rate at $T = 10$ and using $h = 2^{-6}$.

Δt	BDF1*		BDF2*	
	L_2 Rel. Error	COC	L_2 Rel. Error	COC
0.1	2.1169E-01	—	3.3748E-02	—
0.05	9.3644E-02	0.66	8.2462E-03	2.03
0.025	4.0056E-02	0.74	2.0522E-03	2.01
0.0125	1.8193E-02	0.80	5.1340E-04	2.00
0.00625	8.6826E-03	0.84	1.2906E-04	1.99
0.003125	4.2488E-03	0.87	3.2999E-05	1.97

(b) Space convergence rate at $T = 1$.

h	BDF1*		BDF2*	
	L_2 Rel. Error	COC	L_2 Rel. Error	COC
2^{-3}	7.9851E-03	—	8.0138E-03	—
2^{-4}	6.3200E-04	3.66	6.5462E-04	3.61
2^{-5}	6.7111E-05	3.24	4.4550E-05	3.88
2^{-6}	6.6356E-06	3.34	2.5694E-06	4.12

Table 4.1: Solving model (4.3) in $\mathbb{R}^2$ using FEM. $L^\infty([0,T], L^2(\Omega))$ errors for $r_\eta = 100$.

4.1.4 Numerical Experiments in $\mathbb{R}^3$

Let $\Omega \subset \mathbb{R}^3$ be an axisymmetric domain. Then using Fourier representation in the azimuthal direction as in (3.13), the BDF2* scheme (4.17) becomes

$$\begin{aligned}\frac{1}{2\Delta t}\int_{\hat{\Omega}}(3\hat{v}_k^{n+1}-4\hat{v}_k^n+\hat{v}_k^{n-1})\hat{\psi}rdrdz+\int_{\hat{\Omega}}\overline{\eta}\nabla_{rz}\delta^2\hat{v}_k^{n+1}\cdot\nabla_{rz}\hat{\psi}rdrdz\\ +\int_{\hat{\Omega}}\overline{\eta}\frac{k^2}{r}\delta^2\hat{v}_k^{n+1}\hat{\psi}drdz+\int_{\hat{\Omega}}\nabla_{rz}[(V^n)_k^{\wedge}]\cdot\nabla_{rz}\hat{\psi}rdrdz\\ +\int_{\hat{\Omega}}\frac{k^2}{r}(V^n)_k^{\wedge}\hat{\psi}drdz=\int_{\hat{\Omega}}\hat{f}_k^{n+1}\hat{\psi},\quad k=0,\pm1,...,\pm M,\end{aligned}\tag{4.27}$$

where $\hat{\Omega}$ is the meridional plane, and $\nabla_{rz}v = (\partial_r v)\mathbf{e}_r + (\partial_z v)\mathbf{e}_z$ and $(V^n)_k^{\wedge} = (\eta(2v^n - v^{n-1}))_k^{\wedge}$. Recall the function $\overline{\eta}$ is a parameter function which needs to satisfy (4.18), but also we it set as

$$\overline{\eta} = \overline{\eta}(r, z). \tag{4.28}$$

This requirement makes sense if we want to avoid convolutions involving $\hat{v}_k^{n+1}$. The term $(V^n)_k^{\wedge} = (\eta(2v^n - v^{n-1}))_k^{\wedge}$ in (4.27) couples the Fourier modes, but it is handled explicitly in time, so the system matrices are still decoupled mode by mode when finite elements are used. To compute $(V^n)_k^{\wedge}$ we use forward and backward Fast Fourier Transform (FFT), i.e., we apply the inverse FFT to $\hat{v}^n$ and $\hat{v}^{n-1}$, compute the subtraction $2v^n - v^{n-1}$, then compute its product against η, and finally apply FFT to this product.

We now investigate the stability of scheme (4.27) setting $\Omega = \{(r, \theta, z) \in [0, 1] \times [0, 2\pi] \times [-1/2, 1/2]\}$, and $v(r, \theta, z, t) = (z + r^2 \sin(\theta)) \cos(t)$ as an analytical solution. We also set

$$\eta = 1 + r^2 \tilde{g}_M(\theta),$$

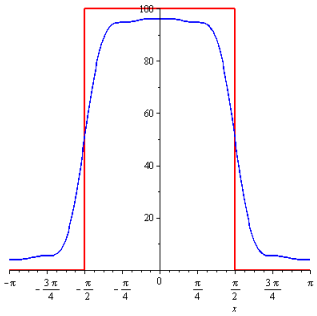

Figure 4.1: Functions $g(\theta)$ and $\tilde{g}_8(\theta)$.

where $\tilde{g}_M(\theta)$ approximates

$$g(\theta) = \begin{cases} 100 & \text{if} \quad \theta \in [-\frac{\pi}{2}, \frac{\pi}{2}], \\ 1 & \text{if} \quad \theta \in [-\pi, -\frac{\pi}{2}) \cup (\frac{\pi}{2}, \pi), \end{cases}$$

using M-complex modes and the so-called Cesáro filter, see [34]. In this experiment we set $M = 8$, and figure 4.1 shows $g(\theta)$ and $\tilde{g}_8(\theta)$. Observe that the difference ratio $r_\eta \approx 100$, so we set $\overline{\eta} = 100$. Observe $\overline{\eta}$ is not dependent on θ as requested in (4.28). To discretize the meridional domain $\hat{\Omega}$, we use $\mathbb{P}_2$ Lagrange elements. Table 4.2 shows the successful convergence rate in time of scheme (4.27) for different time steps Δt, and a uniform mesh of size $h = 0.0125$.

(a) Convergence rate for $h = 0.0125$ and $T = 10$.

Δt	BDF2*	
	L_2 Rel. Error	COC
1.000000	1.4127E-01	—
0.100000	3.8682E-02	1.87
0.050000	5.3183E-03	2.86
0.025000	1.4634E-03	1.86
0.012500	2.4175E-04	2.60
0.006250	6.0064E-05	2.01
0.003125	1.4922E-05	2.01
0.001563	3.7474E-06	1.99

Table 4.2: Solving model (4.3) in $\mathbb{R}^3$ using Fourier-FEM. $L^\infty([0,T], L^2(\Omega))$ errors for $M = 8$ modes and $r_\eta \approx 100$.

4.2 General Scalar Parabolic PDEs

We now focus our attention to the following initial-boundary value problem

$$\begin{cases} u_t + A(t)u = f(\mathbf{x}, t) & \mathbf{x} \in \Omega, 0 < t \leq T, \\ u(\mathbf{x}, t) = 0 & \mathbf{x} \in \partial\Omega, 0 < t \leq T, \\ u(\mathbf{x}, 0) = u^0 & \mathbf{x} \in \Omega, \end{cases} \tag{4.29}$$

where we assume $\Omega \subset \mathbb{R}^d$ for $d = 2, 3$ with smooth boundary $\partial\Omega$, and

$$A(t)u = -\sum_{ij}^{d} \frac{\partial}{\partial x_j} \left(\eta_{ij}(\mathbf{x}, t) \frac{\partial u}{\partial x_j} \right) + \sum_{i}^{d} \eta_i(\mathbf{x}, t) \frac{\partial u}{\partial x_i} + \eta(\mathbf{x}, t)u. \tag{4.30}$$

We also assume that η_{ij}, η_i, and η are uniformly bounded with minimal regularity; specifically, we assume $\eta_{ij}, \eta_i, \eta \in L^\infty([0,T], L^\infty(\Omega))$. By assumption each η_{ij} is uniformly positive and there exists a constant $c_\eta > 0$ such that $\sum_{ij}^d \eta_{ij}\xi_i\xi_j \geq c_\eta|\xi|^2$ for $\xi \in \mathbb{R}^d$.

Recall that our goal is to solve numerically (4.29), but let us first investigate the well posedness of model (4.29). For instance, defining

$$a(t;u,v) = \sum_{i,j}^{d} \int_\Omega \eta_{ij} \frac{\partial u}{\partial x_i} \frac{\partial v}{\partial x_j} dx, \tag{4.31}$$

$$\text{and} \quad b(t;u,v) = \sum_{i}^{d} \int_\Omega \eta_i \frac{\partial u}{\partial x_i} v dx + \int_\Omega \eta u v dx, \tag{4.32}$$

we get the variational weak form of (4.29) which consists of finding $u \in C([0,T]; H_0^1(\Omega))$, with $\partial_t u \in L^2([0,T]; H^{-1}(\Omega))$ such that

$$\begin{cases} (u_t, v) + a(t;u,v) + b(t;u,v) = (f,v), \quad \forall v \in H_0^1(\Omega), 0 < t \leq T, \\ u(0) = u^0 \end{cases} \tag{4.33}$$

where $u^0 \in H_0^1(\Omega)$, and $f : [0,T] \to L^2(\Omega)$. To simplify notation let us define $|u| := \|u\|_{H^1(\Omega)}$ for $u \in H_0^1(\Omega)$, and $\|u\| := \|u\|_{L^2(\Omega)}$ for $u \in L^2(\Omega)$. We also define $\|u\|_{L^\infty} := \|u\|_{L^\infty([0,T],L^\infty(\Omega))}$ for $u \in L^\infty([0,T], L^\infty(\Omega))$. Observe that $a(t;v,u)$ and $b(t;v,u)$ are bilinear forms; where $a(t;\cdot,\cdot)$ is symmetric and both forms satisfy the

following properties:

$$c|u|^2 \leq a(t;u,u), \tag{4.34}$$

$$\widehat{c}|u|^2 - \lambda\|u\|^2 \leq a(t;u,u) + b(t;u,u), \tag{4.35}$$

$$|a(t;u,v)| + |a'(t;u,v)| + |b(t;u,v)| + |b'(t;u,v)| \leq C|u||v|, \tag{4.36}$$

$$|b(t;v,u) - b(t;u,v)| \leq \widehat{C}(|u|\|v\| + |v|\|u\|). \tag{4.37}$$

where $a'(t,\cdot,\cdot) = (d/dt)a(t,\cdot,\cdot)$, and $c, \widehat{c}, C, \widehat{C} \in \mathbb{R}^+$. For instance the coercivity property (4.34) is satisfied with $c = c_\eta$. Now, notice that

$$\begin{aligned} a(t;u,u) + b(t;u,u) &= \sum_{ij}^{d} \int_\Omega \eta_{ij} \frac{\partial u}{\partial x_i}\frac{\partial u}{\partial x_j} + \sum_{i}^{d} \int_\Omega \eta_i \frac{\partial u}{\partial x_i} u dx + \int_\Omega \eta u^2 dx \\ &\geq c_\eta \int_\Omega |\nabla u|^2 - \sum_{i}^{d} \|\eta_i\|_{L^\infty} \int_\Omega |\nabla u||u| dx \\ &\quad - \|\eta\|_{L^\infty} \int_\Omega u^2 dx, \end{aligned} \tag{4.38}$$

but using Cauchy's inequality (4.9) with $\epsilon = \frac{c_\eta}{2}\left(\sum_i^d \|\eta_i\|_{L^\infty}\right)^{-1}$, we get

$$\sum_{i}^{d} \|\eta_i\|_{L^\infty} \int_\Omega |\nabla u||u| dx \leq \frac{c_\eta}{2} \int_\Omega |\nabla u|^2 + \frac{1}{2c_\eta}\left(\sum_{i}^{d} \|\eta_i\|_{L^\infty}\right)^2 \int_\Omega u^2, \tag{4.39}$$

so using this last inequality in (4.38), property (4.35) is satisfied with $\widehat{c} = \frac{c_\eta}{2}$, and $\lambda = \frac{1}{2c_\eta}\left(\sum_i^d \|\eta_i\|_{L^\infty}\right)^2 + \|\eta\|_{L^\infty}$. We assume that coefficients η_{ij}, η_i, and η are sufficiently smooth in time to satisfy (4.36). Observe that property (4.37) is satisfied for $\widehat{C} = 2\sum_i^d \|\eta_i\|_{L^\infty}$. Now, using a similar reasoning as in (4.38) and (4.39), we see that for

any constants $\epsilon_1, \epsilon_2 > 0$ we have that

$$\epsilon_2 |b(t;u,u)| \leq \frac{c\epsilon_1}{2}|u|^2 + \sigma \|u\|^2, \tag{4.40}$$

where $\sigma = \frac{1}{2c\epsilon_1}\epsilon_2^2 \left(\sum_i^d \|\eta_i\|_{L^\infty}\right)^2 + \epsilon_2 \|\eta\|_{L^\infty}$. Inequality (4.40) is useful to prove stability in subsection 4.2.2. Finally, if we define $A(t;u,v) = a(t;u,v) + b(t;u,v)$, then $A(t;\cdot,\cdot)$ is bounded in $H_0^1(\Omega)$ and satisfies Gårding inequality; namely,

$$\widehat{c}|u|^2 \leq A(t;u,u) + \lambda \|u\|^2,$$

so it is a standard result that the weak problem (4.33) has a unique solution, see [19, Theorem 6.6], and [52, Theorem 8.19].

4.2.1 Time Discretization

Let us recall that we are looking to solve (4.33) using a time stepping scheme which uses constant matrices at every time step, and avoids implicit convolutions when hybrid Fourier-finite elements are employed. So both terms $a(t;u,v)$ and $b(t;u,v)$ should be handled explicitely in time. We now propose a second order time scheme with those properties,

$$\begin{aligned} &\frac{1}{\Delta t}(\delta u^{n+1} + \frac{1}{2}\delta^2 u^{n+1}, v) + \overline{a}(\delta^2 u^{n+1}, v) \\ &\quad + a(t^{n+1}; 2u^n - u^{n-1}, v) + b(t^{n+1}; 2u^n - u^{n-1}, v) = (f^{n+1}, v) \end{aligned} \tag{4.41}$$

where $\overline{a}(\cdot,\cdot)$ is a symmetric bilinear which needs to satisfy the following conditions $\forall u, v \in H_0^1(\Omega)$ and $\forall t \in (0,T]$:

$$l_{\overline{a}}|u|^2 \leq \overline{a}(u,u), \tag{4.42}$$

$$\overline{a}(u,v) \leq L_{\overline{a}}|u||v|, \tag{4.43}$$

$$a(t,u,u) \leq \overline{a}(u,u), \tag{4.44}$$

where $l_{\overline{a}}$ and $L_{\overline{a}}$ are positive constants. The necessity of condition (4.44) is used in the proof of Theorem (4.2.1). For instance, we can choose,

$$\overline{a}(u,v) = d\overline{\eta}\int_\Omega \sum_i^d \frac{\partial u}{\partial x_i}\frac{\partial v}{\partial x_i}dx, \tag{4.45}$$

where $\overline{\eta} = \sup_{1\leq i,j\leq d,\Omega\times[0,T]} \eta_{ij}$. Doing so conditions (4.42)-(4.44) are satisfied, and we avoid implicit convolutions using time independent matrices even when the operator $A(t)$ is time dependent. Moreover, observe that the term $\overline{a}(\delta^2 u^{n+1}, v)$ in (4.41) adds artificial diffusion in the same spirit as (4.17). Scheme (4.41) we will be refered as BDF2** from now on, and its stability is proved next.

4.2.2 Proof of Stability

In order to prove the stability of scheme (4.41), we shall need the following discrete version of Gronwall's lemma which proof can be found in [56].

Lemma 4.2.1. *Assume that the sequence* $\{w_n\}$ *satisfies*

$$w_n \leq a_n + \sum_{k=0}^{n-1} b_k w_k, \quad n = 0, 1, \ldots,$$

where $\{a_n\}$ *is nondecreasing and* $b_n \geq 0$. *then we have the following bound:*

$$w_n \leq a_n exp\left(\sum_{k=0}^{n-1} b_k\right).$$

Theorem 4.2.1 (BDF2**). *Let* $\overline{a}(\cdot,\cdot) : H_0^1(\Omega)\times H_0^1(\Omega) \to \mathbb{R}$, *be a symmetric bilinear form such that satisfies* (4.42)-(4.44), *and let*

$$\Delta t < \frac{c}{2\big(8\widehat{C}^2(1+\varrho)^2+\Lambda\big)}, \tag{4.46}$$

where

$$\Lambda = \frac{1}{16}(2+\varrho)^2\big(\sum_{i}^{d}\|\eta_i\|_{L^\infty}\big)^2 + (2+\varrho)c\|\eta\|_{L^\infty},$$

and $\varrho = \frac{L_{\overline{a}}}{c}$. *Then the solution of the scheme* (4.41) *satisfies,*

$$\begin{aligned}\|\delta u^{n+1}\|^2 + \|u^{n+1}\|^2 + \Delta t|\delta u^{n+1}|^2 + \Delta t|u^{n+1}|^2 \\ \leq C\left(\|\delta u^1\|^2 + \|u^1\|^2 + \Delta t|\delta u^1|^2 + \Delta t|u^1|^2 + \Delta t|u^0|^2\right) \quad \forall t_{n+1} \leq T,\end{aligned}$$

where the constant C *depends on* $l_{\overline{a}}, \varrho$, T, *and the constants that appear in properties (4.34)-(4.37).*

Proof. We first sum and subtract the terms $a(t^{n+1}, u^{n+1}, v)$, and $b(t^{n+1}, u^{n+1}, v)$ in equation (4.41) to get

$$\begin{aligned}\frac{1}{\Delta t}(\delta u^{n+1} + \frac{1}{2}\delta^2 u^{n+1}, v) + \overline{a}(\delta^2 u^{n+1}, v) - a(t^{n+1}; \delta^2 u^{n+1}, v) + a(t^{n+1}; u^{n+1}, v) \\ - b(t^{n+1}; \delta^2 u^{n+1}, v) + b(t^{n+1}; u^{n+1}, v) = 0.\end{aligned}$$

Choosing $v = \Delta t \varrho \delta u^{n+1} + 2\Delta t u^{n+1}$ we obtain

$$I_1 + \Delta t \cdot (I_2 + I_3 + I_4 + I_5 + I_6) = 0, \tag{4.47}$$

where

$$I_1 = 2(\delta u^{n+1} + \frac{1}{2}\delta^2 u^{n+1}, \varrho \delta u^{n+1} + u^{n+1}), \qquad I_2 = 2\overline{a}(\delta^2 u^{n+1}, \varrho \delta u^{n+1} + u^{n+1}),$$
$$I_3 = -2a(t^{n+1}; \delta^2 u^{n+1}, \varrho \delta u^{n+1} + u^{n+1}), \qquad I_4 = 2a(t^{n+1}; u^{n+1}, \varrho \delta u^{n+1} + u^{n+1}),$$
$$I_5 = -2b(t^{n+1}; \delta^2 u^{n+1}, \varrho \delta u^{n+1} + u^{n+1}), \quad \text{and} \quad I_6 = 2b(t^{n+1}; u^{n+1}, \varrho \delta u^{n+1} + u^{n+1}).$$

Now, observe that

$$I_1 = 2\varrho \|\delta u^{n+1}\|^2 + \varrho(\delta^2 u^{n+1}, \delta u^{n+1}) + 2(\delta u^{n+1}, u^{n+1}) + (\delta^2 u^{n+1}, u^{n+1}),$$

so using 4.1.1.a with $k = 0, 1$ for the third and second terms respectively. And using 4.1.1.d with $k = 0$ for the last term we get

$$\begin{aligned} I_1 =& 2\varrho \|\delta u^{n+1}\|^2 + \frac{\varrho}{2}\delta \|\delta u^{n+1}\| + \frac{\varrho}{2}\|\delta^2 u^{n+1}\|^2 \\ &+ \delta \|u^{n+1}\|^2 + \|\delta u^{n+1}\|^2 + \frac{1}{2}\delta^2 \|u^{n+1}\|^2 + \frac{1}{2}\|\delta^2 u^{n+1}\|^2 - \|\delta u^n\|^2. \end{aligned} \tag{4.48}$$

Similarly we compute

$$\begin{aligned}
I_2 =&\varrho\delta\overline{a}(\delta u^{n+1},\delta u^{n+1}) + \varrho\overline{a}(\delta^2 u^{n+1},\delta^2 u^{n+1})\\
&+ \delta^2\overline{a}(u^{n+1},u^{n+1}) + \overline{a}(\delta^2 u^{n+1},\delta^2 u^{n+1}) - 2\overline{a}(\delta u^n,\delta u^n),\\
I_3 =&-\varrho a(t^{n+1};\delta u^{n+1},\delta u^{n+1}) + \varrho a(t^{n+1};\delta u^n,\delta u^n) - \varrho a(t^{n+1};\delta^2 u^{n+1},\delta^2 u^{n+1})\\
&- \delta^2 a(t^{n+1};u^{n+1},u^{n+1}) - a(t^{n+1};\delta^2 u^{n+1},\delta^2 u^{n+1}) + 2a(t^{n+1};\delta u^n,\delta u^n),
\end{aligned}$$

and

$$\begin{aligned}
I_4 =&\varrho a(t^{n+1};u^{n+1},u^{n+1}) - \varrho a(t^{n+1};u^n,u^n) + \varrho a(t^{n+1};\delta u^{n+1},\delta u^{n+1})\\
&+ 2a(t^{n+1};u^{n+1},u^{n+1}).
\end{aligned}$$

So summing,

$$\begin{aligned}
I_2 + I_3 + I_4 =&\Big(\varrho\delta\overline{a}(\delta u^{n+1},\delta u^{n+1})\Big)\\
&+ \Big((1+\varrho)\big(\overline{a}(\delta^2 u^{n+1},\delta^2 u^{n+1}) - a(t^{n+1};\delta^2 u^{n+1},\delta^2 u^{n+1})\big)\Big)\\
&+ \big(\varrho a(t^{n+1};\delta u^n,\delta u^n) - \overline{a}(\delta u^n,\delta u^n)\big) + 2a(t^{n+1};\delta u^n,\delta u^n)\\
&+ \Big(\delta^2\overline{a}(u^{n+1},u^{n+1}) + \varrho a(t^{n+1};u^{n+1},u^{n+1}) - \varrho a(t^{n+1};u^n,u^n)\Big)\\
&+ \Big(a(t^{n+1};u^{n+1},u^{n+1}) + 2a(t^{n+1};u^n,u^n) - a(t^{n+1};u^{n-1},u^{n-1})\Big).
\end{aligned}$$

By condition (4.44) the second term is positive, so we drop it. The third term is

positive since $\varrho = \frac{L_{\overline{a}}}{c}$ and by (4.34) and (4.43), so we drop it too. Then we get

$$\begin{aligned} I_2 + I_3 + I_4 \geq & \varrho\delta\overline{a}(\delta u^{n+1}, \delta u^{n+1}) + \frac{1}{2}a(t^{n+1}; \delta u^n, \delta u^n) \\ & + \delta^2\overline{a}(u^{n+1}, u^{n+1}) + \varrho a(t^{n+1}; u^{n+1}, u^{n+1}) \\ & - \varrho a(t^{n+1}; u^n, u^n) + a(t^{n+1}; u^{n+1}, u^{n+1}) + 2a(t^{n+1}; u^n, u^n) \\ & - a(t^{n+1}; u^{n-1}, u^{n-1}). \end{aligned}$$

Now, summing and subtracting $\varrho a(t^n; u^n, u^n)$, $2a(t^n; u^n, u^n)$, and $a(t^{n-1}; u^{n-1}, u^{n-1})$ in this last inequality,

$$\begin{aligned} I_2 + I_3 + I_4 \geq & \varrho\delta\overline{a}(\delta u^{n+1}, \delta u^{n+1}) + \frac{1}{2}a(t^{n+1}; \delta u^n, \delta u^n) + \delta^2\overline{a}(u^{n+1}, u^{n+1}) \\ & + \varrho a(t^{n+1}; u^{n+1}, u^{n+1}) - \varrho a(t^n; u^n, u^n) \\ & + \varrho|a(t^{n+1}; u^n, u^n) - a(t^n; u^n, u^n)| \\ & + |2a(t^{n+1}; u^n, u^n) - 2a(t^n; u^n, u^n)| \\ & + a(t^{n+1}; u^{n+1}, u^{n+1}) + 2a(t^n; u^n, u^n) - a(t^{n-1}; u^{n-1}, u^{n-1}). \end{aligned} \tag{4.49}$$

To bound the fourth and fifth terms we use property (4.36), and the mean value theorem,

$$\begin{aligned} I_2 + I_3 + I_4 \geq & \varrho\delta\overline{a}(\delta u^{n+1}, \delta u^{n+1}) + \frac{1}{2}a(t^{n+1}; \delta u^n, \delta u^n) + \delta^2\overline{a}(u^{n+1}, u^{n+1}) \\ & + \varrho a(t^{n+1}; u^{n+1}, u^{n+1}) - \varrho a(t^n; u^n, u^n) \\ & - C\Delta t|u^n|^2 - C\Delta t|u^{n-1}|^2 \\ & + \Big(a(t^{n+1}; u^{n+1}, u^{n+1}) + 2a(t^n; u^n, u^n) - a(t^{n-1}; u^{n-1}, u^{n-1})\Big). \end{aligned} \tag{4.50}$$

Observe that for the last term we have

$$
\begin{aligned}
a(t^{n+1};u^{n+1},u^{n+1}) + 2a(t^n;u^n,u^n) & \\
-a(t^{n-1};u^{n-1},u^{n-1}) &= \left(\frac{1}{2}+\frac{1}{2}\right)a(t^{n+1};u^{n+1},u^{n+1}) \\
&\quad + \left(\frac{3}{2}+\frac{1}{2}\right)a(t^n;u^n,u^n) \\
&\quad + (1-2)a(t^{n-1};u^{n-1},u^{n-1}) \\
&\geq \frac{c}{2}|u^{n+1}|^2 + \frac{c}{2}|u^n|^2 + c|u^{n-1}|^2 \\
&\quad + \frac{1}{2}a(t^{n+1};u^{n+1},u^{n+1}) + \frac{3}{2}a(t^n;u^n,u^n) \\
&\quad - 2a(t^{n-1};u^{n-1},u^{n-1}),
\end{aligned}
$$

where we have used property (4.34) for the last step. Using this last inequality in (4.50) and property (4.36) for the term $\frac{1}{2}a(t^{n+1};\delta u^n,\delta u^n)$ we obtain

$$
\begin{aligned}
I_2+I_3+I_4 \geq \varrho\delta\overline{a}(\delta u^{n+1},\delta u^{n+1}) &+ \frac{c}{2}|\delta u^n|^2 + \delta^2\overline{a}(u^{n+1},u^{n+1}) \\
&+ \varrho a(t^{n+1};u^{n+1},u^{n+1}) - \varrho a(t^n;u^n,u^n) \\
&+ \frac{c}{2}|u^{n+1}|^2 + \frac{c}{2}|u^n|^2 + c|u^{n-1}|^2 \\
&+ \frac{1}{2}a(t^{n+1};u^{n+1},u^{n+1}) + \frac{3}{2}a(t^n;u^n,u^n) \\
&- 2a(t^{n-1};u^{n-1},u^{n-1}) - C\Delta t|u^n|^2 - C\Delta t|u^{n-1}|^2.
\end{aligned} \tag{4.51}
$$

We now compute I_5 in (4.47) using items a) and d) of Proposition 4.1.1 as follows

$$\begin{aligned}
I_5 = &- \varrho b(t^{n+1}; \delta u^{n+1}, \delta u^{n+1}) + \varrho b(t^{n+1}; \delta u^n, \delta u^n) - \varrho b(t^{n+1}; \delta^2 u^{n+1}, \delta^2 u^{n+1}) \\
&- \varrho b(t^{n+1}; \delta u^{n+1}, \delta u^n) + \varrho b(t^{n+1}; \delta u^n, \delta u^{n+1}) \\
&- \delta^2 b(t^{n+1}; u^{n+1}, u^{n+1}) - b(t^{n+1}; \delta^2 u^{n+1}, \delta^2 u^{n+1}) + 2b(t^{n+1}; \delta u^n, \delta u^n) \\
&- b(t^{n+1}; \delta u^{n+1}, \delta u^n) + b(t^{n+1}; \delta u^n, \delta u^{n+1}) \\
&- b(t^{n+1}; u^{n+1}, u^n) + b(t^{n+1}; u^n, u^{n+1}) \\
&+ b(t^{n+1}; u^n, u^{n-1}) - b(t^{n+1}; u^{n-1}, u^n),
\end{aligned}$$

and for I_6 we use item b) of Proposition 4.1.1 to get

$$\begin{aligned}
I_6 = &\varrho b(t^{n+1}; u^{n+1}, u^{n+1}) - \varrho b(t^{n+1}; u^n, u^n) + \varrho b(t^{n+1}; \delta u^{n+1}, \delta u^{n+1}) \\
&- \varrho b(t^{n+1}; u^{n+1}, u^n) + \varrho b(t^{n+1}; u^n, u^{n+1}) + 2b(t^{n+1}; u^{n+1}, u^{n+1}).
\end{aligned}$$

Then summing,

$$\begin{aligned}
I_5 + I_6 = &(2+\varrho) b(t^{n+1}; \delta u^n, \delta u^n) - (1+\varrho) b(t^{n+1}; \delta^2 u^{n+1}, \delta^2 u^{n+1}) \\
&+ (1+\varrho) b(t^{n+1}; u^{n+1}, u^{n+1}) \\
&+ (2-\varrho) b(t^{n+1}; u^n, u^n) - b(t^{n+1}; u^{n-1}, u^{n-1}) \\
&- (1+\varrho) \big(b(t^{n+1}; \delta u^{n+1}, \delta u^n) - b(t^{n+1}; \delta u^n, \delta u^{n+1}) \big) \\
&- (1+\varrho) \left(b(t^{n+1}; u^{n+1}, u^n) - b(t^n; u^n, u^{n+1}) \right) \\
&+ b(t^{n+1}; u^n, u^{n-1}) - b(t^{n+1}; u^{n-1}, u^n).
\end{aligned}$$

We now bound the first five terms using inequality (4.40) with $\epsilon_2 = 2 + \varrho$, and $\epsilon_1 = \widehat{\epsilon_i}$ for $i = 1 \dots 5$, these five constants will be defined later. We also bound the

reamining terms of the above inequality with property (4.37), so we get

$$\begin{aligned} I_5 + I_6 \geq & -\Lambda_1\|\delta u^n\|^2 - \frac{c\widehat{\epsilon}_1}{2}|\delta u^n|^2 - \Lambda_2\|\delta^2 u^{n+1}\|^2 - \frac{c\widehat{\epsilon_2}}{2}|\delta^2 u^{n+1}|^2 \\ & - \Lambda_3\|u^{n+1}\|^2 - \frac{c\widehat{\epsilon}_3}{2}|u^{n+1}|^2 - \Lambda_4\|u^n\|^2 - \frac{c\widehat{\epsilon}_4}{2}|u^n|^2 \\ & - \Lambda_5\|u^{n-1}\|^2 - \frac{c\widehat{\epsilon}_5}{2}|u^{n-1}|^2 \\ & - \Big(\gamma|u^{n+1}| + |u^n|)\|\delta u^n\| + \gamma(|u^n| + |u^{n-1}|)\|\delta u^{n+1}\|\Big) \\ & - \Big(\gamma|u^{n+1}|\|u^n\| + \gamma|u^n|\|u^{n+1}\|\Big) \\ & - \Big(\widehat{C}|u^{n-1}|\|u^n\| + \widehat{C}|u^n|\|u^{n-1}\|\Big), \end{aligned} \tag{4.52}$$

where $\Lambda_j = \frac{1}{2c\widehat{\epsilon}_j}(2+\varrho)^2\left(\sum_i^d \|\eta_i\|_{L^\infty}\right)^2 + (2+\varrho)\|\eta\|_{L^\infty}$, and $\gamma = \widehat{C}(1+\varrho)$. Now, observe that

$$\begin{aligned} |\delta^2 u^{n+1}|^2 &= |\delta u^{n+1} - \delta u^n|^2 \\ &\leq |\delta u^{n+1}|^2 + 2|\delta u^{n+1}||\delta u^n| + |\delta u^n|^2 \\ &\leq 2|\delta u^{n+1}|^2 + 2|\delta u^n|^2 \\ &\leq 4|u^{n+1}| + 4|u^n| + 2|\delta u^n|^2, \end{aligned} \tag{4.53}$$

where Cauchy-Schwarz inequality has been used in the second and last steps. So

using (4.53) in (4.52) and regrouping terms we get

$$
\begin{aligned}
I_5 + I_6 \geq & -\frac{c}{2}\left(\widehat{\epsilon}_1 + 2\widehat{\epsilon}_2\right)|\delta u^n|^2 - \frac{c}{2}\left(4\widehat{\epsilon}_2 + \widehat{\epsilon}_3\right)|u^{n+1}|^2 \\
& - \frac{c}{2}(4\widehat{\epsilon}_2 + \widehat{\epsilon}_4)|u^n|^2 - \frac{c}{2}\widehat{\epsilon}_5|u^{n-1}|^2 \\
& - \gamma(|u^{n+1}| + |u^n|)\|\delta u^n\| - \gamma(|u^n| + |u^{n-1}|)\|\delta u^{n+1}\| \\
& - \gamma|u^{n+1}|\|u^n\| - \gamma|u^n|\|u^{n+1}\| \\
& - \widehat{C}|u^{n-1}|\|u^n\| - \widehat{C}|u^n|\|u^{n-1}\|, \\
& - \Lambda_1\|\delta u^n\|^2 - \Lambda_2\|\delta^2 u^{n+1}\|^2 - \Lambda_3\|u^{n+1}\|^2 - \Lambda_4\|u^n\|^2 - \Lambda_5\|u^{n-1}\|^2
\end{aligned}
\tag{4.54}
$$

To bound even further, we use Cauchy's inequality (4.9) to all the terms that contain γ and the las term of (4.54); namely,

$$
\begin{aligned}
\gamma\big(|u^{n+1}| + |u^n|\big)\|\delta u^n\| &\leq \left(\frac{1}{2c\epsilon_1} + \frac{1}{2c\epsilon_2}\right)\gamma^2\|\delta u^n\|^2 + \frac{c\epsilon_1}{2}|u^{n+1}|^2 + \frac{c\epsilon_2}{2}|u^n|^2, \\
\gamma\big(|u^n| + |u^{n-1}|\big)\|\delta u^{n+1}\| &\leq \left(\frac{1}{2c\epsilon_3} + \frac{1}{2c\epsilon_4}\right)\gamma^2\|\delta u^{n+1}\|^2 + \frac{c\epsilon_3}{2}|u^n|^2 + \frac{c\epsilon_4}{2}|u^{n-1}|^2, \\
\gamma|u^{n+1}|\|u^n\| + \gamma|u^n|\|u^{n+1}\| &\leq \frac{\gamma^2}{2c\epsilon_5}\|u^n\|^2 + \frac{c\epsilon_5}{2}|u^{n+1}|^2 + \frac{\gamma^2}{2c\epsilon_6}\|u^{n+1}\|^2 + \frac{c\epsilon_6}{2}|u^n|^2,
\end{aligned}
$$

and

$$
\widehat{C}|u^{n-1}|\|u^n\| + \widehat{C}|u^n|\|u^{n-1}\| \leq \frac{\widehat{C}^2}{2c\epsilon_7}\|u^n\|^2 + \frac{c\epsilon_7}{2}|u^{n-1}|^2 + \frac{\widehat{C}^2}{2c\epsilon_8}\|u^{n-1}\|^2 + \frac{c\epsilon_8}{2}|u^n|^2.
$$

Recall that we need to compute (4.47), so the objective is to balance all the terms containing the norm $|\cdot|$ in (4.51) and (4.54). So using the above four inequalities we

need to solve

$$\begin{cases} \widehat{\epsilon_1} + 2\widehat{\epsilon_2} & = 1, \\ 4\widehat{\epsilon_2} + \widehat{\epsilon_3} + \epsilon_1 + \epsilon_5 & = 1, \\ 4\widehat{\epsilon_2} + \widehat{\epsilon_4} + \epsilon_2 + \epsilon_3 + \epsilon_6 + \epsilon_8 & = 1, \\ \widehat{\epsilon_5} + \epsilon_4 + \epsilon_7 & = 2. \end{cases} \tag{4.55}$$

We see that choosing $\widehat{\epsilon_3} = \epsilon_1 = \epsilon_5 = 1/8$, $\widehat{\epsilon_2} = 5/32$, $\widehat{\epsilon_1} = 11/16$, $\widehat{\epsilon_4} = \epsilon_2 = \epsilon_3 = \epsilon_6 = \epsilon_8 = 3/40$, $\epsilon_4 = \epsilon_7 = 1/2$ and $\widehat{\epsilon_5} = 1$ satisfy the above system of linear equations. So we have that

$$\begin{aligned} I_2 + I_3 + I_4 + I_5 + I_6 \geq & - \left(\Lambda_3 + \frac{20}{3c}\gamma^2\right) \|u^{n+1}\|^2 \\ & - \frac{23}{3c}\gamma^2 \|\delta u^{n+1}\|^2 - \Lambda_2 \|\delta^2 u^{n+1}\|^2 + \varrho \delta \overline{a}(\delta u^{n+1}, \delta u^{n+1}) \\ & + \delta^2 \overline{a}(u^{n+1}, u^{n+1}) + \varrho a(t^{n+1}; u^{n+1}, u^{n+1}) \\ & - \varrho a(t^n; u^n, u^n) + \frac{1}{2} a(t^{n+1}; u^{n+1}, u^{n+1}) + \frac{3}{2} a(t^n; u^n, u^n) \\ & - 2a(t^{n-1}; u^{n-1}, u^{n-1}) - C\Delta t |u^n|^2 - C\Delta t |u^{n-1}|^2 \\ & - C\|\delta u^n\|^2 - C\|u^n\|^2 - C\|u^{n-1}\|^2. \end{aligned}$$

Using this last inequality, and (4.48) we have in (4.47) that

$$\begin{aligned}
&\left(1+\frac{5\varrho}{2}-\frac{20}{3c}\gamma^2\Delta t\right)\|\delta u^{n+1}\|^2+\left(\frac{1+\varrho}{2}-\Lambda_2\Delta t\right)\|\delta^2 u^{n+1}\|^2\\
&+\left(\frac{3}{2}-\left(\Lambda_3+\frac{23}{3c}\gamma^2\right)\Delta t\right)\|u^{n+1}\|^2+\Delta t\varrho\overline{a}(\delta u^{n+1},\delta u^{n+1})\\
&+\Delta t\overline{a}(u^{n+1},u^{n+1})+\Delta t\varrho a(t^{n+1};u^{n+1},u^{n+1})+\frac{\Delta t}{2}a(t^{n+1};u^{n+1},u^{n+1})\\
&\qquad\le\left(1+\frac{\varrho}{2}+C\Delta t\right)\|\delta u^n\|^2+(2+C\Delta t)\|u^n\|^2-\left(\frac{1}{2}+C\Delta t\right)\|u^{n-1}\|^2\\
&\qquad\quad+\Delta t\varrho\overline{a}(\delta u^n,\delta u^n)+2\Delta t\overline{a}(u^n,u^n)-\Delta t\overline{a}(u^{n-1},u^{n-1})+\Delta t\varrho a(t^n;u^n,u^n)\\
&\qquad\quad-\frac{3\Delta t}{2}a(t^n;u^n,u^n)+2\Delta t a(t^{n-1};u^{n-1},u^{n-1})+C\Delta t^2|u^n|^2+C\Delta t^2|u^{n-1}|^2,
\end{aligned}$$

By condition (4.46) the second term is positive, so we drop it, and summing we get

$$\begin{aligned}
&\left(1+\frac{\varrho}{2}-\frac{20}{3c}\gamma^2\Delta t\right)\|\delta u^{n+1}\|^2+\left(\frac{3}{2}-\left(\Lambda_3+\frac{23}{3c}\gamma^2\right)\Delta t\right)\|u^{n+1}\|^2\\
&+\Delta t\varrho\overline{a}(\delta u^{n+1},\delta u^{n+1})+\Delta t\overline{a}(u^{n+1},u^{n+1})+\Delta t\varrho a(t^{n+1};u^{n+1},u^{n+1})\\
&+\frac{\Delta t}{2}a(t^{n+1};u^{n+1},u^{n+1})\\
&\qquad\le\sum_{k=2}^{n}C\Delta t\|\delta u^k\|^2+\sum_{k=2}^{n}C\Delta t\|u^k\|^2+\sum_{k=2}^{n}C\Delta t^2|\delta u^k|^2+\sum_{k=2}^{n}C\Delta t^2|u^k|^2\\
&\qquad\quad+(1+\frac{\varrho}{2}+C\Delta t)\|\delta u^1\|^2+\left(\frac{3}{2}+C\Delta t\right)\|u^1\|^2+\Delta t\varrho\overline{a}(\delta u^1,\delta u^1)+\Delta t\overline{a}(u^1,u^1)\\
&\qquad\quad+\Delta t\varrho a(t^1;u^1,u^1)+\left(\frac{\Delta t}{2}+C\Delta t^2\right)a(t^1;u^1,u^1)+(2\Delta t+C\Delta t^2)a(t^0;u^0,u^0).
\end{aligned}$$

Using (4.34) and (4.42) to bound all terms of the left hand side which have $a(\cdot;\cdot,\cdot)$

and $\overline{a}(\cdot;\cdot,\cdot)$ respectively, we finally compute

$$\begin{aligned}
&\beta_1\|\delta u^{n+1}\|^2+\beta_2\|u^{n+1}\|^2\\
&+\Delta t\varrho l_{\overline{a}}\cdot|\delta u^{n+1}|^2+\left(l_{\overline{a}}+c\varrho+\frac{c}{2}\right)\Delta t|u^{n+1}|^2\\
&\qquad\leq C\Bigg(\sum_{k=2}^{n}\Delta t\|\delta u^k\|^2+\sum_{k=2}^{n}\Delta t\|u^k\|^2+\sum_{k=2}^{n}\Delta t^2|\delta u^k|^2+\sum_{k=2}^{n}\Delta t^2|u^k|^2\\
&\qquad\qquad+\|\delta u^1\|^2+\|u^1\|^2+\Delta t|\delta u^1|^2+\Delta t|u^1|^2+\Delta t|u^0|^2\Bigg).
\end{aligned}$$

where $\beta_1=1+\frac{\varrho}{2}-\frac{20}{3c}\gamma^2\Delta t$, and $\beta_2=\frac{3}{2}-\left(\Lambda_3+\frac{23}{3c}\gamma^2\right)\Delta t$. By condition (4.46), β_1 and β_2 are positive; moreover, β_1^{-1} and β_2^{-1} are uniformly bounded below. So the result follows using Gronwall's Lemma 4.2.1. □

As in Theorems 4.1.1 and 4.1.2, condition (4.46) is too restrictive. However, as shown in the following experiments, numerical evidence suggests that scheme (4.41) is stable for $\Delta t\sim O(h)$ using finite elements where h is the mesh size.

4.2.3 Numerical experiments in $\mathbb{R}^2$

We test numerically our scheme (4.41) when $\Omega\subset\mathbb{R}^2$ with the following parabolic PDE,

$$\begin{cases}
\partial_t u+\frac{u}{2}\frac{\partial_t\eta}{\eta}-\nabla\cdot\left(\nabla\left(\eta u\right)\right)=f(\mathbf{x},t) & \mathbf{x}\in\Omega,0<t\leq T,\\
u(\mathbf{x},t)=0 & \mathbf{x}\in\partial\Omega,0<t\leq T,\\
u(\mathbf{x},0)=u^0 & \mathbf{x}\in\Omega,
\end{cases}\tag{4.56}$$

where

$$\eta(x,y,t)=\frac{1}{1-\beta\cdot s(r)\cos(\theta-2\pi t)}.$$

Moreover, Ω, $s(r)$ and β are the same as defined in subsection 4.1.3. Observe (4.56) is not in conservative form as in (4.30), but we can still define the bilinear

forms in (4.31) as

$$a(t;u,v) = \int_\Omega \eta \nabla u \cdot \nabla v dx,$$
$$\text{and} \quad b(t;u,v) = \int_\Omega u \nabla \eta \cdot \nabla v dx + \int_\Omega \frac{\partial_t \eta}{2\eta} uv dx.$$

We set as an analytical solution of (4.56) $u(x,y,t) = \eta^{-1}\cos(x+y+t)$, and compute f accordingly. We also choose

$$\overline{a}(u,v) = \overline{\eta} \int_\Omega \nabla u \nabla v dx,$$

where $\overline{\eta} = \sup_{(x,y,t)\in\Omega\times[0,T]} \eta(x,y,t)$ as in (4.45), so conditions (4.42)-(4.44) are satisfied. Table 4.3 shows time and space convergence of scheme (4.41) which is referred as BDF2**. To get these results we discretized spatially using $\mathbb{P}_2$ Lagrange finite elements using a uniform mesh, and setting a difference ratio $r_\eta = 100$, then $\overline{\eta} = 100$.

(a) Time convergence rate at $T = 10$ and using $h = 2^{-6}$.

Δt	BDF2**	
	L_2 Rel. Error	COC
0.100000	6.9898E-01	—
0.050000	2.0186E-01	1.79
0.025000	6.0391E-02	1.74
0.012500	1.4095E-02	2.10
0.006250	3.4316E-03	2.04
0.003125	8.5332E-04	2.01

(b) Space convergence rate at $T = 1$.

h	BDF2**	
	L_2 Rel. Error	COC
2^{-3}	7.5515E-03	—
2^{-4}	6.6648E-04	3.50
2^{-5}	4.1190E-05	4.02
2^{-6}	2.9285E-06	3.81

Table 4.3: Solving model (4.56) in $\mathbb{R}^2$ using FEM. $L^\infty([0,T], L^2(\Omega))$ errors for $r_\eta = 100$.

5. NUMERICAL SIMULATION OF KINEMATIC DYNAMOS

In this section we first introduce a new time stepping scheme for solving Maxwell equations (3.8) when $\mu = \mu(\mathbf{x}, t)$. This novel scheme is capable of avoiding implicit convolutions using only constant matrices when hybrid Fourier-Finite elements are used. Then in subsection 5.4 we report some convergence tests using this new scheme, which has been implemented on an extended version of `SFEMaNS`. In subsection 5.6 we report and validate simulations for the kinematic dynamo problem using the half VKS setting. We first compare our code `SFEMaNS` againts the 3D code `DOLMEN` (see Zaidi *et al.* [67]). All figures related to `DOLMEN` are courtesy of C. Nore and F. Bouillault. Part of the data reported using `SFEMaNS` in subsection 5.6 is reprinted with permission from [44].

5.1 PDE Setting and Variational Weak Form

Following the discussion in subsection 3.7 and the results of section 4, we propose to do a change of variables in the MHD equations; specifically, we use the magnetic induction field $\mathbf{B}$ instead of $\mathbf{H}$. Recalling that $\mathbf{B} = \mu\mathbf{H}$, the Maxwell equations (3.8)

are now as follows:

$$
\begin{cases}
\partial_t \mathbf{B}^c = -\nabla\times(R_{\mathrm{m}}^{-1}\sigma^{-1}(\nabla\times(\frac{\mathbf{B}^c}{\mu^c}) - \mathbf{j}^s) - \tilde{\mathbf{u}}\times\mathbf{B}^c) & \text{in every} \quad \Omega_{ci}, \quad i \in \overline{1,N}, \\
\mu^v \partial_t \Delta\phi = 0, & \text{in} \quad \Omega_v, \\
(R_{\mathrm{m}}^{-1}\sigma^{-1}(\nabla\times(\frac{\mathbf{B}^c}{\mu^c}) - \mathbf{j}^s) - \tilde{\mathbf{u}}\times\mathbf{B}^c)\times\mathbf{n}^c = \mathbf{a} & \text{on} \quad \Gamma_{c,n}, \\
\frac{\mathbf{B}^c}{\mu^c}\times\mathbf{n} = \frac{\mathbf{B}_d^c}{\mu^c}\times\mathbf{n} & \text{on} \quad \Gamma_{c,d}, \\
\mu^v \partial_{\mathbf{n}^v}\partial_t\phi = -\mathbf{n}^v\cdot\nabla\times(\mathbf{n}^v\times\mathbf{a}), & \text{on} \quad \Gamma_v, \\
\frac{\mathbf{B}_1^c}{\mu_1^c}\times\mathbf{n}_1^c + \frac{\mathbf{B}_2^c}{\mu_2^c}\times\mathbf{n}_2^c = 0 & \text{on} \quad \Sigma_\mu, \\
\mathbf{B}_1^c\cdot\mathbf{n}_1^c + \mathbf{B}_2^c\cdot\mathbf{n}_2^c = 0 & \text{on} \quad \Sigma_\mu, \\
\frac{\mathbf{B}^c}{\mu^c}\times\mathbf{n}^c + \nabla\phi\times\mathbf{n}^v = 0 & \text{on} \quad \Sigma, \\
\mathbf{B}^c\cdot\mathbf{n}^c + \mu^v\nabla\phi\cdot\mathbf{n}^v = 0 & \text{on} \quad \Sigma, \\
\mathbf{B}|_{t=0} = \mathbf{B}_0, \quad \phi|_{t=0} = \phi_0 & \text{in} \quad \Omega.
\end{cases}
\tag{5.1}
$$

For the time being we assume $\mu = \mu(\Omega)$ only, and there are no Dirichlet boundary conditions for $\mathbf{B}^c$, i.e, $\Gamma_{c,d} = \emptyset$. We now get a continuous weak form of the above system (5.1). Let us recall the spaces $\mathbf{L}$ and $\mathbf{X}$ defined in subsection 3.4 as

$$
\begin{aligned}
\mathbf{L} &= \left\{ (\mathbf{b},\phi) \in \mathbf{L}^2(\Omega_c)\times H^1_{\int=0}(\Omega_v) \right\}, \\
\mathbf{X} &= \left\{ (\mathbf{b},\phi) \in \mathbf{H}_{\mathrm{curl}}(\Omega_c)\times H^1_{\int=0}(\Omega_v); (\mathbf{b}\times\mathbf{n}^c + \nabla\phi\times\mathbf{n}^v)|_\Sigma = 0 \right\}.
\end{aligned}
$$

Because we want to include the term $\left(\frac{\mathbf{B}^c}{\mu^c}\times\mathbf{n}^c + \nabla\phi\times\mathbf{n}^v\right)$ as a natural boundary condition, and avoid implicit convolutions involving the term $\partial_t\mathbf{B}^c$, we propose to use a continuous Petrov-Galerkin weak formulation. For that we first introduce the

space,

$$\mathbf{Y} = \left\{ \left(\frac{\mathbf{b}}{\mu^c}, \phi \right) \in \mathbf{H}_{\mathrm{curl}}(\Omega) \times H^1_{\int=0}(\Omega_v); \left(\frac{\mathbf{b}}{\mu^c} \times \mathbf{n}^c + \nabla\phi \times \mathbf{n}^v \right) |_\Sigma = 0 \right\}.$$

Then the proposed continuous weak form of (5.1) is to seek the pair $(\mathbf{B}, \phi) \in L^2((0,+\infty); \mathbf{Y}) \cap L^\infty((0,+\infty); \mathbf{L})$ such that for all pairs $(\mathbf{b}, \psi) \in \mathbf{X}$ and for almost every $t \in (0,+\infty)$,

$$\begin{cases} \mathbf{B}|_{t=0} = \mathbf{B}_0, \quad \nabla\phi|_{t=0} = \nabla\phi_0, \\ \int_{\Omega_c} \partial_t \mathbf{B} \cdot \mathbf{b} + \int_{\Omega_c} \left(R_{\mathrm{m}}^{-1} \sigma^{-1} \left(\nabla\times \left(\frac{\mathbf{B}^c}{\mu^c} \right) - \mathbf{j}^s \right) - \tilde{\mathbf{u}} \times \mathbf{B}^c \right) \cdot \nabla\times\mathbf{b} \\ + \int_{\Omega_v} \mu^v \partial_t(\nabla\phi) \cdot \nabla\psi \\ + \int_{\Sigma_\mu} \left\{ R_{\mathrm{m}}^{-1} \sigma^{-1} \left(\nabla\times \frac{\mathbf{B}^c}{\mu^c} - \mathbf{j}^s \right) - \tilde{\mathbf{u}} \times \mathbf{B}^c \right\} \cdot (\mathbf{b}_1 \times \mathbf{n}_1^c + \mathbf{b}_2 \times \mathbf{n}_2^c) \\ + \int_\Sigma \left(R_{\mathrm{m}}^{-1} \sigma^{-1} (\nabla\times \frac{\mathbf{B}^c}{\mu^c} - \mathbf{j}^s) - \tilde{\mathbf{u}} \times \mathbf{B}^c \right) \cdot (\mathbf{b} \times \mathbf{n}_1^c + \nabla\psi \times \mathbf{n}^v) \\ = \int_{\Gamma_c} (\mathbf{a} \times \mathbf{n}) \cdot (\mathbf{b} \times \mathbf{n}) + \int_{\Gamma_v} (\mathbf{a} \times \mathbf{n}) \cdot (\nabla\psi \times \mathbf{n}). \end{cases} \tag{5.2}$$

The properties of the above weak form such as existence and uniqueness of solutions are left for future research.

5.2 Finite Element Discretization

We keep the same notation and setting as in subsection 3.5.1. The finite element method we use to discretize (5.1) is still non-conforming, i.e., the continuity constraints $(\mathbf{b}\times\mathbf{n}^c + \nabla\varphi\times\mathbf{n}^v)|_\Sigma = 0$, and $(\mathbf{b}_1\times\mathbf{n}_1^c + \mathbf{b}_2\times\mathbf{n}_2^c)|_{\Sigma_\mu} = 0$ in $\mathbf{X}$, and the continuity constraints $(\frac{\mathbf{b}}{\mu}\times\mathbf{n}^c + \nabla\varphi\times\mathbf{n}^v)|_\Sigma = 0$, and $(\frac{\mathbf{b}_1}{\mu_1}\times\mathbf{n}_1^c + \frac{\mathbf{b}_2}{\mu_2}\times\mathbf{n}_2^c)|_{\Sigma_\mu} = 0$ in $\mathbf{Y}$ are relaxed and enforced by means of an interior penalty method.

Let $\ell_{\mathbf{B}}$, and ℓ_ϕ be two integers in $\{1, 2\}$ with $\ell_\phi \geq \ell_{\mathbf{B}}$. We define the meridional

finite element spaces,

$$\mathbf{X}_h^{\mathbf{B},2D} := \{\mathbf{b}_h \in \mathbf{L}^2(\Omega_c);\, \mathbf{b}_h|_{\Omega_{ci}} \in \boldsymbol{\mathcal{C}}^0(\overline{\Omega_{ci}}), \forall i = 1, \ldots, N, \mathbf{b}_h(T_K)|_K \in \mathbb{P}_{\ell_{\mathbf{B}}},\ \forall K \in \mathcal{F}_h^c\},$$
$$X_h^{\phi,2D} := \{\varphi_h \in \mathcal{C}^0(\overline{\Omega_v});\, \varphi_h(T_K)|_K \in \mathbb{P}_{\ell_\phi},\ \forall K \in \mathcal{F}_h^v\},$$

where $\mathbb{P}_k$ denotes the set of bivariate polynomials of total degree at most k, and $\mathbb{P}_k := \mathbb{P}_k \times \mathbb{P}_k \times \mathbb{P}_k$. Then, using the complex notation $\mathrm{i}^2 = -1$, the fields $\mathbf{B}$, $\mathbf{H}$ and the scalar potential ϕ are approximated in the following spaces:

$$\mathbf{X}_h^{\mathbf{B}} := \{\mathbf{b} = \sum_{m=-M}^{M} \mathbf{b}_h^m(r,z)e^{\mathrm{i}m\theta};\, \mathbf{b}_h^m \in \mathbf{X}_h^{\mathbf{B},2D},\ \overline{\mathbf{b}_h^m} = \mathbf{b}_h^{-m},\ k \in \overline{0,M}\},$$
$$\mathbf{X}_h^{\mathbf{H}} := \mathbf{X}_h^{\mathbf{B}},$$
$$X_h^{\phi} := \{\varphi = \sum_{m=-M}^{M} \varphi_h^m(r,z)e^{\mathrm{i}m\theta};\, \varphi_h^m \in X_h^{\phi,2D},\ \overline{\varphi_h^m} = \varphi_h^{-m},\ m \in \overline{0,M}\},$$

where $M+1$ is the maximum number of complex Fourier modes.

As in subsection 3.5.2, we introduce a magnetic pressure p^c to control the divergence condition $\nabla\cdot\mathbf{B} = 0$ weakly in the dual space of $H_0^s(\Omega)$ where $\frac{1}{2} < s \leq 1$. So let us recall the following finite element spaces,

$$X_h^{p,2D} := \left\{p_h \in L^2(\Omega_c)\ /\ p_h \in \mathcal{C}^0(\overline{\Omega_c}),\ p_h(T_K) \in \mathbb{P}_{\ell_p},\ \forall K \in \mathcal{F}_h^c,\ p_h = 0 \text{ on } \partial\Omega_c\right\},$$
$$X_h^{p} := \left\{p = \sum_{m=-M}^{M} p_h^m(r,z)\mathrm{e}^{\mathrm{i}m\theta}\ /\ \forall m = 1\ldots, M,\ p^m \in X_h^{p,2D} \text{ and } p_h^m = \overline{p_h^{-m}}\right\},$$

where ℓ_p is an integer in {1,2}.

5.3 Time Discretization Scheme

For the rest of this section, we now consider μ^c to be dependent of time as well, i.e., $\mu^c = \mu^c(\Omega, t)$. Moreover, let us drop the assumption of not having Dirichlet

boundary conditions, i.e, we now assume $\Gamma_{c,d} \neq \emptyset$. As usual let Δt be the time step and set $t^n := n\Delta t, n \geq 0$. After proper initialization at t^0 and t^1, we define

$$D\mathbf{B}^{c,n+1} = \frac{1}{2}(3\mathbf{B}^{c,n+1} - 4\mathbf{B}^{c,n} + \mathbf{B}^{c,n-1}), \tag{5.3}$$

and

$$\mathbf{B}^* = 2\mathbf{B}^{c,n} - \mathbf{B}^{c,n-1}. \tag{5.4}$$

Now, in order to avoid implicit convolutions to solve (5.1), we mimic what is done in schemes (4.17) and (4.41). Specifically, we discretize explicitely in time the term

$$-\nabla\times\left(R_{\mathrm{m}}^{-1}\sigma^{-1}\left(\nabla\times\left(\frac{\mathbf{B}^c}{\mu^c}\right)^* - \mathbf{j}^s\right) - \tilde{\mathbf{u}}\times\mathbf{B}^*\right) \tag{5.5}$$

in the first equation of (5.1) and use integration by parts similarly as in (5.2). Moreover, we also add artificial difussion through the curl operator including the term

$$-\nabla\times\left(R_{\mathrm{m}}^{-1}\sigma^{-1}\nabla\times\left(\frac{\delta^2\mathbf{B}^{c,n+1}}{\overline{\mu^c}}\right)\right), \tag{5.6}$$

in (5.1). Let use recall that $\delta^2(\cdot)$ is defined in (4.15), and is always consistent and second order accurate in time. The function $\overline{\mu^c}$ is a parameter function in the same spirit as $\overline{\eta}$ in schemes (4.17), (4.41) and (4.45) where $\eta = \mu^{-1}$, and needs to satisfy the following conditions:

$$\overline{\mu^c} \leq \mu^c \quad \text{in} \quad \Omega_c, \qquad 0 \leq t \leq T, \tag{5.7}$$

$$\overline{\mu^c} = \mu^c \quad \text{on} \quad \Sigma, \Sigma_\mu, \text{and} \quad \Gamma_{c,d}, \qquad 0 \leq t \leq T, \tag{5.8}$$

$$\overline{\mu^c} = \overline{\mu^c}(\Omega_{ci}^{2D}), \qquad i \in \overline{1,N}, \tag{5.9}$$

where we recall that Ω_{ci}^{2D} has been defined in subsection 3.5.1 as the meridional portion of the axisymmetric connected component Ω_{ci} of Ω. We give now a description of why (5.7)-(5.9) are needed for our numerical method. Condition (5.7) is the equivalent of condition (4.18), which is used to guarantee stability of schemes (4.17), and (4.41) in Theorems (4.1.2) and (4.2.1), respectively. Using condition (5.8) avoids cumbersome terms involving $\mathbf{B}^*$ on the interfaces Σ and Σ_μ. Those appear when integration by parts is used for both terms (5.5) and (5.6). Moreover, by condition (5.8) we can implement Dirichlet boundary conditions on $\Gamma_{c,d}$ similarly as it is done in scheme (3.16). Condition (5.9) means that $\overline{\mu^c}$ is independent of t and θ, which makes our algorithm to generate time independent matrices that avoid implicit convolutions.

Our proposed scheme to solve (5.1) is to compute in one step by solving $\mathbf{B}^{c,n+1} \in \mathbf{X}_h^{\mathbf{B}}$, $\phi^{n+1} \in X_h^\phi$ and $p^{c,n+1} \in X_h^p$, so that the following holds for all $\mathbf{b} \in \mathbf{X}_h^{\mathbf{H}}$, $\varphi \in X_h^\phi$ and $q \in X_h^p$,

$$\begin{cases} \mathbf{B}^c|_{t=0} = \mathbf{B}_0^c, \\ \int_{\Omega_c} \frac{D\mathbf{B}^{c,n+1}}{\Delta t}\cdot\mathbf{b} + \int_{\Omega_v} \mu^v \frac{\nabla D\phi^{n+1}}{\Delta t}\cdot\nabla\varphi + \overline{\mathcal{L}}((\mathbf{B}^{c,n+1},\phi^{n+1}),(\mathbf{b},\varphi)) \\ +\mathcal{P}(\phi^{n+1},\varphi) + \overline{\mathcal{D}}((\mathbf{B}^{c,n+1},p^{n+1}),(\mathbf{b},q)) + \overline{\mathcal{E}}(\mathbf{B}^{c,n+1},\mathbf{b}) = \overline{\mathcal{R}}_n(\mathbf{b},\varphi), \end{cases} \tag{5.10}$$

where,

$$\begin{aligned} \overline{\mathcal{L}}((\mathbf{B},\phi),(\mathbf{b},\varphi)) = &\int_{\Omega_c} \frac{1}{\sigma R_m}\nabla\times\left(\frac{\mathbf{B}}{\overline{\overline{\mu^c}}}\right)\cdot\nabla\times\mathbf{b} \\ &+ \int_{\Sigma_\mu}\left\{\frac{1}{\sigma R_m}\nabla\times\left(\frac{\mathbf{B}}{\overline{\overline{\mu^c}}}\right)\right\}\cdot(\mathbf{b}_1\times\mathbf{n}_1^c + \mathbf{b}_2\times\mathbf{n}_2^c) \\ &+ \overline{g}((\mathbf{B},\phi),(\mathbf{b},\varphi)) + \int_\Sigma \frac{1}{\sigma R_m}\nabla\times\left(\frac{\mathbf{B}}{\overline{\overline{\mu^c}}}\right)\cdot(\mathbf{b}\times\mathbf{n}^c + \nabla\varphi\times\mathbf{n}^v)\,. \end{aligned}$$

Similar to $g((\mathbf{H},\phi),(\mathbf{b},\varphi))$ in (3.16), the bilinear form $\overline{g}((\mathbf{B},\phi),(\mathbf{b},\varphi))$ penalizes the jumps conditions on Σ and Σ_μ using interior penalty method; namely,

$$\begin{aligned}\overline{g}((\mathbf{B},\phi),(\mathbf{b},\varphi)) = \beta_3 \sum_{F\in\Sigma_\mu} h_F^{-1} \int_F \left(\frac{\mathbf{B}_1}{\overline{\overline{\mu^c}}_1}\times\mathbf{n}_1^c + \frac{\mathbf{B}_2}{\overline{\overline{\mu_2^c}}}\times\mathbf{n}_2^c\right)\cdot(\mathbf{b}_1\times\mathbf{n}_1^c+\mathbf{b}_2\times\mathbf{n}_2^c)\\ + \beta_1 \sum_{F\in\Sigma_\mu} h_F^{-1} \int_F (\mathbf{B}_1\cdot\mathbf{n}_1^c+\mathbf{B}_2\cdot\mathbf{n}_2^c)\cdot\left(\overline{\mu_1^c}\mathbf{b}_1\cdot\mathbf{n}_1^c+\overline{\mu_2^c}\mathbf{b}_2\cdot\mathbf{n}_2^c\right)\\ + \beta_2 \sum_{F\in\Sigma} h_F^{-1} \int_F \left(\frac{\mathbf{B}}{\overline{\overline{\mu^c}}}\times\mathbf{n}_1^c+\nabla\phi\times\mathbf{n}_2^c\right)\cdot(\mathbf{b}\times\mathbf{n}^c+\nabla\varphi\times\mathbf{n}^v)\\ + \beta_1 \sum_{F\in\Sigma} h_F^{-1} \int_F (\mathbf{B}\cdot\mathbf{n}_1^c+\nabla\phi\cdot\mathbf{n}_2^c)\cdot(\overline{\mu^c}\mathbf{b}\cdot\mathbf{n}^c+\nabla\varphi\cdot\mathbf{n}^v),\end{aligned}$$

where β_1,β_2,β_3 are penalization constant parameters and user dependent. The bilinear form $\mathcal{P}(\phi,\varphi)$ is the same as in (3.16), but let us recall that

$$\mathcal{P}(\phi,\varphi) = \int_{\Omega_v}\mu^v\nabla\phi\cdot\nabla\varphi - \int_{\partial\Omega_v}\mu^v\varphi\mathbf{n}\cdot\nabla\phi.$$

Similar to $\mathcal{D}((\mathbf{H},p),(\mathbf{b},q))$ in (3.17), the bilinear form $\overline{\mathcal{D}}((\mathbf{B},p),(\mathbf{b},q))$ controls the divergence condition $\nabla\cdot\mathbf{B}^c=0$ weakly,

$$\begin{aligned}\overline{\mathcal{D}}((\mathbf{B},p),(\mathbf{b},q)) =& \beta_1\left(\int_{\Omega_c}\overline{\mu^c}\nabla p\cdot\mathbf{b} - \int_{\Omega_c}\mathbf{B}\cdot\nabla q + \sum_{K\in\mathcal{F}_h^c}\int_{K^{3D}} h_K^{2(1-\alpha)}\nabla p\cdot\nabla q\right)\\ &+ \beta_1\sum_{K\in\mathcal{F}_h^c} h_K^{2\alpha}\int_{K^{3D}}\overline{\mu^c}\nabla\cdot\mathbf{B}\nabla\cdot\mathbf{b}.\end{aligned}$$

As the bilinear form $\mathcal{E}(\mathbf{H},\mathbf{b})$ does in (3.18), the form $\overline{\mathcal{E}}(\mathbf{B},\mathbf{b})$ imposes the Dirichlet

boundary conditions on $\Gamma_{c,d}$ weakly

$$\overline{\mathcal{E}}(\mathbf{B},\mathbf{b}) = \int_{\Gamma_{c,d}} \frac{1}{\sigma R_m}\left(\nabla\times\left(\frac{\mathbf{B}}{\overline{\overline{\mu^c}}}\right)\right)\cdot(\mathbf{b}\times\mathbf{n}^c) + \beta_4\left(\sum_{F\in\Gamma_{c,d}} h_F^{-1}\int_F\left(\frac{\mathbf{B}}{\overline{\overline{\mu^c}}}\times\mathbf{n}^c\right)\cdot(\mathbf{b}\times\mathbf{n}^c)\right),$$

where β_4 is a user dependent parameter. The right hand side bilinear form $\overline{\mathcal{R}}_n(\mathbf{b},\varphi)$ is defined as

$$\begin{aligned}\overline{\mathcal{R}}_n(\mathbf{b},\varphi) = &\int_{\Omega_c}\frac{1}{\sigma R_m}\nabla\times\left(\frac{\mathbf{B}^*}{\overline{\overline{\mu^c}}}\right)\cdot\nabla\times\mathbf{b} - \int_{\Omega_c}\frac{1}{\sigma R_m}\nabla\times\left(\frac{\mathbf{B}}{\mu^c}\right)^*\cdot\nabla\times\mathbf{b}\\ &+\int_{\Sigma_\mu}\left\{\frac{1}{\sigma R_m}\mathbf{j}^s+\tilde{\mathbf{u}}\times\mathbf{B}^*\right\}\cdot(\mathbf{b}_1\times\mathbf{n}_1^c+\mathbf{b}_2\times\mathbf{n}_2^c)\\ &+\int_{\Omega_c}\left(\frac{1}{\sigma R_m}\mathbf{j}^s+\tilde{\mathbf{u}}\times\mathbf{B}^*\right)\cdot\nabla\times\mathbf{b}\\ &+\int_{\Sigma}\left(\frac{1}{\sigma R_m}\mathbf{j}^s+\tilde{\mathbf{u}}\times\mathbf{B}^*\right)\cdot(\mathbf{b}\times\mathbf{n}^c+\nabla\varphi\times\mathbf{n}^v)\\ &+\int_{\Gamma_{c,n}}(\mathbf{a}\times\mathbf{n})\cdot(\mathbf{b}\times\mathbf{n}) + \int_{\Gamma_v}(\mathbf{a}\times\mathbf{n})\cdot(\nabla\varphi\times\mathbf{n}),+\overline{\mathcal{H}}_n(\mathbf{b}).\end{aligned}$$

where the linear form $\overline{\mathcal{H}}_n(\mathbf{b})$ is defined as

$$\overline{\mathcal{H}}_n(\mathbf{b}) = \int_{\Gamma_{c,d}}\left(\frac{1}{\sigma R_m}\mathbf{j}^s+\tilde{\mathbf{u}}\times\mathbf{B}^*\right)\cdot(\mathbf{b}\times\mathbf{n}^c) + \int_{\Gamma_{c,d}}\beta_4\left(\sum_{F\in\Gamma_{c,d}} h_F^{-1}\int_F\left(\frac{\mathbf{B}_d^c}{\overline{\overline{\mu^c}}}\times\mathbf{n}^c\right)\cdot(\mathbf{b}\times\mathbf{n}^c)\right),$$

whose last term balances the bilinear form $\overline{\mathcal{E}}(\mathbf{B},\mathbf{b})$.

We now make some important observations of scheme (5.2):

- Even though scheme (5.2) can handle the case $\mu=\mu(\mathbf{x},t)$, we have assumed μ is at least continuous in the θ component; namely, jump conditions on Σ_μ,

and on Σ cannot be handled for θ. Because in Fourier space, we have lost local information in this component. However, jumps conditions can be still handled when depend only in (r, z).

- In practice, those terms in $\overline{\mathcal{R}}_n(\mathbf{b}, \varphi)$ that have $\left(\frac{\mathbf{B}}{\mu^c}\right)^*$ or $\tilde{\mathbf{u}} \times \mathbf{B}^*$ are computed in real space, and then transfered into Fourier space.

- Although the continuous weak formulation (5.2) is a Petrov-Galerkin one, the discrete weak formulation (3.16) is Galerkin, because we previously set $\mathbf{X}_h^{\mathbf{B}} = \mathbf{X}_h^{\mathbf{H}}$.

5.4 Convergence Tests

The scheme (5.10) has been implemented in the code `SFEMaNS`, and in this subsection we test our implementation using manufactured solutions. Although scheme (5.10) computes $\mathbf{B}^c$, using $\mathbf{B}^c = \mu^c \mathbf{H}^c$ we can compute $\mathbf{H}^c$ as well. All convergence tables reported in this subsection are reported using $\mathbf{H}^c$.

5.4.1 Maxwell Equations with Jumps

For this convergence test, we use the same setting and analytical solution as in subsection 3.6.2. Denoting by $\mathbf{H}_h$ the approximate magnetic field, we report in table 5.1 the relative errors, and the computed order of convergence (COC). For this test $\mathbb{P}_2$, and $\mathbb{P}_1$ Lagrange elements are used for $\mathbf{H}_h^c$ and p_h^c, respectively. The convergence rate observed in table 5.1 agrees with the optimal one expected using scheme (3.16). We recall that in table 3.2 of subsection 3.6.2 superconvergence is observed. Nevertheless, the numerical errors in table 5.1 have a better accuracy.

h	$\|\nabla\cdot(\mu\mathbf{H})_h\|_{L^2}$	COC	$\|\nabla\times(\mathbf{H}-\mathbf{H}_h)\|_{L^2}$	COC	$\|\mathbf{H}-\mathbf{H}_h\|_{L^2}$	COC
0.2	6.9259E-02	—	3.3573E-01	—	2.2607E-01	—
0.1	1.3491E-04	9.00	2.3323E-04	10.49	5.3161E-05	12.05
0.05	5.0534E-05	1.42	4.9039E-05	2.25	6.1933E-06	3.10
0.025	1.1779E-05	2.10	9.7326E-06	2.33	6.8326E-07	3.18
0.0125	3.0474E-06	1.95	2.0294E-06	2.26	9.9443E-08	2.78

Table 5.1: Numerical errors computed when μ is axisymmetric, and it has jumps using scheme (5.10).

5.4.2 Maxwell Equations with Vacuum and μ Variable in θ

For this particular test we set $\mu^c = \mu^c(r,\theta,z)$, but μ^c is not allowed to have jumps in Ω_c, so $\Sigma_\mu = \emptyset$. We construct an analytical solution for the system (3.8) defining first the magnetic field $\mathbf{H}$ and the magnetic permeablity μ by

$$\mathbf{H} = \begin{cases} \mathbf{H}^c & \text{in} \quad \Omega_c \\ \nabla\psi & \text{in} \quad \Omega_v \end{cases}, \quad \text{and} \quad \mu = \begin{cases} \mu^c & \text{in} \quad \Omega_c \\ 1 & \text{in} \quad \Omega_v \end{cases}. \tag{5.11}$$

We set $\Omega_c = \{(r,\theta,z) \in R^3 : (r,\theta,z) \in [0,1]\times[0,2\pi)\times[-1,1]\}$, and $\Omega_v = \{(r,\theta,z) \in R^3 : r^2+z^2 = 10^2, \theta \in [0,2\pi)\} \setminus \Omega_c$. Now, let us set

$$\mathbf{H} = \frac{1}{\mu^c}\nabla\psi, \tag{5.12}$$

where $\psi = \psi(r,z) = J_0(r)\cosh(z)$. Observe that $\psi(r,z)$ is the same as the one

defined in (3.22) which satisfies the Laplace equation in cylindrical coordinates

$$\partial_{rr}\psi + \frac{1}{r}\partial_r\psi + \partial_{zz}\psi = 0.$$

If we also set $\mathbf{j} = \nabla \times \mathbf{H}$, $\mathbf{u} = 0$, then $\mathbf{E} = \mathbf{0}$, and $\mathbf{H}$ satisfies the Maxwell equations (3.8). Now, let us define

$$\mu = \mu(r, \theta, z) = \frac{1}{f(r, z)\cos(m\theta) + 1}, \tag{5.13}$$

where

$$f(r, z) = b \cdot r^3 \cdot (1 - r)^3 \cdot (z^2 - 1)^3,$$

and b is a non-negative parameter which determines the variation of μ. Observe that $\mu = 1$ at $(r, z) = (1, \pm 1)$, then $\mu = 1$ at Ω_v. So we set $\mu^c = \mu$, because by using (5.11) allows us to have vacuum, and μ^c has no jumps on Ω as required. Also notice that $f(r, z) \leq 0$ for $(r, \theta, z) \in \Omega_c$ and

$$\sup_{\Omega^c} |f(r, z)| = |f|_{\max} = \frac{b}{2^6}, \quad \inf_{\Omega^c} |f(r, z)| = |f|_{\min} = 0.$$

Then if $m \neq 0$, then

$$\begin{aligned} &\mu^c_{\min} = \frac{1}{1 + |f|_{\max}}, && \mu^c_{\max} = \frac{1}{1 - |f|_{\max}}, \\ &r_\mu = \frac{\mu_{\max}}{\mu_{\min}} = \frac{1 + |f|_{\max}}{1 - |f|_{\max}}, \quad \text{and} && b = 2^6 \left(\frac{r_\mu - 1}{r_\mu + 1} \right). \end{aligned} \tag{5.14}$$

Denoting by $\mathbf{H}_h$ the approximate magnetic field, we report in tables 5.2a and 5.2b the relative errors using the code `SFEMaNS`. These tables also show the computed order

of convergence (COC). For this test $\mathbb{P}_2, \mathbb{P}_2$ and $\mathbb{P}_1$ Lagrange elements are employed for $\mathbf{H}_h^c, \phi_h$ and p_h^c, respectively. We set a variation ratio of $r_\mu = 50$, and $m = 4$ in (5.13). Moreover, we have chosen

$$\overline{\mu} = \overline{\mu}(r, z) = \frac{1}{1 + |f(r, z)|},$$

which satisfies conditions (5.7)-(5.9). Solution (5.12) is in Fourier space with modes $m = 0, 4$, but our experiments run using $M = 8$ as the total of complex Fourier modes, because explicit convolutions coming from the term (5.5) are performed in real space.

h	$\|\nabla\cdot(\mu\mathbf{H})_h\|_{L^2}$	COC	$\|\nabla\times(\mathbf{H}-\mathbf{H}_h)\|_{L^2}$	COC
0.2	2.0159E-02	—	1.2939E-02	—
0.1	9.1712E-03	1.14	2.7943E-03	2.21
0.05	3.5180E-03	1.38	5.5778E-04	2.32
0.025	1.2798E-03	1.46	1.0640E-04	2.39
0.0125	4.8781E-04	1.39	2.3761E-05	2.16

(a)

h	$\|\mathbf{H}-\mathbf{H}_h\|_{L^2}$	COC	$\|\phi-\phi_h\|_{H^1}$	COC
0.2	4.4144E-03	—	3.1675E-04	—
0.1	1.1585E-03	1.93	7.0282E-05	2.17
0.05	1.8991E-04	2.61	1.1526E-05	2.61
0.025	2.7246E-05	2.80	1.7517E-06	2.72
0.0125	3.8001E-06	2.84	2.7838E-07	2.65

(b)

Table 5.2: Numerical errors computed when vacuum is nonempty, and μ is non-axisymmetric using scheme (5.10).

5.4.3 Maxwell Equations with Jumps and μ Variable in θ

We set $\mu^c = \mu^c(r,\theta,z)$, $\Omega_c = \emptyset$, and we allow μ^c to have jumps. We first begin setting $\mathbf{u} = 0$, $\mathbf{E} = 0$, and $\Omega_c = \Omega_{c,1} \cup \Omega_{c,2}$, where

$$\Omega_{c,1} = \{(r,\theta,z) \in R^3 : (r,\theta,z) \in [0,1] \times [0,2\pi) \times [1/4,1]\},$$

and

$$\Omega_{c,2} = \{(r,\theta,z) \in R^3 : (r,\theta,z) \in [1,2] \times [0,2\pi) \times [1/4,1]\}.$$

Let $\lambda_\mu = 10$ and set

$$\mathbf{H}^c = \begin{bmatrix} H_r \\ 0 \\ H_z \end{bmatrix}, \tag{5.15}$$

where

$$H_r = \begin{cases} H_{1,r} = r(1 + s(r,z) \cdot \cos(m\theta)) & \text{in} \quad \Omega_{c,1}, \\ H_{2,r} = \frac{rz^3(3r+2)}{3z^2r+2z^2+2\lambda_\mu} & \text{in} \quad \Omega_{c,2}, \end{cases}$$

and

$$H_z = -2z(1 + s(r,z) \cdot \cos(m\theta)).$$

We now define the magnetic permeability as

$$\mu^c = \mu^c(r,\theta,z) = \begin{cases} \mu_1 = \frac{1}{1+s(r,z)\cdot\cos(m\theta)} & \text{in} \quad \Omega_{c,1}, \\ \mu_2 = \mu_1 \cdot (1 + \frac{\lambda_\mu}{z}) & \text{in} \quad \Omega_{c,2}, \end{cases}$$

where,

$$s(r,z) = b \cdot (r \cdot (r-1) \cdot (r-2) \cdot (z - \frac{1}{4}) \cdot (z-1))^3,$$

and b is a non-negative parameter which determines the variation of μ_1. For instance, observe that

$$\sup_{\Omega^c} |s(r,z)| = |s|_{\max} \approx 1.6 \times 10^{-4} \cdot b, \text{ and } \quad \inf_{\Omega^c} |s(r,z)| = 0.$$

Then if $m \neq 0$,

$$\begin{aligned} \mu_{1,\min} &= \frac{1}{1+|s|_{\max}}, & \mu_{1,\max} &= \frac{1}{1-|s|_{\max}}, \\ r_{\mu_1} &= \frac{\mu_{1,\max}}{\mu_{1,\min}} = \frac{1+|s|_{\max}}{1-|s|_{\max}}, \quad \text{and} & b &= \frac{1}{1.6\times 10^{-4}} \left(\frac{r_\mu - 1}{r_\mu + 1} \right). \end{aligned} \tag{5.16}$$

Denoting by $\mathbf{H}_h$ the approximate magnetic field, we report in table 5.3 the relative errors using the code `SFEMaNS`. These tables also show the computed order of convergence (COC). For this test $\mathbb{P}_2$ and $\mathbb{P}_1$ Lagrange elements are employed for $\mathbf{H}_h^c$ and p_h^c, respectively. We set a variation ratio of $r_{\mu_1} = 50$, and $m = 3$ in (5.16). Moreover, we have chosen

$$\overline{\mu} = \overline{\mu}(r,z) = \begin{cases} \overline{\mu}_1(r,z) & \text{in} \quad \Omega_{c,1}, \\ \\ \overline{\mu}_2(r,z) & \text{in} \quad \Omega_{c,2}, \end{cases}$$

where

$$\overline{\mu}_1(r,z) = \frac{1}{1+|s(r,z)|}, \quad \text{and} \quad \overline{\mu}_2(r,z) = \frac{1}{1+|s(r,z)|} \cdot \left(1 + \frac{\lambda_\mu}{z} \right).$$

With these choices conditions (5.7)-(5.9) are satisfied. Solution (5.15) is in Fourier space with mode $m = 0, 3$, but our experiments run using $M = 8$ as the total of complex Fourier modes, because explicit convolutions coming from the term (5.5) are performed in real space.

h	$\|\nabla\cdot(\mu\mathbf{H})_h\|_{L^2}$	COC	$\|\nabla\times(\mathbf{H}-\mathbf{H}_h)\|_{L^2}$	COC	$\|\mathbf{H}-\mathbf{H}_h\|_{L^2}$	COC
0.2	6.7047E-02	—	4.0861E-02	—	2.7662E-02	—
0.1	2.4419E-02	1.46	1.0172E-02	2.01	1.2171E-02	1.18
0.05	8.2856E-03	1.56	2.1516E-03	2.24	2.5106E-03	2.28
0.025	2.7117E-03	1.61	4.4641E-04	2.27	3.6161E-04	2.80
0.0125	8.7132E-04	1.64	9.1020E-05	2.29	4.8304E-05	2.90

Table 5.3: Numerical errors computed when μ has jumps and is non-axisymmetric using scheme (5.10).

5.5 The Kinematic Dynamo Problem

We now turn our attention to the main application we have in mind, namely the dynamo action. When the velocity $\tilde{\mathbf{u}}$ is given, the problem of solving Maxwell equations (5.1) is called the kinematic dynamo problem. Validation of the kinematic code is a prerequisite for the full nonlinear dynamo problem where the Navier-Stokes equations (2.14) including the Lorentz force are also solved. We consider only the kinematic situation where the velocity field $\tilde{\mathbf{u}}$ is constant, and the magnetic permeability μ is time independent, i.e. $\mu = \mu(\mathbf{x})$. In doing so the kinematic dynamo problem reduces to an eigenvalue problem; namely, assuming $\Omega_v = \emptyset$, the solution of (5.1) can be written as

$$\widetilde{\mathbf{B}} = \sum_{j}^{\infty} c_j \widetilde{\mathbf{b}}_j e^{\lambda_j t},$$

where c_j are constants, and $(\widetilde{\mathbf{b}}_j, \lambda_j)$ is the j-th eigenpair of the problem

$$\lambda\widetilde{\mathbf{b}} = -\nabla\times\left(R_{\mathrm{m}}^{-1}\sigma^{-1}\left(\nabla\times\left(\frac{\widetilde{\mathbf{b}}}{\mu}\right)\right) - \tilde{\mathbf{u}}\times\widetilde{\mathbf{b}}\right), \tag{5.17}$$

satisfying the jump conditions on Σ_μ and suitable boundary conditions. The eigenvalues can be complex numbers, since the right hand side of the eigenvalue problem (5.17) is not symmetric. Then dynamo action is said to occur when a growing solution $\widetilde{\mathbf{B}}$ exists, and this happens when there exists j' such that $\mathrm{Re}(\lambda_{j'}) > 0$; the critical magnetic Reynolds number R_m^c is the value corresponding to $\mathrm{Re}(\lambda_j) = 0, \quad \forall j$. A random initial condition $\mathbf{B}_0$ will have some component of the growing modes, and these dominate at large time. These kinematic dynamos go on growing for ever. In reality, the field $\mathbf{B}$ affects the flow through the Lorentz force in the equation of motion, and changes $\mathbf{u}$ so the dynamo stops growing. This is the nonlinear saturation process, see [15, 17, 41] for details.

5.6 Numerical Simulation of Kinematic Dynamos

In this subsection[1] we show results using scheme (5.10) and `SFEMaNS` for the kinematic dynamo problem inside a half-cylinder. So the problem is to find numerically a positive and a negative eigenvalues of (5.1) to have an estimation of R_m^c. It is common practice to compute R_m^c by linear extrapolation. In order to compare our results we also present numerical experiments done by the code `DOLMEN`, which uses 3D Whitney finite elements. See Zaidi *et al.* [67] for more details about the method and numerical results. All figures in this subsection related to `DOLMEN` are courtesy of C. Nore and F. Bouillault.

The computational domain is a cylindrical vessel of radius $R_c = 1$ and height $H = 0.7$ ($0 \leq r \leq 1$, $-0.2 \leq z \leq 0.5$), and the impeller driving the flow consists of a disk equipped with eight blades. The disk is a cylinder of radius $R_d = 0.54$ and height $l_d = 0.06$ ($-0.2 \leq z \leq -0.14$). The height of the blades is $l_b = 0.14$, their thickness is $e_b = 0.02$, the angle at the rim is $\alpha = 24^o$, and the generator radius is

[1]Part of the data reported in this subsection is reprinted with permission from [44]. Copyright 2015 by EDP Sciences.

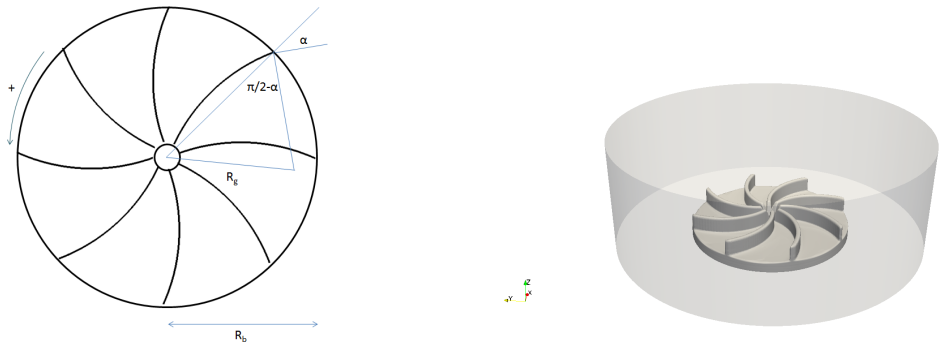

(a) Blade and disk geometry. (b) Impeller geometry.

Figure 5.1: Half von Kármán set-up: (a) blade and disk geometry; (b) impeller geometry. Both images reprinted with permission from [44]. Copyright 2015 by EDP Sciences.

$R_g = 0.66$, see figure 5.1 (a). This geometry is shown in figure 5.1(b).

The velocity field, $\mathbf{V}_F = (u_r, u_\theta^F, u_z)$, in the fluid $(0 \leq r \leq 1,\, 0 \leq z \leq 0.5)$ is modeled as follows:

$$\begin{aligned} u_r &= (\pi/2L)\cos(\pi z/L)\, r(1-r)^2(1+2r), \\ u_\theta^F &= 4\epsilon r(1-r^5)\sin\left(\pi(L-z)/2L\right), \\ u_z &= -(1-r)(1+r-5r^2)\sin\left(\pi z/L\right), \end{aligned} \tag{5.18}$$

where $L = 0.5$ denotes the distance between the top lid of the computational box (i.e., equatorial plane of the VKS container) and the top of the blades, and ϵ measures the ratio between the toroidal and the poloidal components of the velocity (here, $\epsilon = 0.7259$ as in [40]). The velocity field in the impeller region $(0 \leq r \leq 1,\, -0.2 \leq z \leq 0)$ is assumed to be a solid-body rotation:

$$u_\theta^I = r. \tag{5.19}$$

The component u_θ is interpolated between the fluid region and the impeller zone using $u_\theta = u_\theta^F \frac{1+\tanh(z/z_{\text{del}})}{2} + u_\theta^I \frac{1-\tanh(z/z_{\text{del}})}{2}$, with $z_{\text{del}} = 0.05$. The vector field defined above is denoted $\mathbf{V}_0$ and its maximum is $U_{\max} = 1.66$ in Euclidean norm. All the computations presented in this subsection are performed in the reference frame of the impeller, i.e., the velocity field in (3.8) is defined to be $\tilde{\mathbf{u}} := \mathbf{V}_0 - r\mathbf{e}_\theta$. We denote by μ_f, μ_d, and μ_b the magnetic permeability of the fluid, disk and blades, respectively. In all these experiments we set $\mu_f = 1$.

We set $\Omega_v = \emptyset$, so we impose the Dirichlet boundary condition $\frac{\mathbf{B}}{\mu^c} \times \mathbf{n} = 0$ at the bottom and at the sides of the half-cylinder. Two sets of boundary conditions are set at the top of the half-cylinder to amplify the Fourier modes $m = 1$ and $m = 0$. These conditions are described below. Moreover, all the results reported using `SFEMaNS` are done with $M = 128$ of total Fourier modes, $\mathbb{P}_2$ approximation for $\mathbf{B}_h^c$, and $\mathbb{P}_1$ approximation for p_h. The trace of the impeller approximated with `SFEMaNS` is shown in 5.2(a). The meridian mesh is non uniform with a minimum mesh-size $h = 0.0075$ and a maximum mesh-size $h = 0.02$. The trace of the tetrahedral mesh of the impeller and the total mesh used in `DOLMEN` are shown on figure 5.2(b). The mesh is non uniform with a mesh-size $h = e_b/8 = 0.0025$ in each blade and $h = 1/15$ at the top lid $z = 0.5$.

5.6.1 Using Neumann Boundary Condition at the Top

In this numerical simulation we set the condition $\mathbf{B} \cdot \mathbf{n} = 0$ at the top. We put as initial condition the field $\mathbf{B}_0 = \mathbf{e}_x$ plus some random noise. The magnetic Reynolds numbers $R_{\text{m}} = 50$ and $R_{\text{m}} = 70$ are considered. For `SFEMaNS`, we have run $\mu_d = \mu_b = 5$ and $\mu_d = \mu_b = 50$. The computed tresholds for these cases are $R_{\text{m}}^c \approx 58.4$ and $R_{\text{m}}^c \approx 58$, respectively. The code `DOLMEN` cannot handle big values of μ, so the only considered case is $\mu_b = \mu_d = 5$, which gives a computed

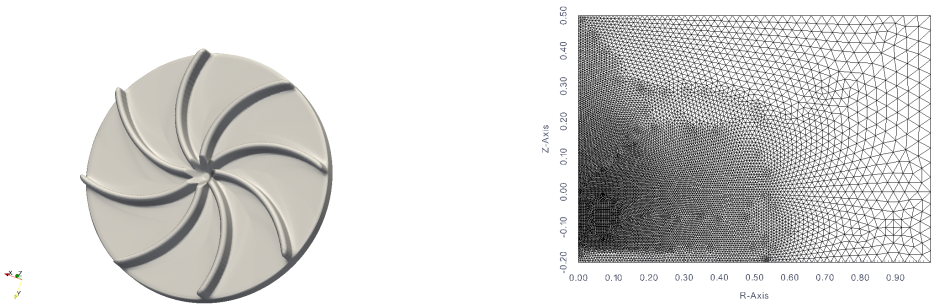

(a) `SFEMaNS`.

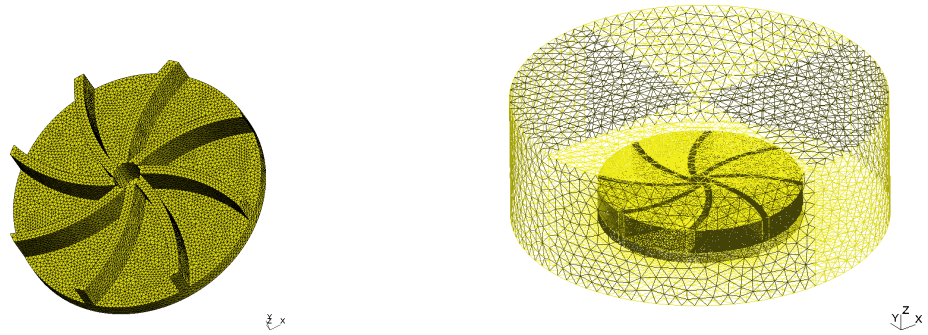

(b) `DOLMEN`.

Figure 5.2: Discretization of the geometry involved using the half bladed von Kármán set-up: (a) impeller and meridian mesh used in `SFEMaNS` for the ; (b) trace of the tetrahedral mesh of the impeller and total mesh used in `DOLMEN`. Both images in (b) are courtesy of C. Nore and F. Bouillault.

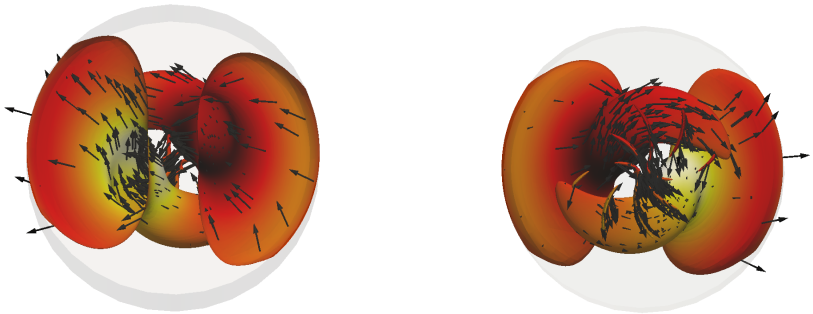

(a) SFEMaNS.

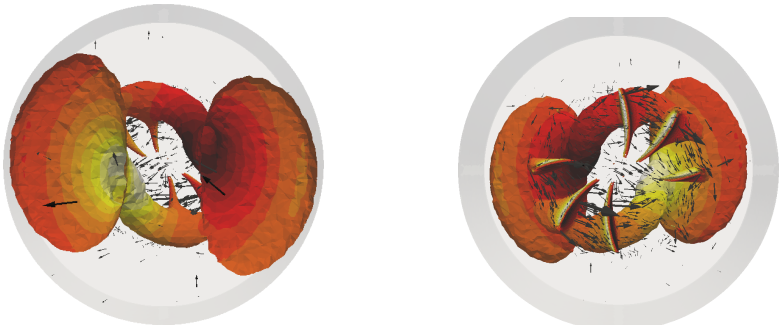

(b) DOLMEN.

Figure 5.3: Structure of the rotating magnetic field generated in a half von Kármán set-up in the bladed configuration (at $R_{\mathrm{m}} = 70$ with $\mu_b = \mu_d = 5$) represented by vectors and the isosurface $\|\mathbf{B}\|^2$ (5% of maximum value) colored by the vertical component (minimum value in white and maximum value in dark/red). Note the $m = 1$ structure of the magnetic field in the bulk and the footprint on the 8 blades. Both images in (b) are courtesy of C. Nore and F. Bouillault.

treshold $R_{\mathrm{m}}^c \approx 61$. The discrepancy between the two codes can have various sources: the blades are not exactly the same and the approximation algorithms are totally different. Nevertheless, the spatial distribution of the magnetic field is very similar for both codes as shown on figure 5.3 where is clearly seen that mode $m = 1$ dominates.

5.6.2 Using Dirichlet Boundary Condition at the Top

Here we set $\frac{\mathbf{B}}{\mu} \times \mathbf{n} = 0$ at the top, and set the axisymmetric field $\mathbf{B}_0 = \mathbf{e}_z$ as initial condition plus some random noise. Setting $\mu_b = \mu_d = 5$, we measure the leading eigenvalues for the magnetic Reynolds numbers $R_{\mathrm{m}} \in [90, 750]$ (see figure 5.6a). The

modes $m = 0$ and $m = 2$ are the leading ones. `DOLMEN` and `SFEMaNS` have similar growth rates for the mode $m = 0$ at $R_\mathrm{m} = 90$ and $R_\mathrm{m} = 550$. We have estimated the thresholds for these modes by interpolation (or extrapolation) on the growth rates. The dynamo threshold is $R_\mathrm{mc} \approx 1300$ for mode $m = 0$ and $R_\mathrm{mc} \approx 550$ for mode $m = 2$.

The leading eigenvector at $R_\mathrm{m} = 750$ is mode $m = 2$ and has a positive growth-rate; the spatial distribution of this mode is shown in figure 5.6b. It is a bulk eigen-mode with four helical structures. The simulations at all investigated R_m show that the leading mode $m = 0$ has a negative growth-rate; the spatial distribution of the corresponding eigenvector is shown in figures 5.4 and 5.5.

5.6.3 Conclusion

In this section we have presented two different kinematic dynamos of the half VKS setting using a given stationary analytical velocity $\tilde{\mathbf{u}}$. Using the new scheme (5.10) implemented in the code `SFEMaNS`, we have found a dynamo in both cases, and validated our numerical results against the 3D code `DOLMEN`. However, in none of these cases we have observed an axisymmetric dynamo. So we conclude that the velocity $\tilde{\mathbf{u}}$ is incapable of generating dynamos similar to the one observed in the real VKS experiment. Then a full MHD simulation is still necessary, and this has been successfully achieved in this thesis, and it is reported in the next section.

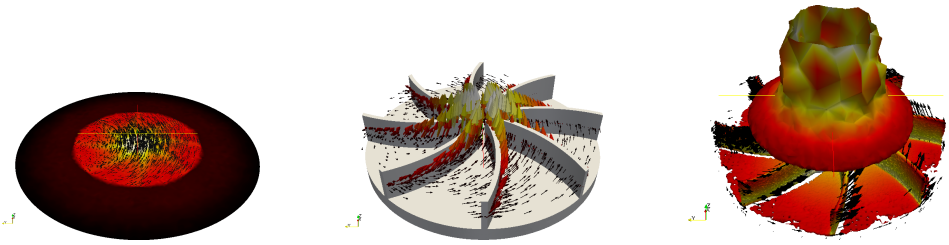

(a) Disk region. (b) Blade region. (c) Bulk region.

Figure 5.4: Structure of the leading eigenvector using `DOLMEN` for mode $m = 0$ (stable at $R_\mathrm{m} = 90$ with $\mu_b = \mu_d = 5$) represented by vectors shown (a) in the disk, (b) in the impeller region and (c) in the bulk region. In the latter, are plotted vectors and the isosurface $\|\mathbf{B}\|^2$ (1% of maximum value–colored by the vertical component with minimum value in black and maximum value in white). All images in this figure are courtesy of C. Nore and F. Bouillault.

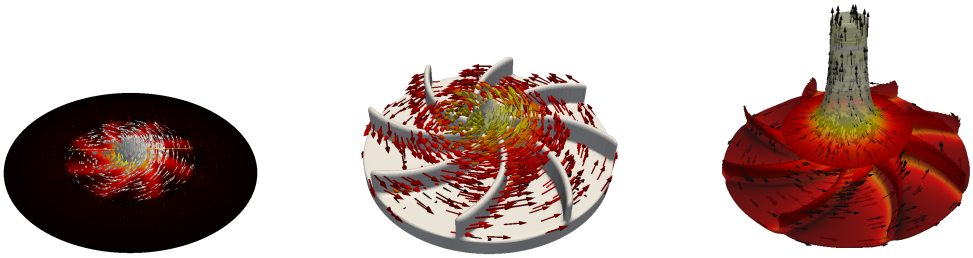

(a) Disk region. (b) Blade region. (c) Bulk region.

Figure 5.5: Same as fig. 5.4 but using `SFEMaNS` at $R_\mathrm{m} = 550$ with $\mu_b = \mu_d = 5$ and the isosurface $\|\mathbf{B}\|^2$ is 0.5% of maximum value, colored by the vertical component with minimum value in brown and maximum value in white. Figure (c) is reprinted with permission from [44]. Copyright 2015 by EDP Sciences.

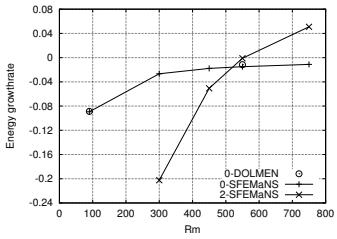

(a) Growth rates for modes $m = 0$ and $m = 2$.

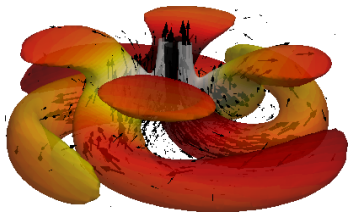

(b) Leading eigenvector for mode $m = 2$ (unstable).

Figure 5.6: Kinematic dynamo in a half von Kármán set-up with the velocity field $\mathbf{V}_0$ and the bladed configuration with $\mu_b = \mu_d = 5$: (a) Energy growth rate of modes $m = 0$ and $m = 2$ for $R_\mathrm{m} \in [90, 750]$ (`DOLMEN` results taken from [67]); (b) structure of the leading eigenvector using `SFEMaNS` at $R_\mathrm{m} = 750$ for mode $m = 2$ represented by the isosurface $\|\mathbf{B}\|^2$ (10% of maximum value, colored by the vertical component with minimum value in dark/red and maximum value in white) and vectors shown in the disk, in the impeller region and in the bulk region. Figure (b) is reprinted with permission from [44]. Copyright 2015 by EDP Sciences.

6. NUMERICAL SIMULATION OF THE VKS-MHD DYNAMO EXPERIMENT

In this section we report full MHD numerical computations of the VKS dynamo experiment. We begin discussing the discretization of Navier-Stokes equations, and how the code `SFEMaNS` has been extended to handle non-axisymmetric moving obstacles such as moving blades. We then peform hydrodynamic and MHD simulations for the VKS at moderated low Reynolds numbers. Doing so we have found that for high values of magnetic permeability μ an axisymmetric magnetic field is predominant. This coincides with the real VKS experiment.

6.1 MHD Equations using $\mathbf{B}$

We recall that in the beginning of section 5 we have reformulated the Maxwell equations using the magnetic induction field $\mathbf{B}$ instead of $\mathbf{H}$. The main reason has been explained in subsection 3.7. So for convenience we rewrite the complete MHD system (3.7)-(3.8) in terms of $\mathbf{B}$ as follows:

$$\begin{cases} \partial_t \mathbf{u} + (\mathbf{u}\cdot\nabla)\mathbf{u} - R_{\mathrm{e}}^{-1}\Delta\mathbf{u} + \nabla p = \left(\nabla\times\left(\frac{\mathbf{B}}{\mu^c}\right)\right)\times\mathbf{B} \quad \text{in} \quad \Omega_{cf}, \\ \nabla\cdot\mathbf{u} = 0 \quad \text{in} \quad \Omega_{cf}, \\ \mathbf{u}|_{t=0} = \mathbf{u}_0 \quad \text{in} \quad \Omega_{cf}, \quad \mathbf{u}|_{\Gamma_f} = \mathbf{d}, \end{cases} \tag{6.1}$$

$$
\begin{cases}
\partial_t \mathbf{B}^c = -\nabla\times(R_{\mathrm{m}}^{-1}\sigma^{-1}(\nabla\times(\frac{\mathbf{B}^c}{\mu^c}) - \mathbf{j}^s) - \tilde{\mathbf{u}}\times\mathbf{B}^c) & \text{in every} \quad \Omega_{ci}, \quad i \in \overline{1,N}, \\
\mu^v \partial_t \Delta\phi = 0, & \text{in} \quad \Omega_v, \\
(R_{\mathrm{m}}^{-1}\sigma^{-1}(\nabla\times(\frac{\mathbf{B}^c}{\mu^c}) - \mathbf{j}^s) - \tilde{\mathbf{u}}\times\mathbf{B}^c)\times\mathbf{n}^c = \mathbf{a} & \text{on} \quad \Gamma_{c,n}, \\
\frac{\mathbf{B}^c}{\mu^c}\times\mathbf{n} = \frac{\mathbf{B}_d^c}{\mu^c}\times\mathbf{n} & \text{on} \quad \Gamma_{c,d}, \\
\mu^v \partial_{\mathbf{n}^v}\partial_t\phi = -\mathbf{n}^v\cdot\nabla\times(\mathbf{n}^v\times\mathbf{a}), & \text{on} \quad \Gamma_v, \\
\frac{\mathbf{B}_1^c}{\mu_1^c}\times\mathbf{n}_1^c + \frac{\mathbf{B}_2^c}{\mu_2^c}\times\mathbf{n}_2^c = 0 & \text{on} \quad \Sigma_\mu, \\
\mathbf{B}_1^c\cdot\mathbf{n}_1^c + \mathbf{B}_2^c\cdot\mathbf{n}_2^c = 0 & \text{on} \quad \Sigma_\mu, \\
\frac{\mathbf{B}^c}{\mu^c}\times\mathbf{n}^c + \nabla\phi\times\mathbf{n}^v = 0 & \text{on} \quad \Sigma, \\
\mathbf{B}^c\cdot\mathbf{n}^c + \mu^v\nabla\phi\cdot\mathbf{n}^v = 0 & \text{on} \quad \Sigma, \\
\mathbf{B}|_{t=0} = \mathbf{B}_0, \quad \phi|_{t=0} = \phi_0 & \text{in} \quad \Omega.
\end{cases}
\tag{6.2}
$$

The Maxwell equations (6.2) have been numerically treated previously, whereas discretization of (6.1) is discussed next.

6.2 Discretization of the Navier-Stokes Equations

In this subsection we begin describing the original algorithm implemented in `SFEMaNS` to solve the Navier-Stokes equations (6.1). Its details are reported in Guermond *et al.* [30]. However, this only works for axysimmetric obstacles, since we have assumed in subsection 3.5.1 that the conducting fluid domain Ω_{cf} is axysimmetric. To overcome this restriction, an implementation of the pseudo-penalization method introduced by Pasquetti *et al.* [45] has been done in `SFEMaNS`. Such method is described in subsection 6.2.3.

6.2.1 Time Stepping Scheme

We first describe the time stepping scheme to solve (6.1), which is a pressure correction based method in rotational form, see Guermond and Shen [32] for details. The scheme consists of seeking the prediction $\widetilde{\mathbf{u}}$ of the velocity $\mathbf{u}$ by solving first

$$\frac{3\widetilde{\mathbf{u}}^{n+1} - 4\mathbf{u}^n + \mathbf{u}^{n-1}}{2\Delta t} - \frac{1}{R_\mathrm{e}}\Delta\widetilde{\mathbf{u}}^{n+1} + \nabla p^n = \mathbf{f}^{n+1}, \tag{6.3}$$

where we have neglected the nonlinear and the Lorentz force terms for the time being. To satisfy the incompressible condition, we determine $\mathbf{u}$ such that

$$\begin{cases} \frac{3}{2\Delta t}\mathbf{u}^{n+1} - \frac{3}{2\Delta t}\widetilde{\mathbf{u}}^{n+1} + \nabla\left(p^{n+1} - p^n + \frac{1}{R_\mathrm{e}}\nabla{\cdot}\widetilde{\mathbf{u}}^{n+1}\right) = 0, \\ \nabla{\cdot}\mathbf{u}^{n+1} = 0. \end{cases} \tag{6.4}$$

In practice, the code `SFEMaNS` computes a scalar ψ^{n+1} such that

$$\Delta\psi^{n+1} = -\frac{3}{2\Delta t}\nabla{\cdot}\widetilde{\mathbf{u}}^{n+1}. \tag{6.5}$$

Doing so, the projected velocity $\mathbf{u}$ can be eliminated from (6.3) and (6.4) because

$$\mathbf{u}^{n+1} = \widetilde{\mathbf{u}}^{n+1} - \frac{2\Delta t}{3}\nabla\psi^{n+1}. \tag{6.6}$$

6.2.2 Finite Element Discretization

Now using the same notation as in subsection 3.5.1, we describe the space discretization in `SFEMaNS`. A mixed Taylor-Hood $\mathbb{P}_2/\mathbb{P}_1$ finite element is used, see [28]. And for the weak formulation we define the finite-dimensional real-valued vector

spaces:

$$\mathbf{V}_h^{2D} := \{\mathbf{v}_h|_{\Omega_{ci}} \in \boldsymbol{\mathcal{C}}^0(\overline{\Omega_{ci}}), \forall i = 1, \ldots, N, \mathbf{v}_h(T_K^{-1})|_K \in \mathbb{P}_2^6,\ \forall K \in \mathcal{F}_h^{cf}\}, \tag{6.7}$$

$$M_h^{2D} := \{q_h \in \mathcal{C}^0(\overline{\Omega_v});\, q_h(T_K^{-1})|_K \in \mathbb{P}_1^2,\ \forall K \in \mathcal{F}_h^{cf}\}. \tag{6.8}$$

At a given time the velocity and the pressure fields are approximated by:

$$\mathbf{V}_h := \{\mathbf{v} = \sum_{m=-M}^{M} \mathbf{v}_h^m(r,z)e^{\mathrm{i}m\theta};\, \mathbf{v}_h^m \in \mathbf{V}_h^{2D},\ \overline{\mathbf{v}_h^m} = \mathbf{v}_h^{-m},\ k \in \overline{0, M}\}, \tag{6.9}$$

$$M_h := \{q_h = \sum_{m=-M}^{M} q_h^m(r,z)e^{\mathrm{i}m\theta};\, q_h^m \in q_h^{\phi,2D},\ \overline{q_h^m} = q_h^{-m},\ m \in \overline{0, M}\}. \tag{6.10}$$

Also let us denote $\mathbf{V}_{h,0}$ as the subspace of $\mathbf{V}_h$ composed of vector fields that are zero on Γ_f. After proper initialization at t^0 and t^1, we define,

$$\mathbf{u}^* = 2\mathbf{u}^n - \mathbf{u}^{n-1}, \quad \text{and} \quad D\mathbf{u}^{n+1} := \frac{1}{2}(3\mathbf{u}^{n+1} - 4\mathbf{u}^n + \mathbf{u}^{n-1}).$$

Then the weak formulation of (6.1) is to solve for $\mathbf{u}^{n+1} \in \mathbf{V}_h$ so that $\mathbf{u}^{n+1}|_{\Gamma_f} = \mathbf{d}^{n+1}$ is an approximation of boundary data $\mathbf{d}(t^{n+1})$ and the following holds for all $\mathbf{v} \in \mathbf{V}_{h,0}$:

$$\begin{aligned}\int_{\Omega_{cf}} \frac{D\mathbf{u}^{n+1}}{\Delta t} \cdot \mathbf{v} + \frac{1}{R_\mathrm{e}} \nabla\mathbf{u}^{n+1} : \nabla\mathbf{v}^{n+1} = &- \int_{\Omega_{cf}} \mathbf{v} \cdot \nabla \left(p^n + \frac{4}{3}\psi^n - \frac{1}{3}\psi^{n-1} \right) \\ &+ \int_{\Omega_{cf}} \mathbf{v} \cdot \left(\left(\nabla \times \frac{\mathbf{B}^*}{\mu} \right) \times \mathbf{B}^* - (\nabla \times \mathbf{u}^*) \times \mathbf{u}^* \right).\end{aligned} \tag{6.11}$$

A pressure correction is computed by solving ψ^{n+1} and ζ^{n+1} in M_h so that the

following holds for all $q \in M_h$:

$$\int_{\Omega_{cf}} \nabla\psi^{n+1} \cdot \nabla q = \frac{3}{2\Delta t} \int_{\Omega_{cf}} \mathbf{u}^{n+1} \cdot \nabla q, \tag{6.12}$$

$$\int_{\Omega_{cf}} q\zeta^{n+1} = \int_{\Omega_{cf}} q\nabla\mathbf{u}^{n+1}. \tag{6.13}$$

The pressure is corrected by setting

$$p^{n+1} = p^n + \psi^{n+1} - \frac{1}{R_\mathrm{e}}\zeta^{n+1}. \tag{6.14}$$

6.2.3 Extension to Non-Axisymmetric Obstacles

As mentioned before, we have assumed so far that the conducting fluid domain Ω_{cf} is completely axisymmetric. To account for non-axisymmetric obstacles, such as curved blades, the pseudo-penalty method introduced by Pasquetti *et al.* [45] has been implemented in `SFEMaNS`. For details and validation of the code we refer to Cappenera [11, Chapter 2].

We now review the pseudo-penalty method. We first define Ω_{obs} as the domain that represents the obstacle inside the fluid. Such obstacle is allowed to be non-axisymmetric. Using the same notation as in (6.2.1), the pseudo-penalty method

consists in solving the following equations in the whole extended domain $\Omega_{cf} \cup \Omega_{\text{obs}}$:

$$\frac{\widetilde{\mathbf{u}}^{n+1} - \chi \mathbf{u}^n}{\Delta t} - \frac{1}{R_{\text{e}}} \Delta \widetilde{\mathbf{u}}^{n+1} + \nabla p^n = \chi \mathbf{f}^{n+1}, \tag{6.15}$$

$$\begin{cases} \frac{\mathbf{u}^{n+1} - \widetilde{\mathbf{u}}^{n+1}}{\Delta t} + \nabla \psi^{n+1} = 0, \\ \nabla \cdot \mathbf{u}^{n+1} = 0, \end{cases} \tag{6.16}$$

$$-\Delta \psi^{n+1} = \frac{1}{\Delta t} \nabla \cdot \widetilde{\mathbf{u}}^{n+1}, \tag{6.17}$$

$$\zeta^{n+1} = -\frac{1}{R_{\text{e}}} \nabla \cdot \widetilde{\mathbf{u}}^{n+1}, \tag{6.18}$$

$$p^{n+1} = p^n + \psi^{n+1} + \zeta^{n+1}, \tag{6.19}$$

where χ is called the penalty function defined as

$$\chi = \begin{cases} 1 \quad \text{in} \quad \Omega_{cf}, \\ 0 \quad \text{in} \quad \Omega_{\text{obs}}. \end{cases} \tag{6.20}$$

It can be proven, see [45, 11], that the predicted velocity $\widetilde{\mathbf{u}}$ computed using (6.15)-(6.19) is also a solution of the equation

$$\frac{\widetilde{\mathbf{u}}^{n+1} - \chi \widetilde{\mathbf{u}}^n}{\Delta t} - \frac{1}{R_{\text{e}}} \Delta \widetilde{\mathbf{u}}^{n+1} + \nabla p^n + \chi \nabla \psi^n = \chi \mathbf{f}^{n+1},$$

so the Navier-Stokes equations (6.1) are solved in Ω_{cf}, and a zero velocity is imposed in Ω_{obs}. Stability of scheme (6.15)-(6.19) has been proven in [11].

The code `SFEMaNS` implements a variant of scheme (6.15)-(6.19), and the case when we have a moving obstacle, i.e., $\chi^n = \chi(t_n)$. Denoting as $\mathbf{u}^n_{\text{obs}}$ the velocity of the obstacle, the scheme is as follows; we solve (6.12)-(6.14) for the pressure p^{n+1},

and for the velocity $\mathbf{u}^{n+1}$ we solve

$$\frac{3\mathbf{u}^{n+1}}{2\Delta t} - \frac{1}{R_{\mathrm{e}}}\Delta\mathbf{u}^{n+1} = -\nabla p^{n} + \chi^{n+1}\left(\frac{4\mathbf{u}^{n} - \mathbf{u}^{n-1}}{2\Delta t} - \nabla\left(\frac{4\psi^{n} - \psi^{n-1}}{3}\right)\right) \qquad (6.21)$$
$$\chi^{n+1}(-(\nabla\times\mathbf{u}^{*,n+1})\times\mathbf{u}^{*,n+1} + \mathbf{f}^{n+1}) + \frac{3\mathbf{u}^{n+1}_{\mathrm{obst}}}{2\Delta t}(1-\chi^{n+1}),$$

where $\mathbf{u}^{*} = 2\mathbf{u}^{n} - \mathbf{u}^{n-1}$. However, despite the fact that a second order extrapolation and BDF2 have been used to approximate $\mathbf{u}^{n+1}$ and the time derivative of $\mathbf{u}$, respectively; scheme (6.21) is just first order in time accurate at the obstacle boundary, see [11]. Peskin [46, 47] was the first to introduced penalty methods for immersed obstacles; other approaches are reported in Homann *et al.* [35] and Fadlun *et al.* [21].

6.3 The VKS Dynamo Experiment

From this subsection to the end of section we finally report the main objective of this thesis. That is, a full MHD numerical simulation of the VKS dynamo experiment. Using the methods described in section 5 and in the previous subsection, the code `SFEMaNS` has been extended to solve numerically the MHD equations (6.1)-(6.2) in the presence of non-axisymmetric conducting obstacles inside the domain Ω. Specifically, schemes (5.10), (6.12)-(6.14) and (6.21) are completely integrated in `SFEMaNS version 3.0`[1].

In this thesis we restrict to Direct Numerical Simulation (DNS) for moderated Reynolds numbers ($200 \leq R_{\mathrm{e}} \leq 2500$), and perform 20 turns for each hydrodynamic simulation. It is worth mentioning that in the work of Cappanera [11], `SFEMaNS v3.0` code is used as well to simulate a similar VKS set up, but with different type of blades; the author performs only an hydrodynamic study, but uses Large Eddy

[1]This code can be requested to `guermond@math.tamu.edu`

Simulation (LES) as well to get computations for $R_e \sim 5000$. His numerical results give a reasonable approximation to experimental data, validating then the Navier-Stokes and LES implementation code within `SFEMaNS v3.0`. We now begin our report for the VKS simulations describing next the experimental setting

6.3.1 Experimental Setup

We simulate the flow driven by TM73 impellers (for Turbine Métallique, meaning Metal Impeller in French) used in the 2006 experiment [42] (see figure 6.1b). The set-up uses two concentric cylindrical containers: one of radius $R_{\text{cyl}} = 206$mm (with a very small thickness) and another thick one of radius $R_{\text{in}} = 289$mm and $R_{\text{out}} = 330$mm made of copper. Both have a total height $H = 412$mm (we neglect the fluid behind the impellers). The impellers are composed of two disks each supporting 8 blades. The disks have a radius $R_b = 155$mm and thickness of 20mm. The blades have an angle of curvature equal to 24^o, a height of 41mm and a thickness of 5mm. Eventually the distance between the inner faces of the disks is set to 370mm such that the aspect ratio of the fluid is $370/206 = 1.8$ as in the TM28 that have been numerically studied in [36]. The fluid in the inner cylinder is pushed by the convex side of the blades (called the unscooping sense of rotation or (+) sense). In Cappanera [11] the TM87 impellers are used.

6.3.2 Numerical Model

The reference length L_{ref} is set to R_{cyl} so that the domain of computation for the hydrodynamic study is $\Omega_{cf} = \{(r, \theta, z) \in [0, 1] \times [0, 2\pi) \times [-1, 1]\}$ and the domain for the MHD study is a larger cylinder which can be decomposed in $\Omega_{cf} \cup \Omega_{\text{out}}$ with $\Omega_{\text{out}} = \{(r, \theta, z) \in [1, 1.6] \times [0, 2\pi) \times [-1, 1]\}$. Figure 6.1a shows Ω_{cf} and the impeller used inside as an obstacle. Denoting by σ_0 the electrical conductivity of the liquid sodium, ρ its density, μ_0 the magnetic permeability of vacuum, the

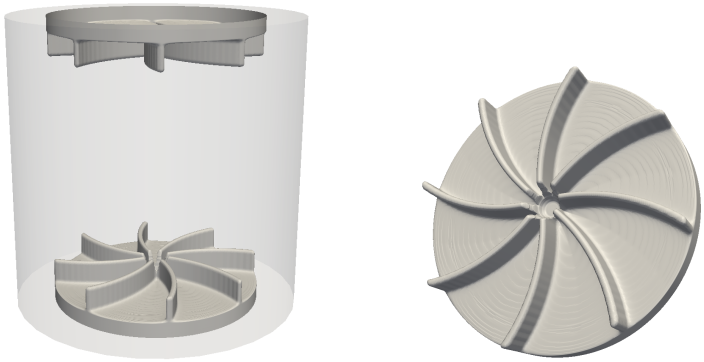

(a) Geometry. (b) TM73 Impeller.

Figure 6.1: VKS hydrodynamic experimental setting.

magnetic induction is made non-dimensional by using $B = U\sqrt{\rho\mu_0}$ (with B and $U = \omega R_{\text{cyl}}$ the reference magnetic induction and velocity respectively with ω the angular velocity of the impellers). Two governing parameters appear: $R_{\text{m}} = \mu_0\sigma_0 R_{\text{cyl}}^2\omega$ the magnetic Reynolds number and $R_{\text{e}} = R_{\text{cyl}}^2\omega/\nu$ the kinetic Reynolds number with ν the kinematic viscosity of the fluid.

The parameters σ, μ are not constant since the walls and the impellers may be composed of copper, steel or soft iron. Specifically, we take $\mathbf{u} = 0$ in Ω_{out}, $\sigma = 1, \mu = 1$ for $\{(r, \theta, z) \in [1, 1.4] \times [0, 2\pi) \times [-1, 1]\}$ (as for a stagnant lateral layer of liquid sodium) and $\sigma = 4.5, \mu = 1$ for $\{(r, \theta, z) \in [1.4, 1.6] \times [0, 2\pi) \times [-1, 1]\}$ (as for a lateral copper wall). We impose perfect ferromagnetic boundary conditions $\mathbf{B} \times \mathbf{n} = 0$ on the outer boundaries.

As mentioned before, we investigate the hydrodynamic and MHD regimes of the above experimental set-up, we use schemes (5.10), (6.12)-(6.14), and (6.21). All of them are now implemented in the code `SFEMaNS`. To define the penalty function χ in (6.20), the cylinder Ω_{cf} is split into a solid obstacle domain Ω_{obs} (composed of the rotating impellers) and a fluid domain Ω_{cf} that are both time dependent due to the

impellers rotation. Recall that we define μ similarly in (3.19) as

$$\mu = \begin{cases} \mu^c & \text{in} \quad \Omega_c \\ \\ 1 & \text{in} \quad \Omega_v \end{cases} . \tag{6.22}$$

where μ^c corresponds to the relative magnetic permeability of the blades with respect to the vacuum. However, in our simulations we make χ and μ to have a smooth profile. We also specify the velocity of the obstacle $\mathbf{u}^n_{\text{obs}}$ that appears in scheme (6.21) as

$$\mathbf{u}^n_{\text{obs}}(r,\theta,z) = \begin{cases} -r\mathbf{e}_\theta & \text{if } z > 0, \\ \\ r\mathbf{e}_\theta & \text{if } z \leq 0. \end{cases} \tag{6.23}$$

6.4 Hydrodynamic Study of the VKS

We first perform hydrodynamic computations integrating (6.1) in the range $R_{\text{e}} \in [200, 2500]$ setting the magnetic induction field $\mathbf{B}$ to zero. We have run a total of 20 turns for each hydrodynamic simulation. Table 6.1 shows the discretization parameters used for each run. All simulations were performed using the Brazos Cluster at Texas A&M.

We will characterize the structure of the flow by representations of the velocity field and by computing various time-averaged physical quantities. The time average $\overline{f}$ of a quantity f is defined as follows:

$$\overline{f} = \frac{1}{q} \sum_{1 \leq n \leq q} f^n. \tag{6.24}$$

Quantities of interest are the kinetic energy E and an indicator of the fluctuation

level δ defined by:

$$E(t) = \frac{1}{2}\|\mathbf{u}\|_{L^2(\Omega)} = \frac{1}{2}\int_\Omega |\mathbf{u}(\mathbf{r},t)|^2 d\mathbf{r}, \quad \delta(\mathbf{u}) = \frac{\|\mathbf{u}\|^2_{L^2(\Omega)}}{\|\overline{\mathbf{u}}\|^2_{L^2(\Omega)}}. \tag{6.25}$$

We also introduce the poloidal and toroidal components, respectively denoted by $P(\mathbf{u})$ and $T(\mathbf{u})$, of the velocity fields that we define as Ravelet in [49]:

$$P(\mathbf{u}) = \frac{1}{|\Omega|}\int_\Omega \sqrt{u_{r,0}^2 + u_{z,0}^2}\, d\Omega, \quad T(\mathbf{u}) = \frac{1}{|\Omega|}\int_\Omega |u_{\theta,0}| d\Omega \tag{6.26}$$

where $u_{r,0}$, $u_{\theta,0}$ and $u_{z,0}$ are the radial, azimuthal and vertical components associated to the Fourier mode $m = 0$ of the velocity $\mathbf{u}$. We also consider the ratio of the poloidal and toroidal components $\Gamma(\mathbf{u}) = P(\mathbf{u})/T(\mathbf{u})$ and two other quantities which are the root mean square velocity and the dimensionless torque K_p defined by:

$$U_{\mathrm{RMS}} = \overline{\sqrt{\frac{2E}{|\Omega|}}}, \quad K_p = \frac{1}{2\omega^2}\int_{\Omega_{\mathrm{solid}}} |(\mathbf{r}\times\mathbf{F})\cdot\mathbf{e}_z| d\Omega, \tag{6.27}$$

where $\mathbf{F}$ is the force that induces a rotating motion of the impellers and ω is the impeller angular velocity. Due to the non-dimensionalization of the problem we have $\omega = 1$. Using χ and $\mathbf{u}_{\mathrm{obs}}$ respectively defined in equations (6.20) and (6.23) K_p is given by:

$$K_p = \frac{1}{2}\int_\Omega r(1-\chi)\mathrm{sign}(z)\frac{3}{2}(\mathbf{u}-\mathbf{u}_{\mathrm{obs}})\cdot\mathbf{e}_\theta d\Omega \tag{6.28}$$

with $\mathrm{sign}(z)$ equal to 1 if $z > 0$ and -1 elsewhere.

Figure 6.2 shows the time evolution of the kinetic energy: at $R_\mathrm{e} = 200$ the flow is steady, at $R_\mathrm{e} = 500$ the flow is marginally unsteady, and increasing further R_e leads to a fluctuating regime. Figures 6.3-6.5 show the time averaged velocity components $\overline{\mathbf{u}}_x, \overline{\mathbf{u}}_y$, and $\overline{\mathbf{u}}_z$ respectively.

Figure 6.7 shows the time averaged azimuthal spectra of the kinetic energy: $\overline{E_m} = \overline{\int_{\Omega^{2D}_{\text{fluid}}} \pi |\hat{\mathbf{u}}(r,m,z,t)|^2 r \mathrm{d}r\mathrm{d}z}$ where $\hat{\mathbf{u}}(r,m,z,t)$ is the m-th Fourier component of the velocity field $\mathbf{u}(r,\theta,z,t)$. The maxima at $m=0$ and $m=8$ of the energy spectrum correspond respectively to the large scale forcing induced by the rotating disks and to the flow induced by the 8 rotating blades. As expected the steady flow at $R_\mathrm{e}=200$ is dominated by the $m=0$ and $m=8$ modes (and their harmonics). At $R_\mathrm{e}=500$ the flow is dominated by the $m=0$ and $m=2$ modes: the azimuthal shear layer near the equator acquires a wavy structure with two co-rotating radial vortices as seen in [50]. The spectrum in figure 6.7b shows that all even modes are populated by nonlinearity. At higher R_e numbers, the $m=1,2,3$ modes compete with a predominance of the $m=3$ mode (and still the $m=0$ and 8 modes). These modes populate all the modes and the spectra are more continuous (see figure 6.7d). Intense helical vortices are generated between the blades as seen in figure 6.10 and first numerically evidenced by [51, 36].

Figure 6.8 shows the instantaneous velocity component $\mathbf{u}_z$ on the plane cut at $z=0$. It is clearly seen the dominance of mode $m=2$ for $R_\mathrm{e}=500$ and the dominance of mode $m=3$ for $R_\mathrm{e}=1000$ in figures 6.8b and 6.8c, respectively. This strengthens the statements mentioned in the preceding paragraph. The dominance of mode $m=3$ is still noticed for $R_\mathrm{e}=1500$ and $R_\mathrm{e}=2500$ in figures 6.8d and 6.8e, respectively; however the fluid is more unstable. Figure 6.9 shows the instantaneous velocity component $\mathbf{u}_z$ on the plane cut at $z=-0.8$.

Table 6.2 shows that all quantities except $\overline{K_p}$ increase with R_e. It is known that the quantities $\overline{\delta(\mathbf{u})}$ (characterizing the turbulent fluctuations in inhomogeneous anisotropic flows [12]) and $\overline{K_p}$ (the dimensionless torque) should reach Reynolds independent values at large R_e numbers. Despite our limited R_e range the global trend followed by the global quantities compares well with the experimental results

of [50].

R_e	Δt	$\mathbb{P}_1$-npts	$\mathbb{P}_1$-nelems	$\mathbb{P}_2$-npts	nmodes	DoF	nprocs
200	0.01	7568	14758	29893	64	8621312	64
500	0.01	✓	✓	✓	✓	✓	✓
1000	0.0025	✓	✓	✓	✓	✓	✓
1500	0.00125	13319	26260	52897	✓	15246464	192
2500	0.00125	20780	41039	82598	✓	23804928	192

Table 6.1: Discretization parameters for each VKS hydrodynamic run, where $\mathbb{P}_k$-npts is the total number of points for the $\mathbb{P}_k$-mesh; similarly $\mathbb{P}_k$-nelems is the total number of elements, nmodes is the number of complex Fourier modes, DoF is the degrees of freedom, and nprocs is the number of CPU cores used. All computations were performed using the Brazos Cluster at Texas A&M.

R_e	$\overline{E}$	$\overline{\delta(\mathbf{u})}$	$\overline{P(\mathbf{u})}$	$\overline{T(\mathbf{u})}$	$\overline{\Gamma(\mathbf{u})}$	U_{RMS}	$\overline{K_p}$
200	0.2287	1.0122	0.07533	0.1936	0.3892	0.2698	0.063108
500	0.2983	1.0201	0.09327	0.2005	0.4653	0.3082	0.053126
1000	0.3893	1.1172	0.11446	0.2460	0.4651	0.3520	0.050474
1500	0.4078	1.2123	0.11569	0.2263	0.5113	0.3603	0.050783
2500	0.4427	1.3461	0.12437	0.2193	0.5671	0.3754	0.051977

Table 6.2: Hydrodynamic computations for the TM73 set-up.

6.5 MHD Results of the VKS

We now solve the full MHD system (6.1)-(6.2) using as initial velocity field the velocity computed during the Navier-Stokes runs at $R_e = 500$ or $R_e = 1500$ and a random initial seed for the magnetic field. Various MHD runs are performed for different values of the magnetic Reynolds number and relative magnetic permeability of the impellers summarized in tables 6.3 and 6.4. The onset of dynamo action

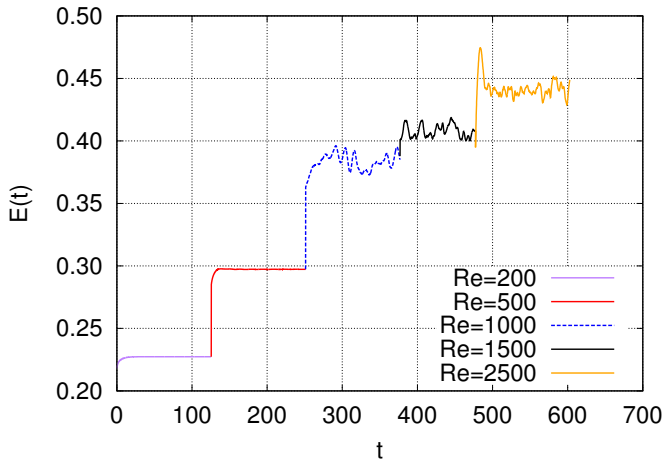

Figure 6.2: Time evolution of the total kinetic energy at different R_e.

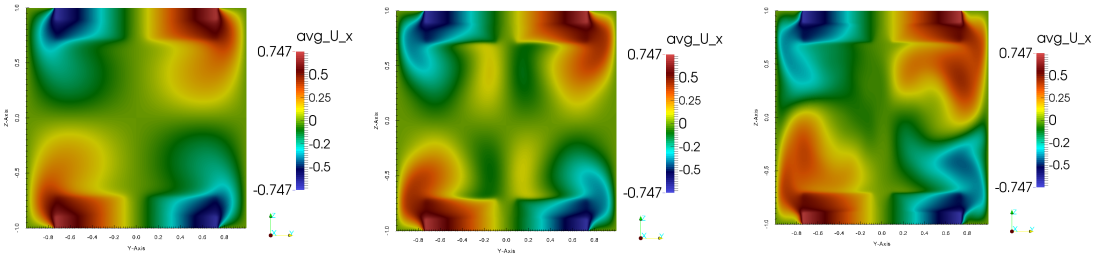

(a) $R_e = 200$. (b) $R_e = 500$. (c) $R_e = 1000$.

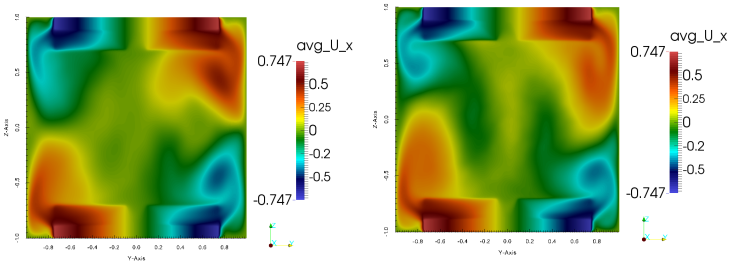

(d) $R_e = 1500$. (e) $R_e = 2500$.

Figure 6.3: Component $\overline{\mathbf{u}}_x$ of the mean velocity at final time at plane cut $x = 0$. This corresponds to the azimuthal component of $\overline{\mathbf{u}}$.

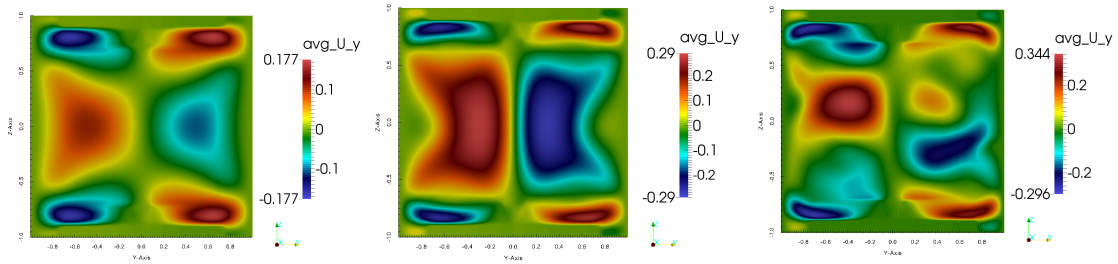

(a) $R_e = 200$. (b) $R_e = 500$. (c) $R_e = 1000$.

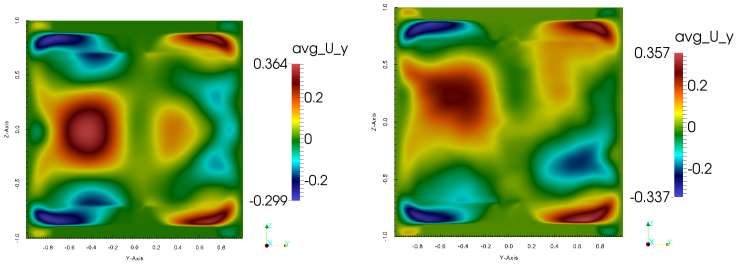

(d) $R_e = 1500$. (e) $R_e = 2500$.

Figure 6.4: Component $\overline{\mathbf{u}}_y$ of the mean velocity at final time at plane cut $x = 0$.

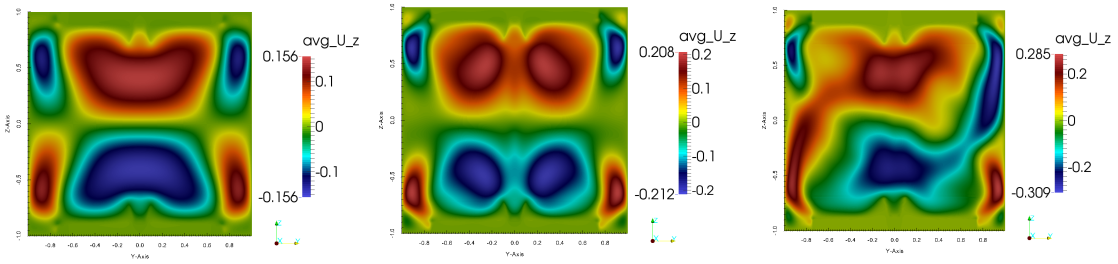

(a) $R_e = 200$. (b) $R_e = 500$. (c) $R_e = 1000$.

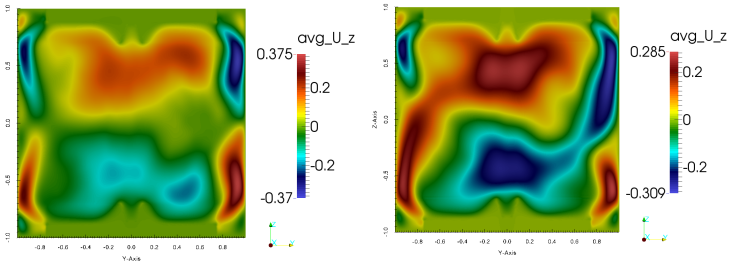

(d) $R_e = 1500$. (e) $R_e = 2500$.

Figure 6.5: Component $\overline{\mathbf{u}}_z$ of the mean velocity at final time at plane cut $x = 0$.

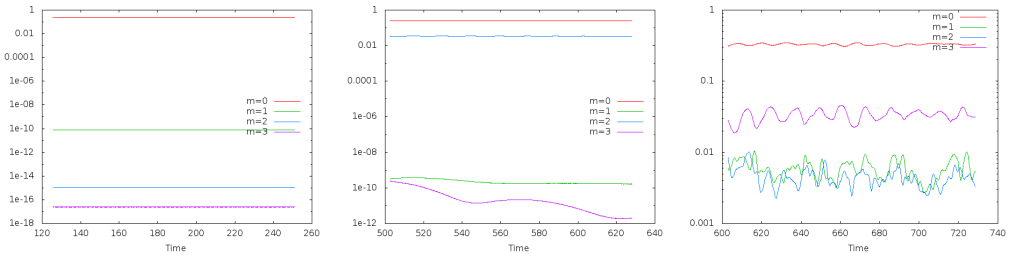

(a) $R_e = 200$. (b) $R_e = 500$. (c) $R_e = 1000$.

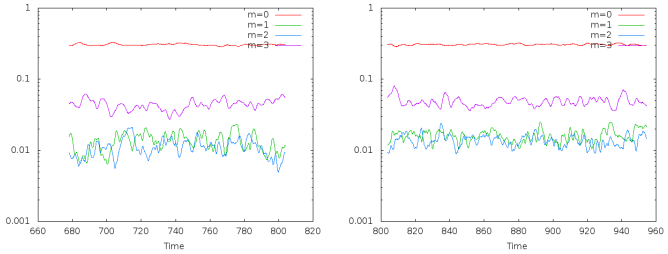

(d) $R_e = 1500$. (e) $R_e = 2500$.

Figure 6.6: Time evolution of the kinetic energy at different R_e for modes $m = 0, 1, 2$ and 3.

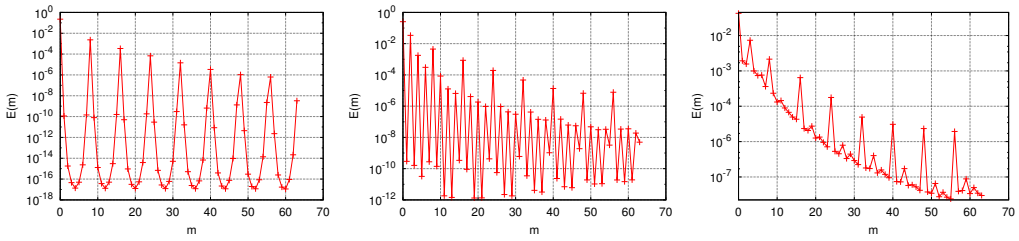

(a) $R_e = 200$ (b) $R_e = 500$ (c) $R_e = 1000$

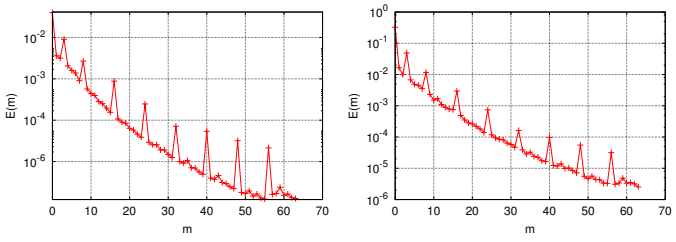

(d) $R_e = 1500$ (e) $R_e = 2500$

Figure 6.7: Time averaged spectra of the kinetic energy as a function of the azimuthal mode.

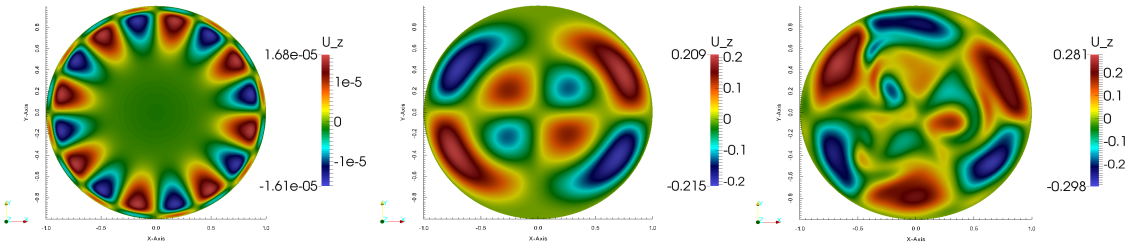

(a) $R_e = 200$. (b) $R_e = 500$. (c) $R_e = 1000$.

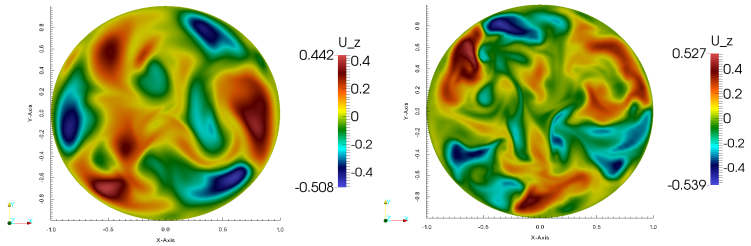

(d) $R_e = 1500$. (e) $R_e = 2500$.

Figure 6.8: Component $\mathbf{u}_z$ of the instantaneous velocity at plane cut $z = 0$ at final time.

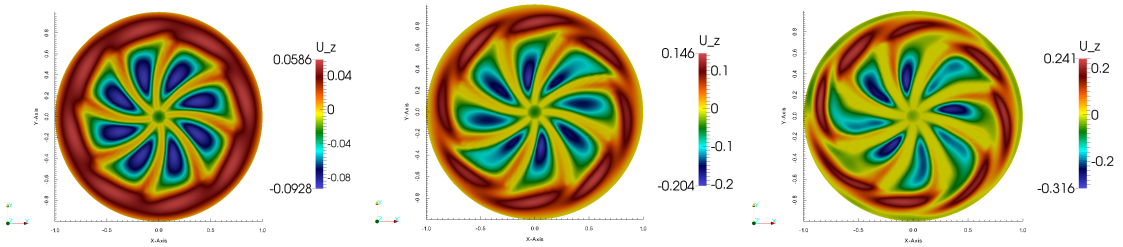

(a) $R_e = 200$. (b) $R_e = 500$. (c) $R_e = 1000$.

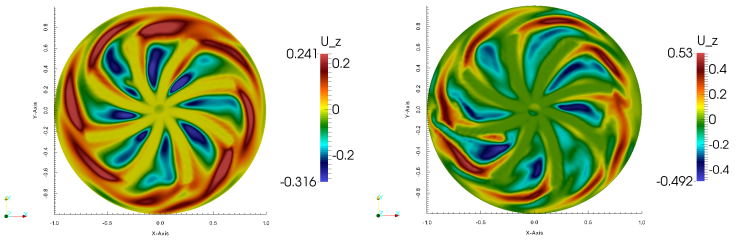

(d) $R_e = 1500$. (e) $R_e = 2500$.

Figure 6.9: Component $\mathbf{u}_z$ of the instantaneous velocity near the bottom blades at plane $z = -0.8$ at final time.

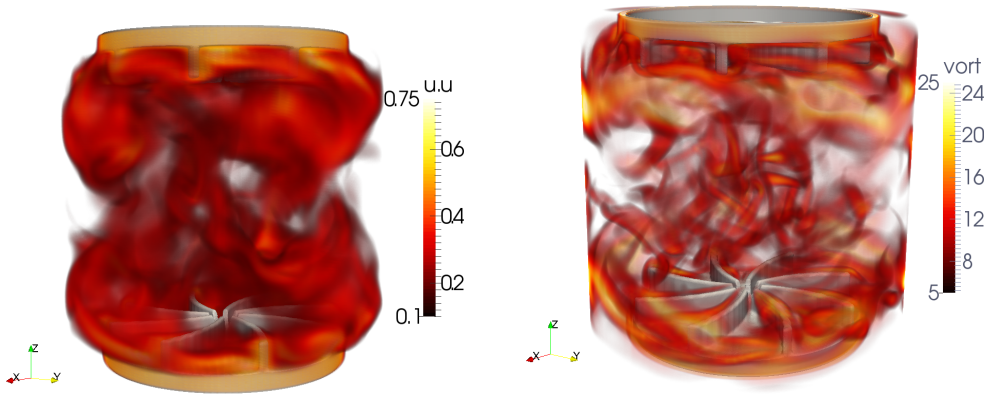

(a) Kinetic energy (b) Vorticity

Figure 6.10: Navier-Stokes simulations in the TM73 VKS configuration at $R_e = 2500$: (a) full scale for $\|\mathbf{u}\|_{L^2(\Omega)} = 2\,E(t)$, (b) partial scale for the vorticity field $\nabla\times\mathbf{u}$ (total scale is between 5 and 41).

is monitored by recording the time evolution of the magnetic energy in the conducting domain, $M(t) = \frac{1}{2}\int_{\Omega\cup\Omega_{\text{out}}} \mathbf{h}(\mathbf{r},t)\cdot\mathbf{b}(\mathbf{r},t)d\mathbf{r}$, as well as the modal energies $M_m(t) = \int_{\Omega^{2D}\cup\Omega^{2D}_{\text{out}}} \pi|\hat{\mathbf{h}}(r,m,z,t)|^2 r dr dz$. Linear dynamo action occurs when $M_m(t)$ is an increasing function of time and nonlinear dynamo action takes place when $M(t)$ saturates.

6.5.1 Two Distinct Families at $R_e = 500$

We have seen that the flow at $R_e = 500$ is characterized by the predominance of the even modes for the velocity field. Due to this azimuthal dependence, the eigenvalue problem associated with (6.1)-(6.2) has two disconnected families of magnetic eigenspaces generated by the even and odd Fourier modes. We henceforth refer to these vector spaces as the 0-family and the 1-family respectively. Given any initial data for (6.1)-(6.2) with nonzero projection on the two families, time integration of the equations gives a magnetic field which is a superposition of the leading eigenvectors in each family.

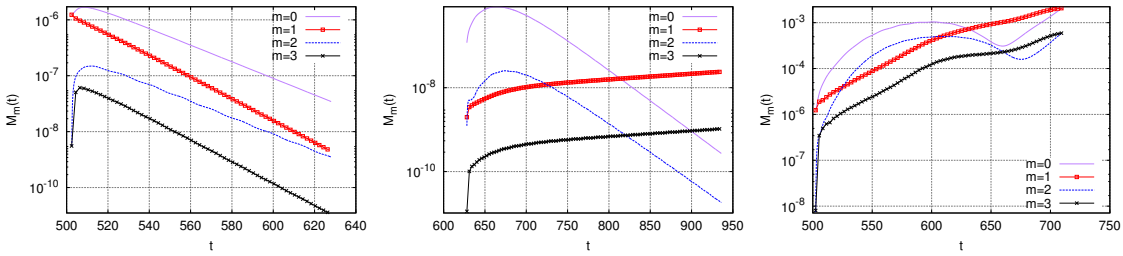

(a) $R_\mathrm{m} = 50$ (b) $R_\mathrm{m} = 150$ (c) $R_\mathrm{m} = 300$

Figure 6.11: Time evolution of the modal magnetic energies $M_m(t)$ for $m = 0, 1, 2, 3$ and for $R_\mathrm{m} \in [50, 300]$ at $R_\mathrm{e} = 500$ and $\mu = 5$.

A typical time evolution of the modal magnetic energy M_m for $m = 0$ to 3 and for $R_\mathrm{m} \in [50, 300]$ at $R_\mathrm{e} = 500$ and $\mu = 5$ is shown in figure 6.11. As expected the two families display two distinct growth-rates for each R_m. Note that the 1-family is supercritical before the 0-family at $R_\mathrm{m} = 150$. Linear interpolation of the growth-rates determines the critical magnetic Reynolds number R_mc when the growth-rate is zero, reported in table 6.3. Figure 6.13a shows the magnetic field at the end of the integration of figure 6.11b. Note the parallel and anti-parallel vectors near the vertical axis. We observe the expected $m = 1$ eigenmode evidenced in kinematic dynamo computations in figure 6.12; compare with [25] (see figure 2d therein). This mode is characterized by an equatorial dipole with two opposite axial structures mainly localized in the bulk of the fluid.

An estimate of the effective magnetic permeability of the soft iron TM73 used in [42] is $\mu \approx 65$ [66]. Therefore we vary the relative permeability of the impellers. Increasing μ enhances the 0-family growth-rates (see figure 6.14) and switches the ordering of the thresholds. Note that the 1-family thresholds barely change with μ because the corresponding eigenmode is localized mainly in the bulk while the 0-family thresholds vary dramatically because the corresponding eigenmode is characterized

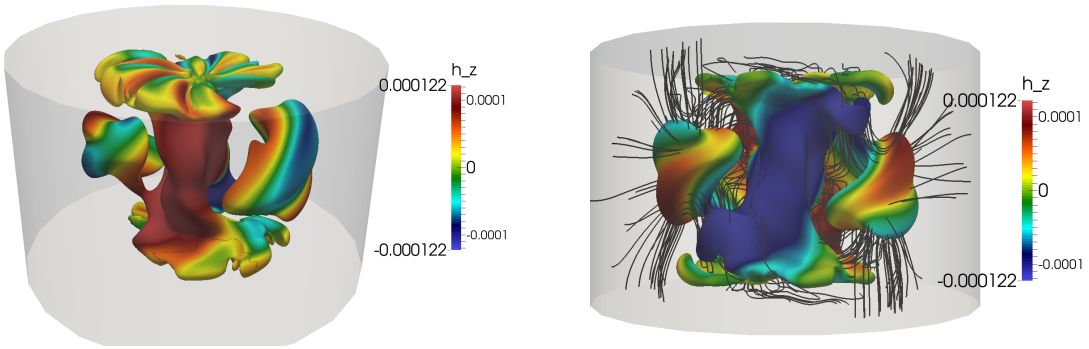

(a) Isosurface (b) Isosurface with streamlines

Figure 6.12: MHD simulations in the TM73 VKS configuration at $R_e = 500, R_m = 150$, with $\mu_b = \mu_d = 5$ represented by isosurface $\|\mathbf{H}\|^2$ (12% of maximum value) colored by the vertical component.

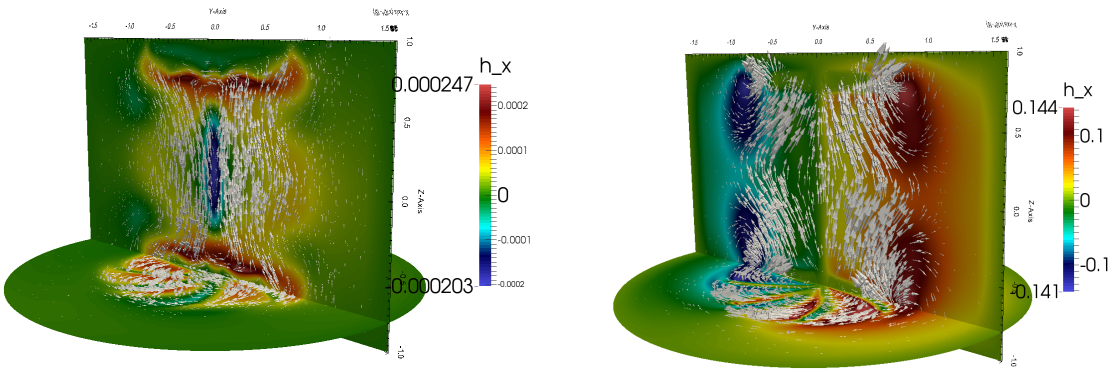

(a) $\mu = 5$ (b) $\mu = 100$

Figure 6.13: MHD simulations in the TM73 VKS configuration at $R_e = 500$, $R_m = 150$ and (a) $\mu = 5$ (1-family), (b) $\mu = 100$ (0-family). Arrows represent in-plane $\{h_y, h_z\}$ vectors or $\{h_x, h_y\}$ vectors and color represents the out-of-plane component h_x wrt the meridian plane Oyz.

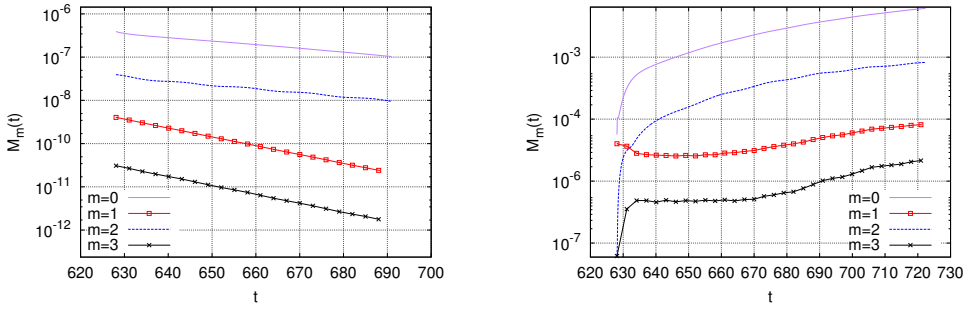

(a) $R_\mathrm{m} = 50$ (b) $R_\mathrm{m} = 150$

Figure 6.14: Time evolution of the modal magnetic energies $M_m(t)$ for $m = 0, 1, 2, 3$ and for $R_\mathrm{m} \in \{50, 150\}$ at $R_\mathrm{e} = 500$ and $\mu = 100$.

by an axial dipole in the bulk and an azimuthal magnetic component concentrated in the impellers (see figure 6.13b).

μ	R_mc(0-family)	R_mc(1-family)
5	240 ±5	147 ±1
50	130 ±2	138 ±2
100	82 ±2	144 ±2

Table 6.3: Magnetic thresholds for $R_\mathrm{e} = 500$.

6.5.2 No Distinct Magnetic Family at $R_e = 1500$

At $R_\mathrm{e} = 1500$ the flow is more fluctuating and all the velocity modes are coupled with a predominance of the $m = 0$ and $m = 3$ modes. Therefore there is no distinct magnetic family and the eigenmode is mainly axisymmetric. Computations need more spatial resolution and CPU time. We have tested two relative permeabilities $\mu \in \{5, 50\}$ and reported the thresholds in table 6.4. The modal magnetic energies for the $m \in [0, 4]$ modes show that the $m = 0$ and $m = 3$ magnetic modes are coupled

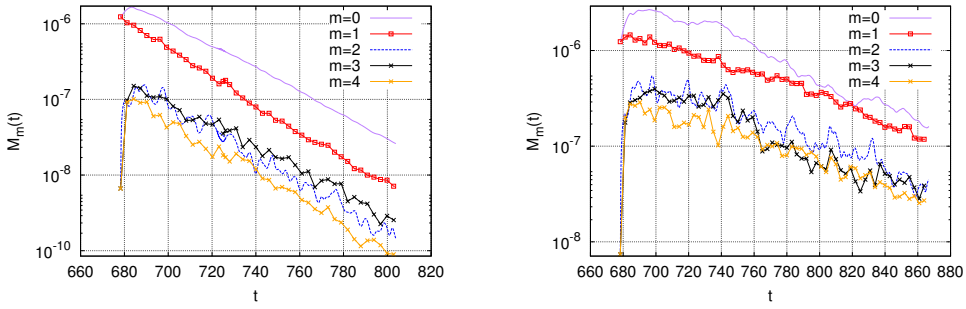

(a) $R_\mathrm{m} = 50$ (b) $R_\mathrm{m} = 100$

Figure 6.15: Time evolution of the modal magnetic energies $M_m(t)$ for $m \in [0, 4]$ and for $R_\mathrm{m} \in \{50, 100\}$ at $R_\mathrm{e} = 1500$ and $\mu = 5$.

as well as $m = 1$ and $m = 4$ magnetic modes because of the predominance of the $m = 3$ mode in the velocity field (see figures 6.15 and 6.16).

An illustrative view of the generated magnetic field is displayed on figure 6.17. The radial component is odd with respect to z whereas the azimuthal and vertical components are even and of opposite sign. These features are compatible with the magnetic field measured at saturation in the experimental dynamo regime obtained with soft iron impellers (see figure 6b in [7]). Using a ferromagnetic material decreases the dynamo threshold and enhances the predominantly axisymmetric magnetic field.

μ	R_mc
5	130 $\pm$5
50	90 $\pm$5

Table 6.4: Magnetic thresholds for $R_\mathrm{e} = 1500$.

Finally, table 6.5 shows the discretization parameters used for all MHD runs for $R_\mathrm{e} = 500$ and $R_\mathrm{e} = 1500$. All simulations were performed using the Brazos Cluster

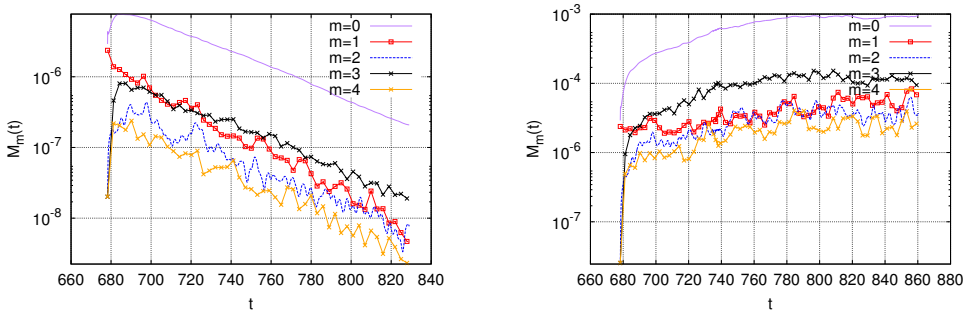

(a) $R_\mathrm{m} = 50$ (b) $R_\mathrm{m} = 100$

Figure 6.16: Time evolution of the modal magnetic energies $M_m(t)$ for $m \in [0, 4]$ and for $R_\mathrm{m} \in \{50, 100\}$ at $R_\mathrm{e} = 1500$ and $\mu = 50$.

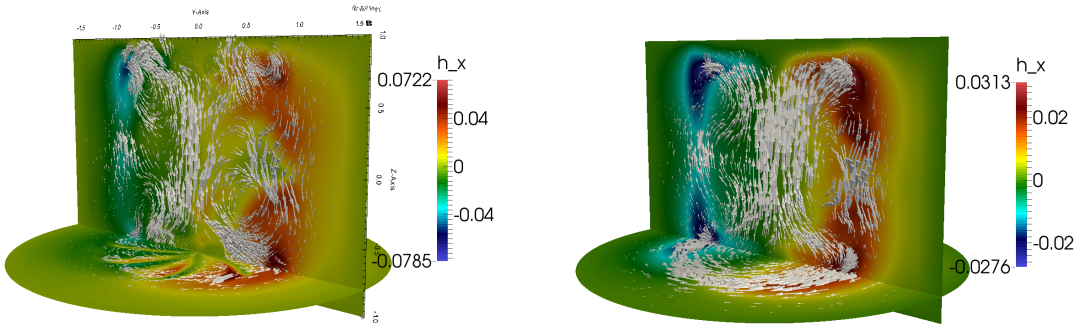

(a) Instantaneous magnetic field (b) Time averaged magnetic field

Figure 6.17: MHD simulations in the TM73 VKS configuration at $R_\mathrm{e} = 1500$, $R_\mathrm{m} = 150$ and $\mu = 50$. Arrows represent in-plane $\{h_y, h_z\}$ vectors or $\{h_x, h_y\}$ vectors and color represents the out-of-plane component h_x wrt the meridian plane Oyz.

at Texas A&M.

$\mathbf{R}_{\mathrm{e}}$	**500**	**1500**
$\mathbb{P}_1$-npts for Ω_{cf}	7568	13319
$\mathbb{P}_1$-nelems for Ω_{cf}	14758	26260
$\mathbb{P}_2$-npts for Ω_{cf}	29893	52897
$\mathbb{P}_1$-npts for Ω	9092	14843
$\mathbb{P}_1$-nelems for Ω	17818	29320
$\mathbb{P}_2$-npts for Ω	36202	59206
nmodes	64	64
DoF	19052800	32303104
nprocs	64	192

Table 6.5: Discretization parameters used for all MHD-VKS runs for $R_{\mathrm{e}} = 500$, and $R_{\mathrm{e}} = 1500$, where $\mathbb{P}_k$-npts is the total number of points for the $\mathbb{P}_k$-mesh to discretize Ω_{cf} or $\Omega = \Omega_{cf} \cup \Omega_{\mathrm{out}}$; similarly $\mathbb{P}_k$-nelems is the total number of elements, nmodes is the number of complex Fourier modes, DoF is the degrees of freedom, and nprocs is the number of CPU cores used. We have used $\mathbb{P}_2$ for each component of $\mathbf{B}^c$, and $\mathbb{P}_1$ for p^c. All computations were performed using the Brazos Cluster at Texas A&M.

6.5.3 Conclusion

Our results show for the first time that the ferromagnetic impellers are crucial to obtain the predominantly axisymmetric dynamo mode in a VKS configuration in a full-MHD model at moderate kinetic Reynolds numbers. Increasing R_{e} from 500 to 1500 decreases the dynamo threshold and a numerical challenge would be to extend the range of R_{e} in numerical simulations.

7. CONCLUSION

All the studies led in this PhD time frame have been motivated by upgrading of the `SFEMaNS` code in order to simulate numerically the VKS experiment. This project comes after the previous PhD thesis of R. Laguerre [37], A. Ribeiro [53], and F. Luddens [39] that allowed the beginning of `SFEMaNS`, and its development into a massive parallel code that can approximate MHD problems involving discontinuous magnetic permeability in the radial and vertical directions.

In this period we first studied a simpler model that mimics the induction equation of the Maxwell equations in the low frequency regime. We proposed two time stepping schemes that avoid implicit convolutions when Fourier-finite element methods are used for spacial discretization. Stability of both schemes was proved. We then extended these ideas for general scalar parabolic PDEs with variable coefficients in time and space. A second order accurate in time scheme was proposed, which avoids implicit convolutions using time independent matrices. Its stability was also proved.

Taking inspiration from our studies of the simpler model, a new formulation of the MHD equations using $\mathbf{B}$, and a novel time stepping method were proposed to handle non-axisymmetric magnetic permeability. The method was implemented in `SFEMaNS`, and comparisons against the 3D code `DOLMEN` [67] were done for the kinematic dynamo problem to validate our new method and its implementation.

Then in collaboration with L. Cappanera [11], `SFEMaNS` was extended to simulate the Navier-Stokes equations when non-axisymmetric moving obstacles are present. Numerical studies with the VKS set up and using `SFEMaNS` were performed, then giving acceptable results against experimental data [50].

Finally, full VKS-MHD computations were performed using `SFEMaNS` code. Our

results show for the first time that the ferromagnetic impellers are crucial to obtain the predominantly axisymmetric dynamo mode in a VKS configuration in a full-MHD model at moderate kinetic Reynolds numbers ($500 \leq R_e \leq 1500$).

7.1 Future Studies

The main goal is to study the turbulence effects to generate the fluid dynamo as in the real VKS experiment. This implies the objective of overcoming the numerical challenge of extending the range of R_e in numerical simulations. As of now, a Large Eddy Simulation (LES) model is being implemented in `SFEMaNS` by L. Cappanera. To handle $R_e \geq 10^3$, our current algorithm for the Maxwell equations may need stabilization for high-magnitude velocities.

REFERENCES

[1] A. Alonso. A mathematical justification of the low-frequency heterogeneous time-harmonic Maxwell equations. *Math. Models Methods Appl. Sci.*, 9(3):475–489, 1999.

[2] D.N. Arnold. An interior penalty finite element method with discontinuous elements. *SIAM J. Numer. Anal.*, 19:742–760, 1982.

[3] S. Badia and R. Codina. Nodal-based finite element approximation of the Maxwell problem suitable for singular solutions. *Siam J. Numer. Anal.*, 50(2):398–417, 2012.

[4] G.A. Baker. Finite element methods for elliptic equations using nonconforming elements. *Math. Comp.*, 31(137):45–59, 1977.

[5] J. Becker. A second order backward difference method with variable steps for a parabolic problem. *BIT*, 34(4):644–662, 1998.

[6] C. Bernardi, M. Dauge, M. Yvon, and M. Azaiez. *Spectral Methods for Axisymmetric Domains*. Gauthier-Villars, Paris, 1999.

[7] J. Boisson, S. Aumaitre, N. Bonnefoy, M. Bourgoin, F. Daviaud, B. Dubrulle, Ph. Odier, J.-F. Pinton, N. Plihon, and G. Verhille. Symmetry and couplings in stationary von Kármán sodium dynamos. *New J. Phys.*, 14(1):013044, 2012.

[8] A. Bonito and J.-L. Guermond. Approximation of the eigenvalue problem for the time harmonic Maxwell system by continuous Lagrange finite elements. *Math. Comp.*, 2011. DOI: 10.1090/S0025-5718-2011-02464-6.

[9] A. Bonito, J.-L. Guermond, and F. Luddens. An interior penalty method with C^0 finite elements for the approximation of the Maxwell equations in heteroge-

neous media: Convergence analysis with minimal regularity. *Math. Modelling and Numer. Anal. (M2AN)*, 2016. http://dx.doi.org/10.1051/m2an/2015086.

[10] J.H. Bramble and J.E. Pasciak. A new approximation technique for div-curl systems. *Math. Comp.*, 73:1729–1762, 2004.

[11] L. Cappanera. *Nonlinear stabilization of magnetohydrodynamics equations and application to multiphase flow.* PhD thesis, 2015. PhD dissertation in Fluid mechanics, advisor: Nore, C. , Paris Saclay 2015.

[12] P.-P. Cortet, P. Diribarne, R. Monchaux, A. Chiffaudel, F. Daviaud, and B. Dubrulle. Normalized kinetic energy as a hydrodynamical global quantity for inhomogeneous anisotropic turbulence. *Phys. Fluids*, 21(2), 2009.

[13] M. Costabel. A coercive bilinear form for Maxwell's equations. *J. Math. Anal. Appl.*, 157(2):527–541, 1991.

[14] M. Costabel and M. Dauge. Weighted regularization of Maxwell equations in polyhedral domains. A rehabilitation of nodal finite elements. *Numer. Math.*, 93(2):239–277, 2002.

[15] P. A. Davidson. *An Introduction to Magnetohydrodynamics.* Cambridge Texts in Applied Mathematics (No. 25), 2001.

[16] S. Dong and J. Shen. A time-stepping scheme involving constant coefficient matrices for phase-field simulations of two-phase incompressible flows with large density ratios. *J. Comput. Phys*, 23(17):5788–5804, 2012.

[17] E. Dormy and A. M. Soward. *Mathematical Aspects of Natural Dynamos (The Fluid Mechanics of Astrophysics and Geophysics).* Chapman and Hall/CRC, 2007.

[18] E. Emmrich. Stability and error of the variable two–step BDF for semilinear parabolic problems. *J. Appl. Math & Computing*, 19(1):33–55, 2005.

[19] A. Ern and J.-L. Guermond. *Theory and Practice of Finite Elements*, volume 159 of *Applied Mathematical Sciences*. Springer-Verlag, New York, 2004.

[20] L.C. Evans. *Partial Differential Equations*. American Mathematical Society, New York, 2nd edition, 2010.

[21] E.A. Fadlun, R. Verzicco, P. Orlandi, and J. Mohd-Yusof. Combined immersed-boundary finite-difference methods for three-dimensional complex flow simulations. *J. Comput. Phys.*, 2000. DOI: 10.1006/jcph.2000.6484.

[22] A. Gailitis, O. Lielausis, S. Dement'ev, E. Platacis, and A. Cifersons. Detection of a flow induced magnetic field eigenmode in the Riga dynamo facility. *Phys. Rev. Lett.*, 84:4365, 2000.

[23] A. Gailitis, O. Lielausis, G. Platacis, Gerbeth, and F. Stefani. Detection of a flow induced magnetic field eigenmode in the Riga dynamo facility. *Phys. Fluids*, 11:2838–2843, 2004.

[24] J.F Gerbeau, L. B. Claude, and Leliévre T. *Mathematical Methods for the Magnetohydrodynamics of Liquid Metals*. Oxford University Press, 2006.

[25] A. Giesecke, C. Nore, F. Stefani, G. Gerbeth, J. Léorat, W. Herreman, F. Luddens, and J.-L. Guermond. Influence of high-permeability discs in an axisymmetric model of the Cadarache dynamo experiment. *New J. Phys.*, 14(5):1367–2630, 2012.

[26] A. Giesecke, C. Nore, F. Stefani, G. Gerbeth, J. Léorat, F. Luddens, and J.-L. Guermond. Electromagnetic induction in non-uniform domains. *Geophys. Astrophys. Fluid Dyn.*, 104(5-6):505–529, 2010.

[27] A. Giesecke, F. Stefani, and G. Gerbeth. Role of soft-iron impellers on the mode selection in the von Kármán-sodium dynamo experiment. *Phys. Rev. Lett.*, 104:044503, 2010.

[28] V. Girault and P.A. Raviart. *Finite Element Methods for Navier-Stokes Equations: Theory and Algorithms*. Springer Series in Computational Mathematics, 1986.

[29] J.-L. Guermond, R. Laguerre, J. Léorat, and C. Nore. An interior penalty Galerkin method for the MHD equations in heterogeneous domains. *J. Comput. Phys.*, 221(1):349–369, 2007.

[30] J.-L. Guermond, R. Laguerre, J. Léorat, and C. Nore. Nonlinear magnetohydrodynamics in axisymmetric heterogeneous domains using a Fourier/finite element technique and an interior penalty method. *J. Comput. Phys.*, 228(8):2739–2757, 2009.

[31] J.-L. Guermond, J. Léorat, F Luddens, C. Nore, and Ribeiro A. Effects of discontinuous magnetic permeability on magnetohynamic problems. *J. Comput. Phys.*, 230(16):6299–6319, 2011.

[32] J.-L. Guermond and J. Shen. On the error estimates for the rotational pressurecorrection projection methods. *Math. Comp.*, 73(248):1719–1737, 2004.

[33] B. Heinrich and B. Weber. Fourier–finite–element approximation of elliptic interface problems in axisymmetric domains. *Math. Meth. Appl. Sci*, 19:909–931, 1996.

[34] J. S. Hesthaven, S. Gottlieb, and D. Gottlieb. *Spectral Methods for Time-Dependent Problems*. Cambridge Monographs on Applied and Computational Mathematics (No. 21), 2007.

[35] H. Homann, J. Bec, and R. Grauer. Effect of turbulent fluctuations on the drag and lift forces on a towed sphere and its boundary layer. *J. Fluid Mech.*, 721:155–179, 4 2013.

[36] S. Kreuzahler, D. Schulz, H. Homann, Y. Ponty, and R. Grauer. Numerical study of impeller-driven von Kármán flows via a volume penalization method. *New J. Phys.*, 16(10):103001, 2014.

[37] R. Laguerre. *Approximation des équations de la MHD par une méthode hybride spectrale-éléments finis nodaux: application á léffet dynamo*. PhD thesis, Paris 7, 2006.

[38] R. Laguerre, C. Nore, A. Ribeiro, J. Léorat, J.-L. Guermond, and F. Plunian. Impact of impellers on the axisymmetric magnetic mode in the VKS2 dynamo experiment. *Phys. Rev. Lett.*, 101(10):104501, 2008.

[39] F. Luddens. *Theoretical and numerical analysis of the magnetohydrodynamics equations: application to dynamo action*. PhD thesis, Université Paris Sud-Paris XI, 2012.

[40] L. Marié, J. Burguete, F. Daviaud, and J. Léorat. Numerical study of homogeneous dynamo based on experimental von Kármán type flows. *EPJ B*, 33(4):469–485, 2003.

[41] H.K. Moffatt. *Magnetic Field Generation in Electrically Conducting Fluids*. Cambridge Monographs on Mechanics and Applied Mathematics. Cambridge University Press, Cambridge, UK, 1978.

[42] R. Monchaux, M. Berhanu, M. Bourgoin, Ph. Odier, M. Moulin, J.-F. Pinton, R. Volk, S. Fauve, N. Mordant, F. Pétrélis, A. Chiffaudel, F. Daviaud,

B. Dubrulle, C. Gasquet, L. Marié, and F. Ravelet. Generation of magnetic field by a turbulent flow of liquid sodium. *Phys. Rev. Lett.*, 98:044502, 2007.

[43] P. Monk. *Finite Element Methods for Maxwell's Equations*. Clarendon Press, Oxford, 2003.

[44] C. Nore, D. Castanon-Quiroz, J.-L. Guermond, J. Leorat, and F. Luddens. Numerical dynamo action in cylindrical containers. *EPJ AP*, 70:31101, 2015.

[45] R. Pasquetti, R. Bwemba, and L. Cousin. A pseudo-penalization method for high Reynolds unsteady flows. *App. Num. Math.*, 58(7):946–954, 2008.

[46] C. Peskin. Flow patterns around heart valves: a numerical method. *J. Comput. Phys.*, 10(2):252–271, 1972.

[47] C. Peskin. Numerical analysis of blood flow in the heart. *J. Comput. Phys.*, 25(3):220–252, 1977.

[48] Yu. B. Ponomarenko. Theory of the hydrodynamic generator. *J. Appl. Mech. Tech.*, 14:775–778, 1973.

[49] F. Ravelet. *Bifurcations globales hydrodynamiques et magnétohydrodynamiques dans un écoulement de von Kármán turbulent*. PhD thesis, Ecole Polytechnique X, 2005.

[50] F. Ravelet, A. Chiffaudel, and F. Daviaud. Supercritical transition to turbulence in an inertially driven von Kármán closed flow. *J. Fluid Mech.*, 601:339–364, 2008.

[51] F. Ravelet, B. Dubrulle, F. Daviaud, and P.-A. Ratié. Kinematic alpha tensors and dynamo mechanisms in a von Kármán swirling flow. *Phys. Rev. Lett.*, 109:024503, Jul 2012.

[52] M. Renardy and R.C. Rogers. *An Introduction to Partial Differential Equations*. Springer-Verlag, 1992.

[53] A. Ribeiro. *Approche spectralléléments finis pour des problèmes de magnétohydrodynamique non–linéaires*. PhD thesis, Université Paris Sud-Paris XI, 2010.

[54] G.O. Roberts. Spatially periodic dynamos. *Philos. Trans. R. Soc. London. Series A*, 266:535–558, 1970.

[55] G.O. Roberts. Dynamo action of fuid motions with two-dimensional periodicity. *Philos. Trans. R. Soc. London. Series A*, 271:411–454, 1972.

[56] Agarwal R.P. *Difference Equations and Inequalities: Theory, Methods, and Applications*. Chapman & Hall–CRC Pure and Applied Mathematics 228. CRC Press, 2nd edition, 2000.

[57] G. Rüdiger and R. Hollerbach. *The Magnetic Universe: Geophysical and Astrophysical Dynamo Theory*. Wiley-VCH, 2004.

[58] A.A. Samarskii. *The Theory of Difference Schemes*. CRC Press, 2001.

[59] D. D. Schnack, I. Lottati, Z. Mikić, and P. Satyanarayana. A finite-volume algorithm for three-dimensional magnetohydrodynamics on an unstructured, adaptive grid in axially symmetric geometry. *J. Comput. Phys.*, 140(1):71–121, 1998.

[60] J. Shen and X. Yang. Numerical approximations of Allen–Cahn and Cahn–Hilliard equations. *DCDS*, Series A(28):1669–1691, 2010.

[61] C.R. Sovinec, A.H. Glasser, T.A. Gianakon, D.C. Barnes, R.A. Nebel, S.E. Kruger, S.J. Plimpton, A. Tarditi, M.S. Chu, and the NIMROD Team. Nonlinear magnetohydrodynamics with high-order finite elements. *J. Comp. Phys.*, 195:355, 2004.

[62] R. Stieglitz and U. Müller. Experimental demonstration of a homogeneous two-scale dynamo. *Phys. Fluids*, 13:561–564, 2001.

[63] R. Temam. *Navier-Stokes Equations: Theory and Numerical Analysis*. North-Holland, Amsterdam, 1984.

[64] V. Thomée. *Galerkin Finite Element Methods for Parabolic Problems*. Springer Series in Computational Mathematics 25. Springer-Verlag, 2nd edition, 2006.

[65] A. Tilgner. Kinematic dynamos with precession driven flow in a sphere. *Geophys. Astrophys. Fluid Dyn.*, 101(1):1–9, 2007.

[66] G. Verhille, N. Plihon, M. Bourgoin, Ph. Odier, and J.-F. Pinton. Induction in a von Kármán flow driven by ferromagnetic impellers. *New J. Phys.*, 12(3):033006, 2010.

[67] H. Zaidi, F. Bouillault, C. Nore, A. Bossavit., and J.-L. Guermond. Approximation of the time-dependent induction equation with advection using Whitney elements: application to dynamo action. *COMPEL*, 35(1):326–339, 2016.